Institute of Physics, Polish Academy of Sciences
Division of Physics and Technology of Wide Band Gap Semiconductor Nanostructures

Unveiling the mechanical stimuli by mechanoluminescence: From experimental setup design to material analysis

Syed Shabhi Haider
A thesis presented for the degree of
Doctor of Philosophy

Principal supervisor:
Prof. Dr Hab. Andrzej Suchocki

Auxiliary supervisor:
Dr. Justyna Barzowska

2025, Warsaw, Poland

Table of Contents

Abstract 5

Abstrakt (in Polish) 7

Acknowledgements 9

List of publications and participation in conferences 10

List of symbols acronyms 13

Chapter 1 Background and Scope of the Thesis 14

1.1. Introduction and aim of the thesis 14

1.2. Outline of the thesis 16

Chapter 2 Mechanoluminescence 17

2.1. Brief historical background 17

2.2. Classification 18

2.3. ML materials and their applications 19

2.4. Experimental Setups and Techniques 21

2.4.1. Impact-induced ML 21

2.4.2. Stress-induced ML 25

2.4.3. Friction-induced ML 25

2.4.4. Ultrasound-induced Luminescence 27

2.4.5. Atomic Force Microscopy based 28

2.4.6. Diamond Anvil Cell based 29

Chapter 3 Self-Designed Experimental Techniques and Setups 32

3.1. Impact-induced ML technique 34

3.1.1. Measurements of ML with non-ML material composites 38

3.1.2. I-ML reproducibility testing 39

3.1.3. I-ML signal by tuning incident angle 40

3.1.4. I-ML measurements for multiple shots....42
3.2. Stress-induced ML technique 43
3.3. Ultrasound-induced Luminescence technique 46
3.3.1. Us-L Measurements at different Us pulse's duration 48
3.3.2. Us amplitude dependent Us-L Measurements 49
3.3.3. Temperature dependent Us-L Measurements 49
Chapter 4 Mechanoluminescence Properties of $LiTaO_3$:Pr 51
4.1. Synthesis process....51
4.2. Characterization techniques....52
4.3. Results and discussion....52
4.3.1. XRD and XPS analysis....52
4.3.2. Absorption and photoluminescence....55
4.3.3. Mechanoluminescence properties....56
4.3.4. Persistent luminescence and Thermoluminescence 62
Chapter 5 Ultrasound induced Luminescence of $LiTaO_3$:Pr 65
5.1. Experimental....65
5.1.1. Preparation of $LiTaO_3$:Pr embedded PDMS films 65
5.1.2. Measuring techniques 66
5.2. Results and discussion....67
5.2.1. Us-L properties at 20 kHz frequency....67
5.2.1.1. Vibrational amplitude-dependent Us-L 68
5.2.1.2. Temperature-dependent Us-L 70
5.2.2. Us-L at 3.3 MHz frequency....73
5.2.3. Thermoluminescence and trap analysis 74
Chapter 6 Thermal Anti-Quenching Properties of $LiTaO_3$:Pr....79

6.1. Intensity Ratio for Luminescence Thermometry 80
6.2. Thermal Anti-Quenching analysis of $LiTaO_3$:Pr 82
6.3. $LiTaO_3$:Pr based Luminescence Thermometry 84
Chapter 7 Mechanoluminescence Properties of Other Materials 90
7.1. Experimental 90
7.1.1. Sample preparation and applied measuring techniques 90
7.2. Results and discussion 91
7.2.1. Mechanoluminescence analysis 91
7.2.2. Ultrasound-induced Luminescence analysis 94
Chapter 8 Conclusion & Future Outlooks 102
8.1. Conclusion 102
8.2. Future outlook 103
References 105

ABSTRACT

Research results reported in this Ph.D. dissertation provide a comprehensive analysis of mechanoluminescence (ML) and the associated phenomenon of ultrasound-induced luminescence (Us-L). The initial part of this study focuses on the development of experimental techniques and setups to investigate ML under various mechanical stimuli and Us-L generated at different ultrasound frequencies. The first two setups directly relate to ML analysis, namely impact-induced ML and stress-induced ML setups. In the impact-induced ML setup, a spherical projectile is fired at the sample to measure ML during the collision. The correlation between incident kinetic energy and ML is thoroughly investigated by varying the incident angle of the projectile up to 40°. The setup is also useful for measuring the ML reproducibility of the material by multiple shootings. In the case of stress-induced ML setup, mechanical force is applied to deform the sample pellets at a specific rate, allowing the study of the correlation between applied force and ML. Additionally, the visualization of stress distribution within the specimen can be achieved by capturing the ML with a digital camera. The third setup focuses on the study of Us-L at 20 kHz frequency, utilizing an ultrasound transducer and a photomultiplier to capture Us-L. This setup is capable of measuring the Us-L at variable pulse durations, vibrational amplitudes and ultrasound powers. The results obtained from multiple measurements of well-known phosphor materials, including $Sr_{0.95}Ca_{0.05}(SO_4)$:Mn, $CaAl_2O_4$:Eu,Dy,La and $SrAl_2O_4$:Eu,Dy validate the excellent performance of these setups in various categories of ML studies.

In the second part of the study, the ML, Us-L, and luminescence thermometric properties of $LiTaO_3$:Pr are comprehensively investigated. Upon excitation at 270 nm, $LiTaO_3$:Pr exhibits photoluminescence with three prominent emission peaks at 511 nm, 616 nm, and 890 nm. Additionally, charge carrier trapping occurs in $LiTaO_3$:Pr, leading to persistent luminescence, thermoluminescence and mechanoluminescence. These trapped charge carriers can also be released when exposed to ultrasound waves. By varying the concentration of praseodymium (1% for sample S1, 3% for sample S2, and 5% for sample S3), the activation energy of the traps (i.e., the trap depth) is modulated. For sample S1, the energy difference between the deep and shallow traps is approximately 0.1 eV, whereas for samples S2 and S3, this difference increases to about 0.45 eV. Moreover, S1 has a relatively higher concentration of shallow traps than S2 and S3. The variation in trap properties in each sample is also responsible for the distinct behavior under mechanical stimuli and ultrasound exposure at different experimental conditions. Impact-induced Mechanoluminescence measurements demonstrate fast mechanical impact detection capabilities of the $LiTaO_3$:Pr samples with excellent ML retention and at various impact kinetic energies. Stress-induced Mechanoluminescence measurements reveal a remarkable superposition of emitted ML intensity curves with time-dependent applied force. Additionally, light emission from $LiTaO_3$:Pr under exposure to low (20 kHz) and high (3.3 MHz) frequency ultrasound waves is also studied. S1 shows high-intensity Us-L and long-distance ultrasound detection. Meanwhile, S2 demonstrates better retention among them, and all of them exhibit good response to ultrasound. The distinct acoustic phenomena observed at low (acoustic cavitation) and high (acoustic streaming) frequencies may lead to different prominent mechanisms of light

emission: ML-driven at 20 kHz and TL-driven at 3.3 MHz. Furthermore, the $LiTaO_3$:Pr sample exhibits thermal anti-quenching, advantageous for luminescence thermometry. The S1 sample demonstrates good performance with a wide temperature range (173–693 K) and high relative sensitivity (11 $\%K^{-1}$), surpassing several previously studied materials. The findings validate $LiTaO_3$:Pr as a promising candidate for fast, sensitive, and remote detection of various mechanical stimuli, ultrasound waves and temperature in industrial and biological applications.

The ML and Us-L properties of additional materials, including $SrSi_2O_2N_2$:Eu, $SrSi_2O_2N_2$:Eu,Mn, AlN:Mn and ZnS:Mn have also been studied. The findings confirm that these materials possess the ability to detect both stress and ultrasound, converting them into visible light signals. This makes them promising candidates for future use in a wide range of mechano-optic sensing applications. Optimized composites could be developed for the remote estimation of the magnitude or region of real-time stress by simply observing color changes (instead of intensity) in the materials with the naked eye or an optical camera. This idea offers another visual and intuitive method for detecting and monitoring mechanical stress, opening up new possibilities for applications.

ABSTRAKT (in Polish)

Badania opisane w niniejszej rozprawie doktorskiej dotyczą kompleksowej analizy mechanoluminescencji (ML) i związanego z nią zjawiska luminescencji indukowanej ultradźwiękami (Us-L). Wstępna część tych badań dotyczy opracowania technik eksperymentalnych do badania ML wywoływanej różnymi bodźcami mechanicznymi i Us-L generowanej przy różnych częstotliwościach ultradźwięków. Pierwsze dwa zestawy pomiarowe umożliwiają bezpośredni pomiar zjawiska ML, a mianowicie układ do pomiaru ML indukowanej uderzeniem i układ do pomiaru ML indukowanej naprężeniem (ściskaniem). W układzie do ML indukowanej uderzeniem, kulisty pocisk jest wystrzeliwany w próbkę, aby uzyskać ML podczas zderzenia. Korelacja między siłą uderzenia pocisku a natężeniem ML może być dokładnie badana poprzez zmianę kąta padania pocisku do 40°. Układ ten umożliwia również badanie powtarzalności ML dla danego materiału poprzez pomiary ML wywołanej wielokrotnymi uderzeniami przez serię pocisków wystrzeliwanych z zadana częstotliwością. W przypadku zestawu pomiarowego do badania ML indukowanej naprężeniem (ściskaniem), wykorzystano uniwersalną maszynę wytrzymałościową. Próbka w postaci krążka jest odkształcana (ściskana) z określoną szybkością, co umożliwia badanie korelacji między przyłożoną siłą a natężeniem ML. Ponadto rozkład naprężeń w próbce uzyskuje się poprzez rejestrację ML za pomocą aparatu cyfrowego. Trzeci ze zbudowanych układów pomiarowych do służy do badania Us-L generowanej ultradźwiękami o częstotliwości 20 kHz. W układzie tym zastosowano przetwornik ultradźwiękowy i fotopowielacz do rejestracji Us-L w konfiguracji pozwalającej mierzyć Us-L przy zmiennych czasach trwania impulsów, amplitudach drgań i mocach ultradźwięków.

Wszystkie trzy zbudowane zestawy pomiarowe zostały najpierw starannie przetestowane z wykorzystaniem dobrze znanych materiałów luminescencyjnych $Sr_{0,95}Ca_{0,05}(SO_4)$:Mn, $CaAl_2O_4$:Eu,Dy,La i $SrAl_2O_4$:Eu,Dy. Wyniki uzyskane z wielokrotnych pomiarów potwierdziły doskonałą przydatność tych układów pomiarowych do badania w różnych rodzajów ML.

W drugiej części badań kompleksowo zbadano ML, Us-L, luminescencję, i właściwości termometryczne $LiTaO_3$:Pr. Po wzbudzeniu światłem o długości fali 270 nm $LiTaO_3$:Pr wykazuje fotoluminescencję z trzema widocznymi pikami emisji przy 511 nm, 616 nm i 890 nm. Ponadto w $LiTaO_3$:Pr występuje pułapkowanie nośników ładunku, co prowadzi do przedłużonej luminescencji, termoluminescencji i mechanoluminescencji. Spułapkowane nośniki ładunku mogą być również uwalniane pod wpływem ultradźwięków. Zmieniając stężenie prazeodymu (1% dla próbki S1, 3% dla próbki S2 i 5% dla próbki S3), moduluje się energię aktywacji pułapek (tj. ich głębokość). W przypadku próbki S1 różnica energii między głębokimi i płytkimi pułapkami wynosi około 0,1 eV, podczas gdy w przypadku próbek S2 i S3 różnica ta wzrasta do około 0,45 eV. Ponadto, próbka S1 ma stosunkowo wyższe stężenie płytkich pułapek w porównaniu do S2 i S3. Zmienność właściwości pułapek w każdej próbce jest również odpowiedzialna za różne zachowanie pod wpływem bodźców mechanicznych i ekspozycji na ultradźwięki w różnych warunkach eksperymentalnych. Pomiary mechanoluminescencji zderzeniowej (I-ML) wykazują możliwości wykrywania zderzeń

mechanicznych próbek $LiTaO_3$:Pr z doskonałą retencją ML i przy różnych energiach kinetycznych uderzenia. Badania mechanoluminescencji indukowanej ściskaniem (S-ML)pokazują superpozycję emitowanych krzywych intensywności ML z zależną od czasu przyłożoną siłą. Ponadto badano również emisję światła z $LiTaO_3$:Pr pod wpływem fal ultradźwiękowych o niskiej (20 kHz) i wysokiej (3,3 MHz) częstotliwości. Próbka S1 wykazuje wysoką intensywność Us-L i detekcję ultradźwięków na stosunkowo duże odległości. Tymczasem próbka S2 wykazuje lepszą retencję wśród nich, a wszystkie z nich wykazują dobrą reakcję na ultradźwięki. Wyraźne zjawiska akustyczne obserwowane przy niskich (kawitacja akustyczna) i wysokich częstotliwościach (strumieniowanie akustyczne) mogą prowadzić do różnych mechanizmów emisji światła: indukowanych poprzez ML przy 20 kHz i poprzez TL przy 3,3 MHz. Ponadto próbka $LiTaO_3$:Pr wykazuje termiczne antywygaszanie, interesujące dla termometrii luminescencyjnej. Próbka S1 wykazuje dobrą wydajność przy szerokim zakresie temperatur (173–693 K) i wysokiej względnej czułości (11 $\%K^{-1}$), przewyższając szereg poprzednio badanych materiałów. Wyniki potwierdzają, że $LiTaO_3$:Pr jest obiecującym kandydatem do szybkiego, czułego i zdalnego wykrywania różnych bodźców mechanicznych, fal ultradźwiękowych i mierzenia temperatury w potencjalnych zastosowaniach przemysłowych i biologicznych.

Przebadano również właściwości ML i Us-L dodatkowych materiałów, w tym $SrSi_2O_2N_2$:Eu, $SrSi_2O_2N_2$:Eu,Mn, AlN:Mn i ZnS:Mn. Wyniki potwierdzają, że materiały te posiadają zdolność wykrywania zarówno naprężeń, jak i ultradźwięków, przekształcając je w światło widzialne. Dzięki temu są obiecującymi kandydatami do przyszłego wykorzystania w szerokim zakresie zastosowań ML. Istnieje możliwość opracowania i zoptymalizowania odpowiednich kompozytów w celu zdalnego oszacowania wielkości lub obszaru naprężenia w czasie rzeczywistym, poprzez obserwację zmiany koloru emisji (zamiast intensywności) w materiałach zarówno gołym okiem lub kamerą optyczną. Ten pomysł oferuje kolejną wizualną i intuicyjną metodę wykrywania i monitorowania naprężeń mechanicznych, otwierając nowe możliwości zastosowań praktycznych.

Acknowledgments

My deepest appreciation goes to the Almighty Allah, the most Beneficial and the most Merciful, for granting me His blessings and strengthening me in my difficult time. I offer my gratefulness to our Prophet Muhammad (S.A.W.W) and his Family (A.S), who have given us the practical lesson of love, humanity, peace and justice. The saying of the Prophet Muhammad (S.A.W.W) "Acquire Knowledge and impart it to the people" tells the importance of knowledge and its spreading.

I would like to express my special thanks and gratitude to my principal supervisor: Prof. Dr Hab. Andrzej Suchocki and auxiliary supervisor: Dr. Justyna Barzowska for their supervision and encouragement throughout my research work. The door to Andrzej Suchocki's office was always open whenever I got into trouble or had a question regarding my research project. It was a great honor for me to work under their supervision.

I am cordially grateful to all my research collaborators (Dr. Ryszard Diduszko, Katarzyna Pojnar, Dr. Anna Wolska, Prof. Marcin T Klepka, Prof. Ludwika Lipinska, Dr. Dawid Jankowski) from other labs for their collaboration. I am also highly thankful to Magdalena Baran for the synthesis of the $LiTaO_3$:Pr samples useful for this study. Moreover, I am grateful to Prof. Philippe Smet for inviting me multiple times for research visits to their LUMILAB, Belgium and to Dr. David Van der Heggen for the assistance in LUMILAB. I also appreciate Dr. Aleksejs Zol and Ernests Einbergs for welcoming me to training visits at the Optical Materials Lab, University of Latvia.

I cordially appreciate the efforts of all ON4.1 Group of High-Pressure Spectroscopy Labs members (Prof. Dr. Yaroslav Zhydachevskyy, Dr. Paweł Ciepielewski, Dr. Volodymyr Tsiumra, Dr. Lev-Ivan Bulyk, Dr. Damian Włodarczyk, Saranya Narayanan, Ajeesh Kumar Somakumar, Vasyl Stasiv, Dr. Piotr Dróżdż, Prof. Agata Kamińska, Prof. Dr. Hanka Przybylińska, Prof. Dr. Alexander Wittlin, Kamil Koronski and Piotr Sybilski) for cooperation and support during my experiments and providing enjoyable moments.

Separate thanks to the free version of ChatGPT was used to correct and revise the English language of this work.

I acknowledge the financial support of the Polish National Science Center OPUS grant No: 2019/33/B/ST8/02142. Moreover, I also acknowledge to STER programme by the Polish National Agency for Academic Exchange and Erasmus+ mobility program to fund my multiple research visits during PhD studies.

For this achievement, I would like to pay my heartiest thanks to the most precious and divine relations of life, my beloved parents, my wife and my siblings for their emotional support.

Regards:
Syed Shabhi Haider

List of publications and participation in conferences

Publications part of the PhD Thesis:

- **S. S. Haider**, J. Barzowska, A, Suchocki. Book chapter; Mechanoluminescence: Unveiling the Mechanical Stress, Specialist Periodical Reports-*Nanoscience: Volume 10*, 2024.
- **S. S. Haider**, M. Baran, R. Diduszko, et.al. Visible to Near-Infrared Mechanoluminescence from Pr-doped $LiTaO_3$ for Stress Sensing Applications, ACS, *The Journal of Physical Chemistry C*, 489-498,128 (1), 2023.
- **S. S. Haider**, J. Barzowska, P. Sybilski, A, Suchocki. Designing of experimental setup for impact induced mechanoluminescence measurements, *Measurement*, 112012, 203, 2022.
- A. K. Somakumar, Y. Zhydachevskyy, D. Wlodarczyk, **S. S. Haider**, J. Barzowska,... & A. Suchocki. Temperature and pressure dependent luminescence mechanism of a zinc blende structured ZnS: Mn nanophosphor under UV excitation, *Journal of Materials Chemistry C*, 7041-7052, 12 (19), 2024.

Other Publications:

- **S. S. Haider**, S. Dad, S. Zakar, M. Z. Iqbal, Mechanistic scrutinizing the charge storage phenomena of battery-grade Mn-Co-S electrodes, Materials Research Bulletin, 111953, 156, 2022.
- S. Zakar, M. Z. Iqbal, **S. S. Haider**, Binder-free ternary transition metal sulfides for energy storage applications, International Journal of Energy Research, 15696-15708, 46, 2022.
- **S. S. Haider**, M. Z. Iqbal, S. Zakar, et.al. Superior performance of electrodeposited CoMnS as novel electrode material for supercapattery devices, Journal of Energy Storage, 102608, 39, 2021.
- **S. S. Haider**, S. Zakar, M. Z. Iqbal, S. Dad, Battery- type electrodeposited ternary metal sulfides electrodes for advanced hybrid energy storage devices, Journal of Electroanalytical Chemistry, 115881, 904, 2022.
- M. Z. Iqbal, **S. S. Haider**, S. Zakar, et.al. Cobalt-oxide/carbon composites for asymmetric solid-state supercapacitors, Materials Research Bulletin, 110974, 131, 2020.
- M. Z. Iqbal, **S. S. Haider**, S. Siddique, M.R.A.Karim, S. Zakar, et.al. Capacitive and diffusion-controlled mechanism of strontium oxide based symmetric and asymmetric device, Journal of Energy Storage, 101056, 27, 2020.
- M. Z. Iqbal, **S. S. Haider**, S. Zakar, et.al. Superior performance of cobalt oxide/carbon composite for solid-state supercapattery devices, Physica B: Physics of Condensed Matter, 412561, 603, 2021.
- M. Z. Iqbal, S. Zakar, **S. S. Haider**, et.al. Electrodeposited CuMnS and CoMnS electrodes for high performance asymmetric supercapacitor devices, Ceramics International, 21343, 46, 2020.

- M. Z. Iqbal, S. Zakar, **S. S. Haider**, et.al. Scrutinizing the charge storage mechanism in SrO based composites for asymmetric supercapacitors by diffusion-controlled process, Applied Nanoscience, 3999, 10, 2020.
- M. Z. Iqbal, A. Khan, A. Numan, **S. S. Haider**, J. Iqbal. Ultrasonication-assisted synthesis of novel strontium based mixed phase structures for supercapattery devices, Ultrasonics Sonochemistry, 104730, 59, 2019.
- M. Z. Iqbal, S. Khan, A. Rehman, **S. S. Haider**, M. A. Kamran, et.al. Enhancement in the mobility of solution processable polymer-based FET by incorporating graphene interlayer, Superlattices and Microstructures, 106331, 137, 2019.
- M. Z. Iqbal, M. Faisal, S. R. Ali, **S. S. Haider**, et.al. Ultraviolet-light-driven current modulation of Au/WS2/Gr Schottky barrier, Physica E: Low-dimensional Systems and Nanostructures, 133837, 117, 2019.
- M.Z. Iqbal, A Khan, **S. S. Haider**, M. W. Iqbal, et.al. Magnetic field driven mobility tweaking in graphene, Journal of Nanoelectronics & Optoelectronics, 1427, 14, 2019.
- M.Z. Iqbal, A Khan, S. Khan, N. Anwar, **S. S. Haider**, et.al. Formation of pn-junction with chemical modification of graphene-hexagonal boron nitride heterostructure, Journal of Nanoelectronics & Optoelectronics, 1420, 14, 2019. (I F: 0.961)
- M. Alzaid, M. Z. Iqbal, **S. S. Haider**, S. Zakar, et. al. Charge carrier modulation in dual-gated graphene field effect transistor using honey as polar organic gate dielectric, Applied physics A, 438, 127, 2021.
- .M. Z. Iqbal, S. Zakar, **S. S. Haider**. Role of aqueous electrolytes on the performance of electrochemical energy storage device, Journal of Electroanalytical Chemistry, 113793, 858, 2020.
- M. Z. Iqbal, S.Siddique, A. Khan, **S. S. Haider**, et.al. Recent developments in graphene based novel structures for efficient and durable fuel cells, Materials Research Bulletin, 110674, 121, 2019.
- S.G. Nedilko, V. Chornii, A. Kuryliuk, M. Lazarenko, V. Scherbatskyi, V. Barbash, O. Yashchenko, **S. S. Haider**, A. Suchocki. Fabrication, Mechanical, Optical, and Dielectrical Properties of Paper Filled with SrAl 2 O 4: Eu, Dy Oxide and Carbon Nanotubes. **IEEE 14th International Conference Nanomaterials: Applications & Properties (NAP)** (pp. 1-4). IEEE, 2024.
- M. Z. Iqbal, J. Nabi, S. Siddique, H. T. A. Awan, **S. S. Haider**, et.al. Role of graphene and transition metal dichalcogenides as hole transport layer and counter electrode in solar cells, International Journal of Energy Research, 1464, 44, 2019.
- A. Aslam, A. Razzaq, S. Naz, N. Amin, M. I. Arshad, M. A. Nabi, A. Nawaz, K. Mahmood, A. Bibi, F. Iqbal, M. Shakil, Z. Farooq, M. Z. Iqbal, S. S. Haider, A. Rehman. Impact of lanthanum-doping on the physical and electrical properties of cobalt ferrites, **Journal of Superconductivity and Novel Magnetism**, 1855-1864, 34, 2021.

Conference presentations, workshops and research visits during PhD studies:

- Research visit to LumiLab, Department of Solid State Sciences, Ghent University, Ghent, Belgium for work on the ultrasound-induced luminescence measurement of

$SrSi_2N_2O_2$:Eu,Mn, and AlN:Mn materials samples, May 03 - June 01, 2024. (NAWA funding)

- One-week training visit at Optical Materials Lab, Institute of Solid Stated Physics, Riga, Latvia on theoretical modelling using COMSOL Multiphysics software, Feb 25 - March 03, 2024. (Erasmus+)
- Research visit to LumiLab, Department of Solid State Sciences, Ghent University, Ghent, Belgium for work on the ultrasound-induced luminescence measurement of $LiTaO_3$:Pr samples, Aug 02-31, 2023. (NAWA funding)
- One-week training visit at Optical Materials Lab, Institute of Solid Stated Physics, Riga, Latvia on ML measurement technique, Sept 10-16, 2023. (Erasmus+)
- Oral Presentation titled "Unveils the mechanical stimuli by mechanoluminescence: From designing of experimental setups to material analysis." at Condensed Matter Physics Seminar, Institute of Physics, Polish Academy of Sciences in Warsaw, Poland, Dec. 10, 2024.
- Oral Presentation titled "Temperature-dependent ultrasonic-induced luminescence properties of $LiTaO_3$:Pr at kHz and MHz range" at E-MRS 2024 FALL MEETING & EXHIBIT, University of Technology in Warsaw, Poland, Sept. 16-19, 2024.
- Poster presentation at IFPAN reporting session for results from 2022, Institute of Physics, PAS, Warsaw, Poland, 9th February 2023.
- Poster presentation titled "Designing of Experimental Setup for Impact Induced Mechanoluminescence Measurements" in the joint conference of FM&NT - NIBS 2022, Riga, Latvia, July 3^{rd}-6^{th}, 2022.
- Oral presentation in 1st International Conference on Applied Physics and Engineering, Department of Physics, NED University, Pakistan, 2021.

Conference presentations, workshops and research visits before PhD studies:

- Participated in the International Workshop on "2D materials & Quantum Effect Devices", at Pakistan Institute of Engineering & Technology, November 12th-14th, 2018.
- Participated in the International Workshop on "International Photonics symposium'18" at GIK Institute of Engineering Sciences & Technology, Pakistan, in collaboration with SPIE-OSA, 2018.
- Participated in the Workshop on "Data Science & Machine Learning" at Habib University, Pakistan, July 10th-14th, 2017.
- Practical course on "Mechatronics: Sense and Move Things with Arduino" in collaboration with ORIC at NED University of Engineering & Technology, Pakistan, Feb 6th- March 6th, 2016.

List of symbols

a	—	Edge length of crystallographic unit cell along x-axis
α	—	Angle between lattice constant, a, and c
c	—	Edge length of crystallographic unit cell along z-axis
E_g	—	Bandgap energy
E_F	—	Fermi energy level
E_a/k_B	—	Potential barrier between two easy magnetic orientations
k_B	—	Boltzmann constant

List of acronyms

ML	—	Mechanoluminescence
PL	—	Photoluminescence
TL	—	Thermoluminescence
I-ML	—	Impact-induced Mechanoluminescence
S-ML	—	Stress-induced Mechanoluminescence
U-ML	—	Ultrasound-induced Mechanoluminescence
Us-L	—	Ultrasound-induced Luminescence
PersL	—	Persistent Luminescence
Us	—	Ultrasound
UV	—	Ultraviolet
PD	—	Photodiode
PDT	—	Photodiode tube
dDAC	—	dynamic Diamond Anvil Cell
AFM	—	Atomic Force Microscope

CHAPTER 1. Background and Scope of the Thesis

1.1. Introduction and aim of the thesis

Light has a major involvement in the development of our civilization, it is the key source of energy and transfer of information. There are numerous mechanisms like photoluminescence, thermoluminescence, chemiluminescence, mechanoluminescence, bioluminescence, electroluminescence, etc., are utilized by the scientist for the exploration of their diverse application in industrial and medical domains [1-7]. This thesis aims to investigate mechanoluminescence and its associated phenomena like ultrasound-induced luminescence, ranging from the development of innovative experimental techniques to the analysis of mechanoluminescent materials. In general words, Mechanoluminescence is defined as the emission of light by a material during the application of mechanical stimuli upon it [8, 9]. A variety of mechanical stimuli are used to produce ML and study its behavior under applied mechanical action [10, 11]. Chapter 2 provides detailed information on ML and the experimental setups designed in the past for ML studies. In the late 20^{th} century, Chao Nan Xu et al. reported two ML materials, ZnS:Mn and $SrAl_2O_4$,Eu for applications in stress sensing for artificial skin and visualizing stress distribution in test specimens [12, 13]. These studies marked a significant milestone in discovering novel and reproducible ML materials for stress-sensing and visualization. Recently, researchers have explored a variety of ML materials such as $ZnS:Mn^{2+}$ (yellow 585 nm) [12, 14], $SrCaMgSi_2O_7:Eu^{2+}$ (bluish-green 499 nm) [15, 16], $Ca_2MgSi_2O_7:Eu^{2+}$ (green 530 nm) [17, 18], $Sr_2MgSi_2O_7:Eu^{2+}$ (blue 464 nm) [19, 20], $Ca_2Al_2SiO_7:Ce^{3+}$ (blue 402 nm) [21, 22], $BaZnOS:Mn^{2+}$ (orange 584 nm) [23], etc. with different color emission and investigate their application in several fields of stress sensing applications like impact sensors [24], stress sensor [13, 25], monitoring of active cracks [26], stress detection in bones [27] stress distribution in metal structure [25], etc.

Similarly, another unique type of light emission related to ML is also observed and named ultrasound-induced ML, produced by transition metal or rare earth doped piezoelectric, or luminescence materials during the exposure of ultrasound waves [28-30]. However, the mechanism of ultrasound-induced light emission is quite diverse. A general perception is ML produced by the stress-induced piezoelectric field that removes the charge carriers from various energy traps, recombined at luminescence centers, causing the emission of specific wavelengths of ML light [3, 10, 31]. However, in the case of ultrasound-induced luminescence, in addition to ML (induced by mechanical interaction with pressure transmitting medium), thermoluminescence may also occur. It is well-established that exposure to ultrasound waves induces a pressure field, leading to the generation of thermal energy [32]. So, because of this hypothesis, it is difficult to resolve that Us-L entirely belongs to ML or TL effects. Furthermore, the diverse applications of Us, spanning from clinical diagnostics to underwater exploration and communication, enhance the significance of Us-L for ultrasonic sensors and imaging technology beneficial for detecting and visualizing Us waves. In general, materials that have single or multiple energy traps can produce TL or ML. Consequently, many studies validate that the same materials also exhibit Us-L properties essential for Us applications. Examples of Us-L exhibiting materials include ZnS:Mn, ZnS:Cu, $CaZnOS:Nd^{3+}$, $SrAl_2O_4$:Eu, $BaSi_2O_2N_2:Eu^{2+}$, CaZnOS:Eu, etc [29, 33-38].

This thesis is based on the experimental investigation of ML phenomena under different mechanical stimulations and the analysis of Us-L associated with ML, TL, or both. Due to the variety of mechanical stimuli used for ML generation and its study, there are no standardized and commercially designed setups available on the market. Therefore, the first portion of this study is based on the designing of multiple experimental techniques and setups for ML studies focused on various mechanical stimuli. Subsequently, the performance, sensitivity, and credibility of the designed setups are scrutinized using multiple well-known, commercially available phosphor materials ($CaAl_2O_4:Eu^{2+},Dy^{3+},La^{3+}$, $SrAl_2O_4:Eu^{2+},Dy^{3+}$ and $Sr_{0.95}Ca_{0.05}(SO_4):Mn$). After validating the setup's performance, comprehensive experimental analyses of the ML, Us-L and TL properties of $LiTaO_3$:Pr were conducted to understand the underlying light emission mechanisms and explore their industrial applications in mechanical stress sensing, ultrasonic sensing and luminescence thermometry. Additionally, other luminescence materials previously studied by our group or collaborators, such as $SrSi_2N_2O_2$:Eu, $SrSi_2N_2O_2$:Eu,Mn, AlN:Mn and ZnS:Mn, were also examined in this work for their ML and Us-L behaviors, complementing earlier studies on their luminescence, PersL, and thermoluminescence properties.

During the investigation of luminescence and thermoluminescence properties of $LiTaO_3$ with different Pr dopant concentrations, it can be found that these materials exhibit modulation in the trap's energies and densities by varying Pr concentration. Moreover, we noted that it emits also infrared light within the first biological window (NIR-I), rendering it valuable for medical applications. Following an extensive literature review, it became apparent that $LiTaO_3$ remains largely unexplored in terms of ML and Us-L studies. Consequently, this knowledge gap motivated us to investigate the ML and Us-L properties of $LiTaO_3$ host material doped with various concentrations of Pr. It can be observed that varying amounts of Pr dopant influence the concentration and excitation energy of distinct traps, which can be used for revealing the diverse behaviors of ML and Us-L. The ML measurements are conducted at different mechanical stimulation and experimental conditions. Three distinct ML experimental setups, namely Friction-induced ML, Impact-induced ML, and Stress-induced ML were utilized to examine their ML properties. F-ML measurements are performed to measure the ML spectra of $LiTaO_3$:Pr. I-ML is utilized to exhibit their mechanical impact detection capabilities at various impact kinetic energies and ML recoverability. S-ML experiments are performed to study the correlation of ML intensity curves with the time-dependent applied force. However, Us-L measurements are performed at low (20 kHz) and high frequency (3.3 MHz) Us waves with multiple parameter selection and at various environmental temperatures to observe a complete set of information regarding the properties of $LiTaO_3$:Pr under the influence of diverse mechanical action and ultrasound waves. Moreover, ML and Us-L properties of single doped oxynitridosilicate $SrSi_2N_2O_2$:Eu, Mn co-doped $SrSi_2N_2O_2$:Eu, AlN:Mn and ZnS:Mn were studied. These materials exhibit prominent luminescence properties, including strong PL emission, effective trap formation, and high quantum yield efficiency, making them ideal candidates for investigating their ML and Us-L characteristics. This allows them to demonstrate their potential as good contenders for optical-based mechanical and ultrasonic sensors.

1.2 Outline of the Thesis

Chapter 2 gives a brief historical overview of ML phenomena and their classification. Various luminescent materials that exhibit ML properties are documented, along with demonstrations of ML applications in various commercial domains. The last section of chapter 2 offers a comprehensive review of several experimental setups and techniques used in ML studies, drawing from published literature. A portion of this chapter is published in the book “Specialist Periodical Reports-Nanoscience: Volume 10”.

Chapter 3 details the construction and operation of newly self-designed experimental setups for I-ML, S-ML, and Us-L studies. It provides comprehensive information, from the individual components to the functioning of the setups, which will be valuable for future utilization and design considerations. Moreover, the calibration and functioning of the setups are tested by employing various known phosphor materials. A portion of this chapter has been published in "Measurement" (doi.org/10.1016/j.measurement.2022.112012).

Chapter 4 offers comprehensive luminescence and mechanoluminescence studies on synthesized $LiTaO_3$:xPr (x=1%, 3%, and 5%) samples. It presents detailed information on the synthesis process, structural analysis, and luminescence characterization. Additionally, this chapter highlights intriguing findings regarding the modulation of I-ML and S-ML properties of $LiTaO_3$:Pr by varying the concentration of Pr dopant. A portion of this chapter has been published in "The Journal of Physical Chemistry C" (doi.org/10.1021/acs.jpcc.3c06434).

Chapter 5 consists of the study of ultrasound-induced luminescence properties of $LiTaO_3$:Pr at low (20 kHz) and High (3.3 MHz) Us frequency setups under various environmental conditions and experimental parameters. Moreover, it presents experimental results that exhibit the correlation between the trap system (concentration, depth) and Us-L properties. There is an intention to publish the results of this chapter as a journal article.

Chapter 6 contains the analysis of the thermal anti-quenching behavior of $LiTaO_3$:Pr. Furthermore, it explores the application of this behavior for luminescence thermometric properties. Additionally, this chapter includes a comparison of the luminescence thermometric parameters of the materials studied in this work with those reported in previously published research.

Chapter 7 comprises results of comprehensive studies on mechanoluminescence properties of single doped oxynitridosilicate $SrSi_2N_2O_2$:Eu, Mn co-doped $SrSi_2N_2O_2$:Eu, AlN:Mn and ZnS:Mn materials. Furthermore, this chapter presents interesting findings concerning the experimental results of I-ML and Us-L at 20 kHz and 3.3 MHz frequency ranges. A portion of this chapter has been published in "Journal of Materials Chemistry C" (10.1039/D4TC00960F). Moreover, there is an intention to publish some other results of this chapter in other journal articles.

Chapter 8 concludes the thesis with a summary of mechanoluminescence studies on various materials and their applications. Additionally, this chapter presents a forward-looking idea that could significantly benefit future mechanoluminescence research.

CHAPTER 2. Mechanoluminescence

In this chapter, we explore the phenomenon of Mechanoluminescence, which is exhibited by various solid materials that emit light under mechanical stress and physical deformation. Its brief history, classification, mechanism, and materials exhibit ML, as well as its applications are discussed. Additionally, we delve into the construction and operation of various experimental techniques and setups used in ML studies. In most cases, the intensity of emitted ML light is directly proportional to the applied mechanical stress, creating a wide range of applications in automotive, turbines, and robotics for stress sensing. It is also used for visualizing stress distribution in metal plates, analyzing stress detection in synthetic bones and joints, detecting invisible defects and cracks in metal assemblies, and imaging crack propagation in infrastructure for health diagnosis, among other applications.

2.1. Brief historical background:

Various materials emit light when subjected to mechanical stress, a phenomenon known as Mechanoluminescence [39, 40]. ML is a highly interesting and complex phenomenon in which the emission of light occurs as a consequence of the applied mechanical stimuli to the sample, utilized to unveil the invisible stress and its transformation (refer to Figure 2.1.1 (a) & (b)). Although it was initially discovered in the 16^{th} century, still researchers are engaged in the exploration and authentication of several proposed theoretical models for a reliable explanation. Diverse behavior and categories of ML are the primary hurdles to an effective explanation of its occurrence. About four hundred years ago, Francis lord Bacon recognized ML phenomena as 'it is not the property of fire alone to give light…loaf-sugar in scraping or breaking' in his book 'Of the Proficiency and Advancement of Learning, Divine and Human [41, 42]. In 1684, Richard Waller also witnessed that a substance like rock salt, sugar loaf, and white sugar was ground in a mortar, it "gives such intense light that the sides of the mortar and shape of the pestle could distinctly be displayed" [43]. Another scientist, Thomas Wedgwood (1792) stated that many crystal substances such as quartz, ruby, and diamond exhibit good ML [44]. Later, Jeffery I. Zink et al. in the research article "Triboluminescence of sugars" described the reason behind the triboluminescence phenomena of sugar as molecular nitrogen and also captured its fractoluminescence spectra that have multiple emission bands of violet-blue color between 300 to 410 nm [45]. Most probably the light sparkle observed by Francis Bacon during the breaking of hard sugar was violet-blue color fractoluminescence. B. P. Chandra documented an article on a survey of ML from 1605 to 2013, validating the emergence and popularity of ML studied among material scientists, medical scientists, physicists, chemists, engineers, technologists, geologists, and other researchers [46]. The statistical analysis reveals the enhancement of research activities in the ML domain (see Figure 2.1.1 (c)).

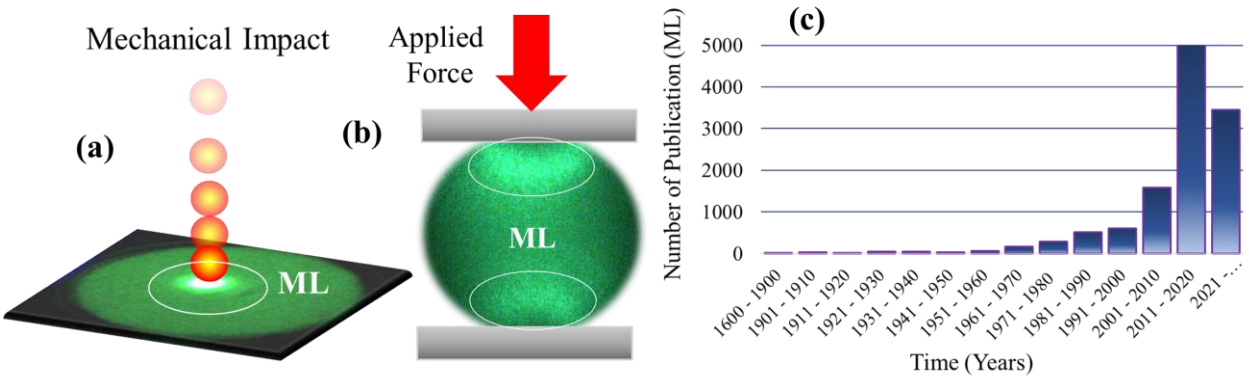

Figure 2.1.1: The schematic illustration of ML with experimental images under the application of (a) abrupt mechanical impact (by impact-induce ML setup), (b) applied mechanical force (by stress-induce ML setup) and (c) the bar plot exhibiting statistical survey of the literature on mechanoluminescence from 1600 to the present (source: Web of Science).

2.2. Classification:

Mechanoluminescence is a term proposed by B.P. Chandra to describe the emission of photons resulting from physical stimuli applied to a material [47]. The applied mechanical deformation can take various forms, including twisting, bending, compression, stretching, dragging, grinding, fracturing, or splitting. The correlation between the intensity of the emitted ML and the magnitude of the mechanical deformation depends on the nature of the materials and the type of mechanical action applied. Consequently, ML phenomena are broadly classified into three subdivisions: triboluminescence, fractoluminescence, and deformation luminescence (see Figure 2.2.1 (a)).

Triboluminescence is caused by contact or separation between the surfaces of two different but identical materials. It is further classified into electrically induced, chemically induced, and thermally induced triboluminescence based on the type of triggering energy. On the other hand, deformation luminescence and fractoluminescence are different from triboluminescence and result from mechanical impacts or stimuli applied to the material. Intense mechanical stimuli can lead to plastic deformation and eventual fracture of the specimen. Below the fracture limit, ML is directly proportional to the applied mechanical stress representing deformation luminescence. It is further divided into two subcategories: elastic luminescence and plastic luminescence. When mechanical stress is applied to ML materials, three stages can be observed. In the initial stage, the stress increases linearly with strain within the deformation range, resulting in a linear increase in ML intensity, known as elastic luminescence. Then, at a certain limit, the stress saturates, resulting in a saturation of the ML intensity, known as plastic luminescence. In the final stage, when large mechanical stress causes cracks in the material and the stress level decreases abruptly, a spark of intense light is observed, termed fractoluminescence (see Figure 2.2.1 (b)).

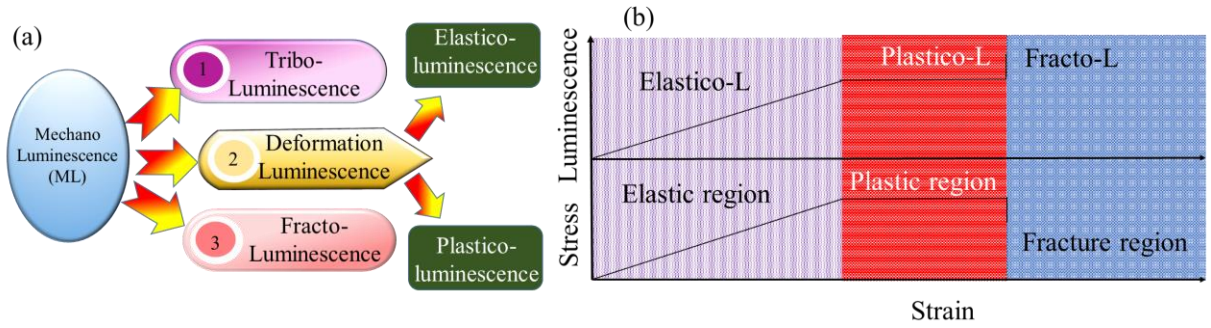

Figure 2.2.1: (a) Schematic illustration of subdivision of mechanoluminescence and (b) the comparison of stress and ML vs. strain graphs in different deformation regions.

2.3. ML materials and their applications:

Stress or strain sensing has traditionally been performed using various electrical signal techniques, such as electrical resistance strain gauges and piezoelectricity [48, 49]. In these methods, mechanical stress and strain are detected as electrical signals. However, these approaches have limitations, including large detector sizes, the need for electrical contacts, and the need for electrical power to operate. As a result, detecting stress in micro-sized specimens or without electrical contact with the specimen using these methods is challenging. ML-based stress sensors offer a promising alternative due to their unique ability to directly convert the impact of applied mechanical action into visible light. These sensors are self-powered by pre-irradiated ultraviolet or visible light and do not require physical contact with the sample. In general, about half of inorganic and one-third of organic materials exhibit ML after energy storage in the form of charge carriers trapped in trap levels through exposure to UV or high-energy radiation, or even without pre-exposure [40]. The mechanisms underlying the ML process are complex and vary depending on the category of ML materials. For simplicity, researchers have classified ML materials into two types based on their reproducibility: trap-controlled and non-reproducible materials [10, 50-52]. Inorganic materials doped with transition metals or lanthanide ions exhibit reproducible ML, known as trap-controlled materials. These materials function similarly to energy storage devices, being remotely charged by exposure to a UV excitation source. Mechanical impact then causes the stored charges to be released (charge carriers from the trap states) in the form of photon emission (by recombination of released charge carriers). During UV exposure, some of the excited carriers are trapped at levels between the valence and conduction bands, called trap levels. These trap levels are created by dopants and various defects in the crystal lattice. Among these traps, some are shallow and require low activation energy, while others are deep and require high activation energy to release the trapped charge carries. PersL is associated with shallow traps, while ML can originate from both shallow and deep traps, depending on the time delay between turning off the UV excitation and applying mechanical stress (see Figure 2.3.1 (a)). The delay between UV exposure and measurement in the dark is significant. Most carriers are released from both shallow and deep traps, sometimes via shallow traps, due to excitation by thermal energy at room temperature. In addition, the ambient temperature affects ML phenomena. In general, the detrapping is linearly dependent on the energy of the applied mechanical stimuli, with two nonlinear regions at low and high energy levels [10, 51-53] (see Figure 2.3.1 (b)). Based on trap formation, these materials are divided into two groups. In the first group, traps are created by controlling the composition of reactant and dopant impurities and by changing the material

synthesis technique during the preparation process. Some examples are $SrAl_2O_4:Eu^{2+}$, Dy^{3+} [54], $Sr_2MgSi_2O_7:Eu^{2+}$ [55], $CaAl_2Si_2O_8:Eu^{2+}$ [56], $LiTaO_3:Pr^{3+}$ [57] , $LiNbO_3:Pr^{3+}$[58], and so on. However, another group has high energy treated alkaline earth oxides, alkali halide crystals, and salts. For example X- or γ-irradiated NaCl [59], $K_2Mg_2(SO_4)_3:Dy^{3+}$ [60], KCl:Cu [61], $CaSO_4:Sm^{3+}/Mn^{2+}$ [62], CaF_2:Er [63], $Al_2O_3:Tb^{3+}$ [64] etc. In this group, trap levels are intentionally created by irradiating the original material (without traps) with high-energy particles and photons, which are essential for the ML properties. Table 2.3.1 provides information on common ML host materials, including dopant, space group, and emission wavelength details.

Host	Dopant	Space group	ML wavelength (nm)	Ref.
$LiTaO_3$	Pr^{3+}, Gd^{3+}	R3c	511, 618	[57]
	Pr^{3+}, Ca^{2+}, Si^{4+}		511, 616	[65]
$LiNbO_3$	Pr^{3+}, Gd^{3+}	R3c	618, 635	[58]
	Nd^{3+}		895	[66]
ZnS	Mn^{2+}	P6mm	587	[67, 68]
	Cu		517	[67, 69]
$Sr_2MgSi_2O_7$	Eu^{2+},Dy^{3+}	$P42_1m$	480	[55, 70]
	Eu^{2+},Ce^{3+}		465	[71]
$Ca_2MgSi_2O_7$	Eu^{2+}	$P42_1m$	530	[17, 72]
$Ba_2MgSi_2O_7$	Dy^{3+}	$P42_1m$	481, 572, 672	[73]
	Eu^{2+},Dy^{3+}		505	[74]
	Ce^{3+}		400	[75]
$SrBaMgSi_2O_7$	Eu^{2+}	$P42_1m$	440	[19]
$SrCaMgSi_2O_7$	Eu^{2+}	$P42_1m$	499	[19]
$SrAl_2O_4$	Eu^{2+},Dy^{3+}	$P2_1$	520	[54, 76]
$CaAl_2O_4$	Tb^{3+}	$P2_1$	495, 550	[77]
$CaAl_2O_4$	Eu^{2+}	$P2_1$	455,606	[78]
$ZnAl_2O_4$	Eu^{2+}	Fd3m	606	[79]
	Mn^{2+}		512	[80, 81]
$Ca_2Al_2SiO_7$	Ce^{3+}	$P42_1m$	402, 427	[21, 22]
	Eu^{3+}		589, 619	[82]
$SrSi_2N_2O_2$	Eu^{2+}	P1	540	[83]
$BaSi_2N_2O_2$	Eu^{2+}	$Cmc2_1$	498	[84]
$MgGa_2O_4$	Mn^{2+}	Fd3m	506	[85, 86]
$ZnGa_2O_4$	Mn^{2+}	Fd3m	505	[86]

Table 2.3.1: The important information about some known ML materials in tabular form.

ML materials offer a wide range of potential applications in various engineering and medical fields, as shown in Figure 2.3.1(c) [12, 13, 25, 53, 74, 87-98]. They have been developed for use as mechano-optical indicators and sensors to analyze stress transformation and measure the magnitude of applied mechanical impact. ML-based stress sensors find applications in automotive, turbines, and robotics for stress sensing [69], visualization of stress distribution in a metal plate [25], analysis of stress detection within synthetic bones and joints [27], detection of invisible defects and cracks in metal assembly [99], imaging the crack propagation in

infrastructure for health diagnosis [100], etc. A study by Chengzhou Li et al. visualized the dynamics of axial force during bolt tightening were visualized using an ML composite material. A $SrAl_2O_4$:Eu/polymer film was applied to the washer for force sensing. During the experiment, the authors measured ML intensity and axial force simultaneously under different conditions and observed a linear dependence between them [90]. In another approach, G. W. Kim et al. used a similar material to record torque in a shaft coated with a ML composite [101]. Several studies have highlighted the advantages of ML for visualizing rapid crack propagation in various engineering domains [102-106]. These techniques are much faster than the other conventional crack monitoring methods [107-109]. These ML materials are useful for analyzing the stress/strain distribution in metals [110, 111]. In one of the studies, $SrAl_2O_4$:Eu composite film was applied to an aluminum plate with a drilled hole. During stress application, optical images of the specimen were captured using a high-speed CCD camera. The extracted images were compared with numerical analysis, which confirmed a linear relationship between the intensity of the ML sensing film and the stress on the metal surface [25]. In another innovative study, Xu's group used the aforementioned materials to image stress distributions in artificial bones and joints under compressive loading [88].

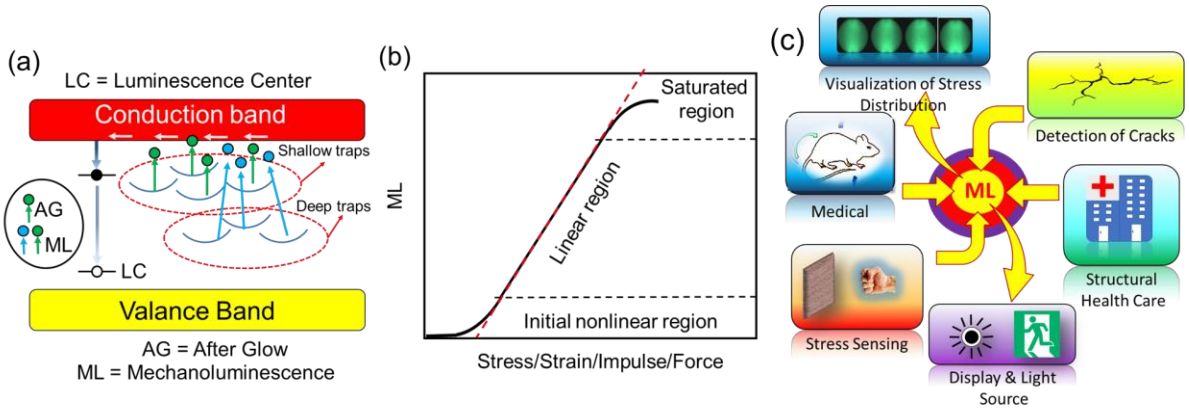

Figure 2.3.1: Schematic illustration of (a) proposed ML mechanism, (b) relationship between ML and applied stress, strain, or impulse at different regions, and (c) ML-based applications in different scientific fields.

2.4. Experimental Setups and Techniques:

There are two different approaches to measuring ML characteristics: (i) ML intensity measurements and (ii) ML spectral measurements. Despite the differences in measurement techniques, the basic principle underlying any experimental method for measuring ML remains the same. First, mechanical stimuli are applied to ML material-based specimens in various forms, including compression [112], stretching [113], bending [114], needle impact [115], air blast [116], scratching [117], ball shooting [92], grinding and milling [47]. Concurrently, ML are captured using devices such as photomultipliers, spectrometers, optical cameras, etc.

2.4.1. Impact-induced ML:

In this section, we discuss several impact-induced ML setups designed to generate ML through abrupt impact forces. Typically, these forces are generated by dropping or shooting an

object of appropriate mass from a certain height or distance. The first example is the drop tower apparatus developed by Ross S. Fontenot et al. [118], This original apparatus consists of fiberboard, Plexiglas panels, and a long PVC pipe. The PVC pipe has holes drilled into it at uniform incremental heights to represent the average drop interval. A standard pin bar is used to hold and release a mass at a given height. In this setup, an ML phosphor is mounted underneath a Plexiglas plate, layered thinly to minimize thickness, and positioned under the hole at the opening of the PVC pipe (see Figure 2.4.1.1(a)). A ball weighing approximately 130 g is placed 1.1 m above the material. When the pin is pulled, the ball hits the material, generating ML. To measure the ML, a PD detector is positioned below the sample plate. The signals are recorded in single-sequence mode on an oscilloscope and analyzed using LabVIEW software, which integrates the area of the curve and measures the emission decay time. However, when measuring ML spectra, the PD is replaced by the spectrometer controlled by SpectraSuite software. The spectra are recorded as shown in Figure 2.4.1.1(b). After recording, LabVIEW code processes the files generated by SpectraSuite to determine the ML light yield and spectral peak position. For troubleshooting or demonstration purposes, the detectors can be removed and mirrors placed at a 45˚ angle under the drop-tower setup so that the observer can easily observe the ML with the naked eye. Figure 2.4.1.1(c) shows three ML images of a Mn-doped ZnS sample captured by a high-speed camera at a high frame rate.

ML spectra are obtained with an integration time of 100 ms. To confirm reliability of ML spectra, hundreds of different files are recorded. For efficiency, a specialized LabVIEW code called the Spectrum Finder is designed to locate files containing SpectraSuite data. This code queries the handler for file locations, scans file descriptions, and displays file numbers and data in graphical order (see Figure 2.4.1.1(d)). The handler can then navigate through the files using keyboard arrow keys. Once the ML spectrum is identified, the handler notes the file number, which is then opened in SigmaPlot or other emission spectrum plotting software. This setup is versatile and serves both ML spectra and ML intensity decay measurements as a function of time.

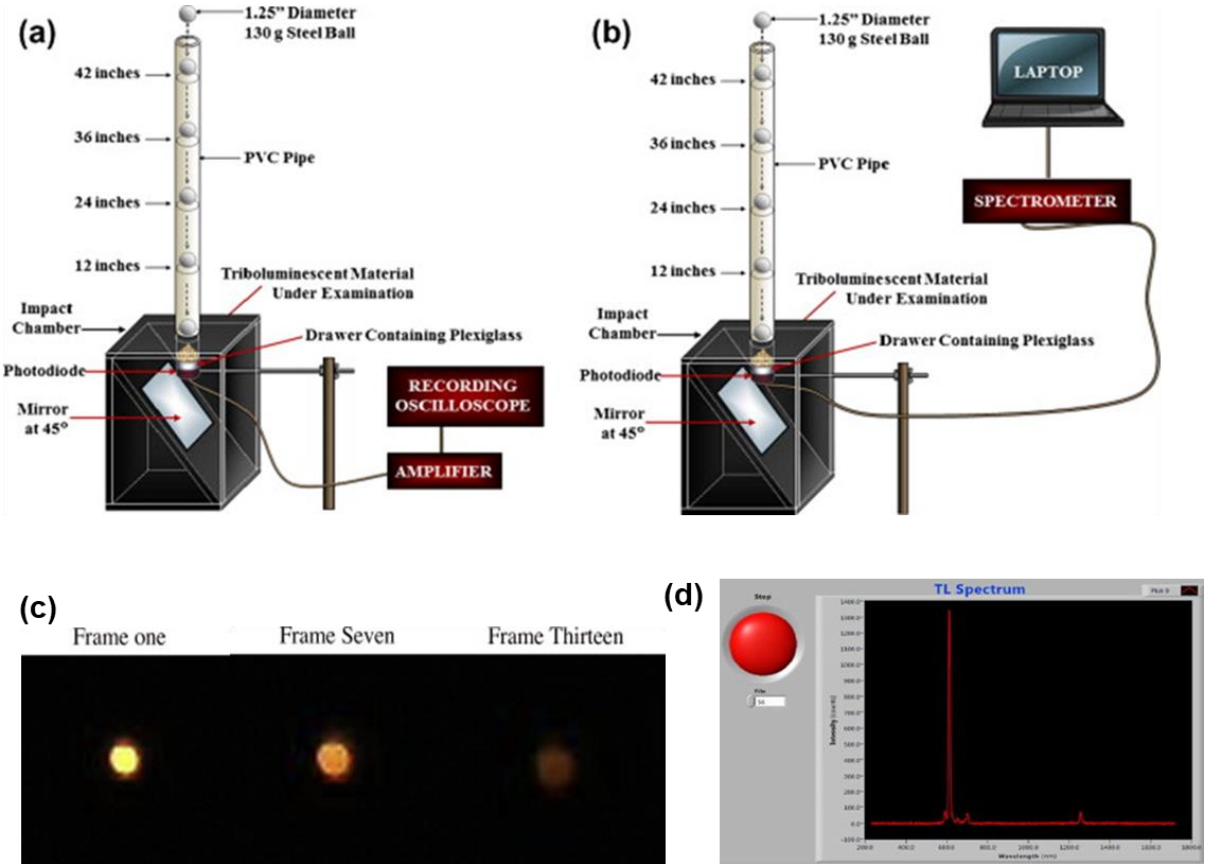

Figure 2.4.1.1: The schematic illustration of the I-ML setup based on the drop tower technique: (a) integrated light yield and (b) visible ML spectrum acquisition. (c) ML images of ZnS:Mn sample that was obtained from the drop tower setup with the help of NAC GX-1 video camera at 1000 Hz frame rate while ML was visible up to 19 frames. (d) Front panel display of the LabVIEW code-named Spectrum Finder. The figure is taken from Ref. [118].

Another experimental setup based on a similar principle has been designed by T. Z. Zhan et al., as illustrated in Figure 2.4.1.2(a) [119]. In this setup, a ZrO_2 sphere is dropped from a height of 2.5 cm onto a sample film deposited on a transparent rubber plate. The ball is released onto the film at zero initial velocity. The intensity of the impact-induced ML is then measured using a photon multiplier module. Prior to measurement, the sample film is exposed to ultraviolet light to fill the traps with charge carriers. To minimize error and ensure accuracy, the experiment is performed five times. In many experiments, the standard deviation is less than 10%. The luminescence of the sample is captured by a CCD camera. Figure 2.4.1.2(b) shows the I-ML signal for both Si-irradiated and non-irradiated areas of the $CaSrAl_2Si_2O_8:Eu^{2+}$ material. It is observed that the I-ML intensity from the irradiated area is significantly stronger than that from the non-irradiated area by about one order of magnitude and is easily visible to the naked eye. The experimental results confirm the effectiveness of the designed setup.

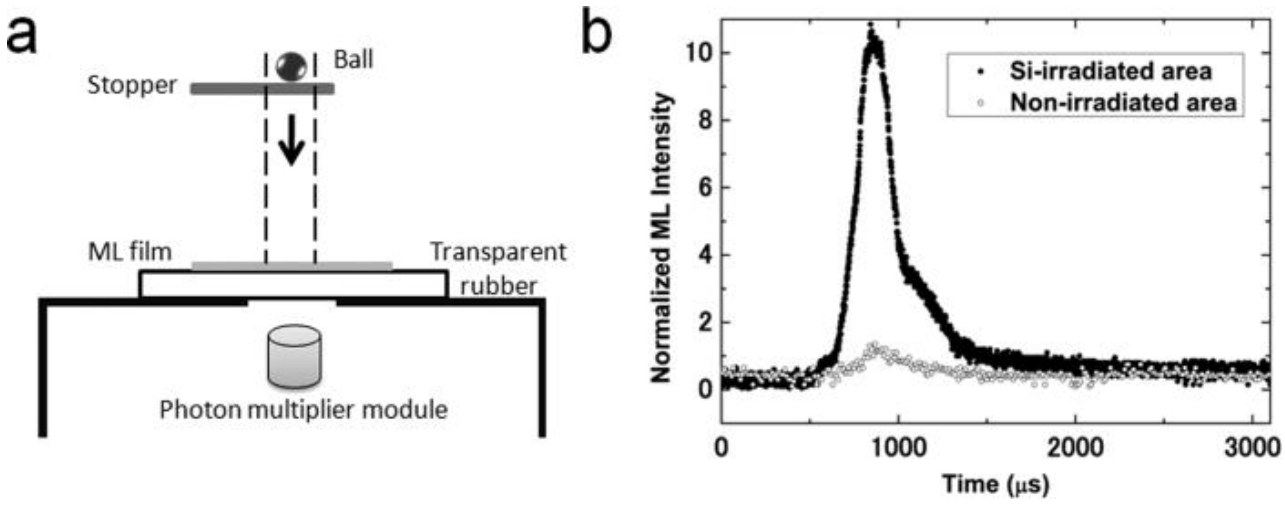

Figure 2.4.1.2 (a) The schematic representation of the I-ML apparatus based on mass dropping (b) I-ML curves for Si irradiated and non-irradiated areas. The figure is reproduced from Ref. [119]

Ishwar Prasad Sahu developed another I-ML setup for ML studies based on impulsive deformation [120]. The measurements start with the dropping of a mass object from a variable height, resulting in different impact velocities due to the gravitational potential. In the measurements of ML properties of $Ca_2MgSi_2O_7:Dy^{3+}$,R (R= Li^+, Na^+ and K^+), a cylindrical moving piston with a mass of 400g was used. A sample powder was dispersed on a transparent Lucite plate placed inside the sample holder under the guide cylinder. The top of the sample was then completely covered with aluminum foil and secured with adhesive tape. The aluminum foil serves two purposes: (i) it reflects the ML light, and (ii) it prevents the sample powder from dispersing throughout the setup during piston collision. This setup also minimizes experimental errors caused by powder scattering during ML signal measurement. The housing is made of thick soft iron to block light and magnetic field interference during ML measurements. A slit in the window allows the size of the window opening to be adjusted to accommodate the incident light beam. In this setup, the impact velocity (v_0) can be varied by adjusting the vertical displacement (h) between the piston drop position and the sample position on the Lucite plate. A pulley and guide cylinder were used to reduce friction, and a classical physics formula ($\sqrt{2gh}$) was used to calculate the impact velocity, where g is the acceleration due to gravity. To capture the ML, a photomultiplier tube (PMT) was mounted directly below the Lucite plate. This PMT is connected to an oscilloscope to display the ML signal. Given the response time of the PMT system of approximately 5 μs, the extracted plots from this study show a linear correlation between impact velocities and peak ML intensities for a prepared batch of $Ca_2MgSi_2O_7:Dy^{3+}$,R (R^+= Li^+, Na^+ and K^+) samples. The recorded ML intensity of these samples increases linearly with the applied mechanical stress. Notably, $Ca_2MgSi_2O_7:Dy^{3+},Li^+$ exhibits a superior ML intensity with a larger slope compared to its counterparts [121].

2.4.2. Stress-induced ML:

Another approach used by scientists to measure ML properties is the application of mechanical stress by tensile testing machines, known as stress-induced ML setups. Here, we introduced the self-designed S-ML setup by Xiaoyan Fu, et al.'s used to measure the ML properties of $Sr_nMgSi_2O_{5-n}$:Eu ($1 \leq n \leq 2$) (SMSE) as shown in Figure 2.4.2.1(a) [122]. This setup consists of a universal testing machine and a photon detector for photon counting connected to a computer system. Additionally, a spectrometer is attached to the setup for measuring ML spectra. To measure the ML properties of the phosphors, identical composite disks (thickness = 15 mm, diameter = 25 mm) were prepared by mixing phosphor materials with optically transparent epoxy resin. This polymeric material serves as a stress transfer medium for the phosphors. Figure 2.4.2.1(c) shows the ML curve of the SMSE phosphors obtained using this setup. A broad emission spectrum peak at about 460 nm is observed, which is consistent with the PL spectra of $Sr_2MgSi_2O_7$:Eu (a), $Sr_{1.6}MgSi_2O_{6.6}$:Eu (b) and $SrMgSi_2O_6$:Eu (c) excited at 365 nm (see Figure 2.4.2.1(b)). The results confirm that ML is emitted from the same luminescence center (Eu^{2+} ion) as PL, which results from the transition of Eu^{2+} ions from the excited state ($4f^6\,5d^1$) to ground state ($^8S_{7/2}$ ($4f^7$)). The present study suggests the appropriate use of the mentioned setup for S-ML studies.

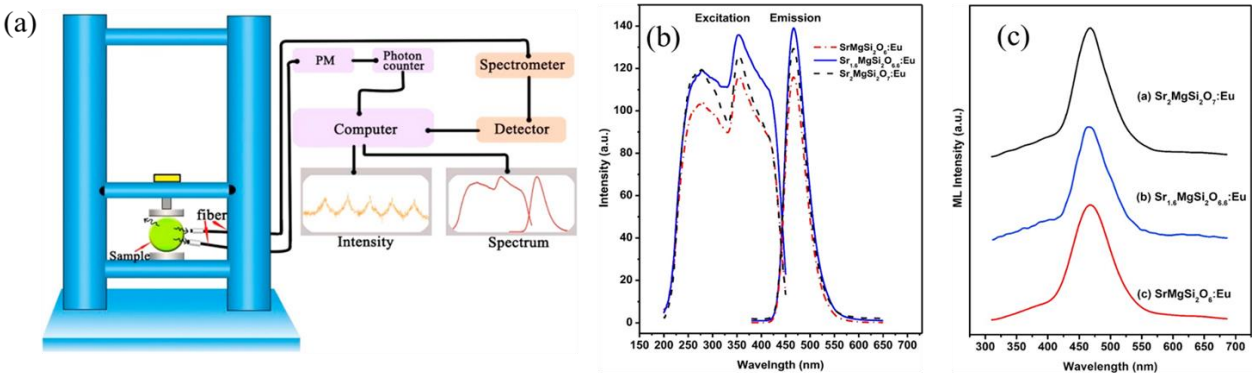

Figure 2.4.2.1(a) Schematic diagram of the S-ML setup, (b) emission and excitation spectra, and (c) ML spectra of $Sr_nMgSi_2O_{5-n}$:Eu ($1 \leq n \leq 2$) samples. *The figure is taken from Ref.* [122].

2. 4. 3. Friction-induced ML:

To study friction-induced ML, Justyna Barzowska et al. designed a finely calibrated setup [83]. In this setup, the mechanical stimulation of the sample is carried out by sliding a glass rod, pressed against the sample plate with a specified force. The sample is sandwiched between two layers of 25 μm polypropylene sticky tape and fixed on a sapphire plate. A uniformly coated layer of the sample is spread over an area of 6 × 28 mm^2 with a thickness of approximately 30 μm. The uniformity of the thickness is confirmed by the uniform luminescence distribution over the entire sample surface. When the glass rod is pressed onto the sample, the applied force creates a contact area of 0.03 mm^2. The glass rod is then dragged along the edges of the sample with a constant contact force, resulting in F-ML. The spectra of light emitted by the sample during subsequent time intervals are recorded using a Shamrock 500i spectrometer equipped with an iDus420 CCD camera (Andor Technology). The time evolution of the emission intensity for the chosen

wavelength range is then calculated from the acquired spectra. Depending on the type of F-ML experiment, the sample plate is either fixed or moved vertically. This process provides measurement points for the F-ML signal from newly exposed areas of the previously irradiated sample. The irradiation time, waiting time after irradiation, the force applied to press the rod against the sample, and the parameters of the rod movement, such as range of motion, speed, repetition, and frequency, are all controlled by dedicated, custom software in LabVIEW. The example of experimental results of F-ML measurements performed with this setup on $SrSi_2N_2O_2$:Eu samples (synthesized with the different synthesis procedure) is shown in Figure 2.4.3.1. The ML caused by the rod dragging across the sample plate was recorded against the background of the time-fading PersL signal. The intensity vs. time curves for samples B and E during mechanical loading (red and cyan lines, respectively) and without mechanical loading (black line) for comparison. During the measurements, the rod was dragged across the sample surface four times at the same location with a contact force of 25 N. The moments when the rod moved on the sample, and ML became observable are indicated by the arrows above the curves. The inset graph in Figure 2.4.3.1 illustrates the relationship between applied force and F-ML intensity. This result confirms a linear relationship between F-ML intensity and applied contact force for both samples, with a steeper slope for sample E, indicating higher sensitivity to mechanical loading compared to sample B. Using the functionality of the described F-ML setup, which enables the measurement of ML, PersL, and PL spectra in the wavelength range of 400–1000 nm, it was applied to studies aimed at comparing ML spectra with PersL and PL spectra for the samples investigated in this dissertation [4, 124].

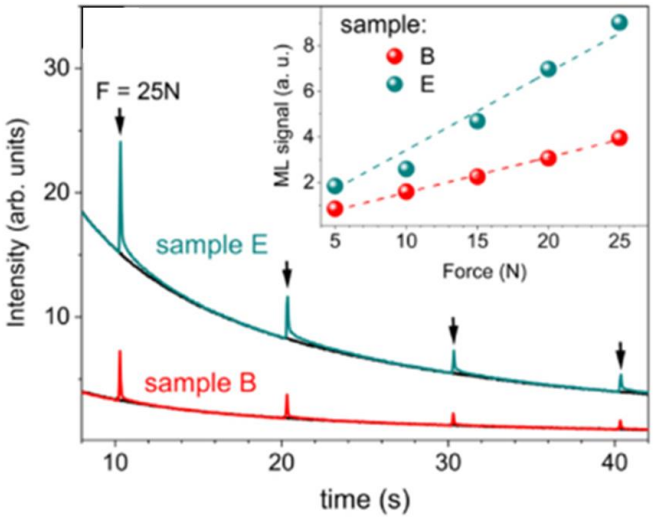

Figure 2.4.3.1: Comparison of the time evolution of the intensity of light emitted by samples B and E after the cessation of 2 minutes of irradiation with 254 nm light. Signals measured without mechanical stimulation (PersL) are plotted with black curves, while signals measured with the sequence of mechanical loading are plotted with a red curve for sample B and a dark cyan curve for sample E. The time when a force of 25 N was applied is marked with arrows. Inset: the dependence of ML intensity induced by the first mechanical load on the applied force. The figure is taken from Ref. [83].

2.4.4. Ultrasound-induced Luminescence:

Various experimental setups have been designed by different researchers to study ultrasound wave induced luminescence. Two explanations have been proposed for Us-L: the first suggests that applied Us waves create mechanical stress in the exposed region, leading to ML, while the second posits that Us waves increase the temperature of the region, leading to thermoluminescence. Here, we present the approach of Tianzhuo Zhan et al. to study the ultrasonically induced ML properties of various materials. First, they designed a special system consisting of a single-element piezoelectric transducer vibrating at a frequency of 20 MHz and an ultrasound pulse receiver with user-controllable pulse energy, pulse frequency, and attenuation parameters. A photon counting system and a CCD camera were used to measure ML intensity and distribution, respectively. To demonstrate the medical application of this technique, ML measurements were performed by interposing a scanning gel between the ML sensing film and the transducer surface. This gel facilitates the transmission of ultrasound energy from the transducer to the ML sensing film by matching the acoustic impedance. The thickness of the ML film is 0.20 mm, which is approximately three times the wavelength (0.076 mm) of the ultrasound. A photon counter and a high-speed CCD camera are positioned above the ML sensing sample. The entire setup is schematically shown in Figure 2.4.4.1(a) and is connected to a computer system. To investigate the correlation between ML intensity and applied ultrasound power for europium-holmium co-doped strontium aluminate, an epoxy ML sensing film was fabricated. During the measurement, the ML produced at different ultrasound output power levels was recorded by a photon counter. The results of this measurement showed a linear relationship between ML intensity and ultrasound output power, as shown in Figure 2.4.4.1(b). For more details, see the reference [28].

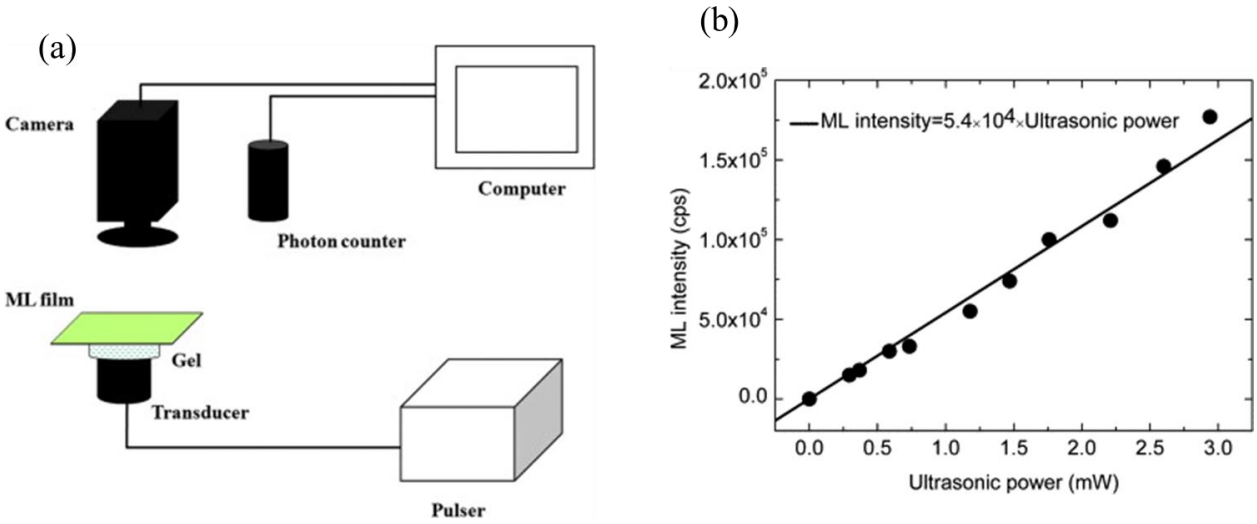

Figure 2.4.4.1: (a) Graphic representation of the setup for U-ML measurement and (b) ML intensity as a function of ultrasound power. The figure is taken from Ref. [28].

Simon E. Michels et al. also established another experimental setup to examine the Us-L properties of various materials [35]. In this approach, a piston transducer operating at 3.3 MHz with an output power ranging from 0.1 to 2.0 W/cm^2 was used. The Us-L generated by a sample during exposure to the Us beam was measured and visualized with a camera, while a

thermographic camera was utilized for thermographic visuals. The transducer (movable), and sample holder (fixed perpendicular to the Us beam) were positioned within the same rectangular water tank. The distance between the transducer and the sample could be adjusted from a few millimeters to 0.6 meters. A schematic illustration of the setup is presented in Figure 2.4.4.2(a). Initially, the sample membrane, as shown in Figures 2.4.4.2(b) and (c), prepared with PDMS, was irradiated with UV or blue light to trap charge carriers in the trap levels. Subsequently, the light emission was measured by a camera both in the absence (referred to as PersL) and presence of Us waves (referred to as Us-L). The results confirmed the emission of Us-L and demonstrated the effectiveness of the specially designed experimental setup, as depicted in Figure 2.4.4.2(d).

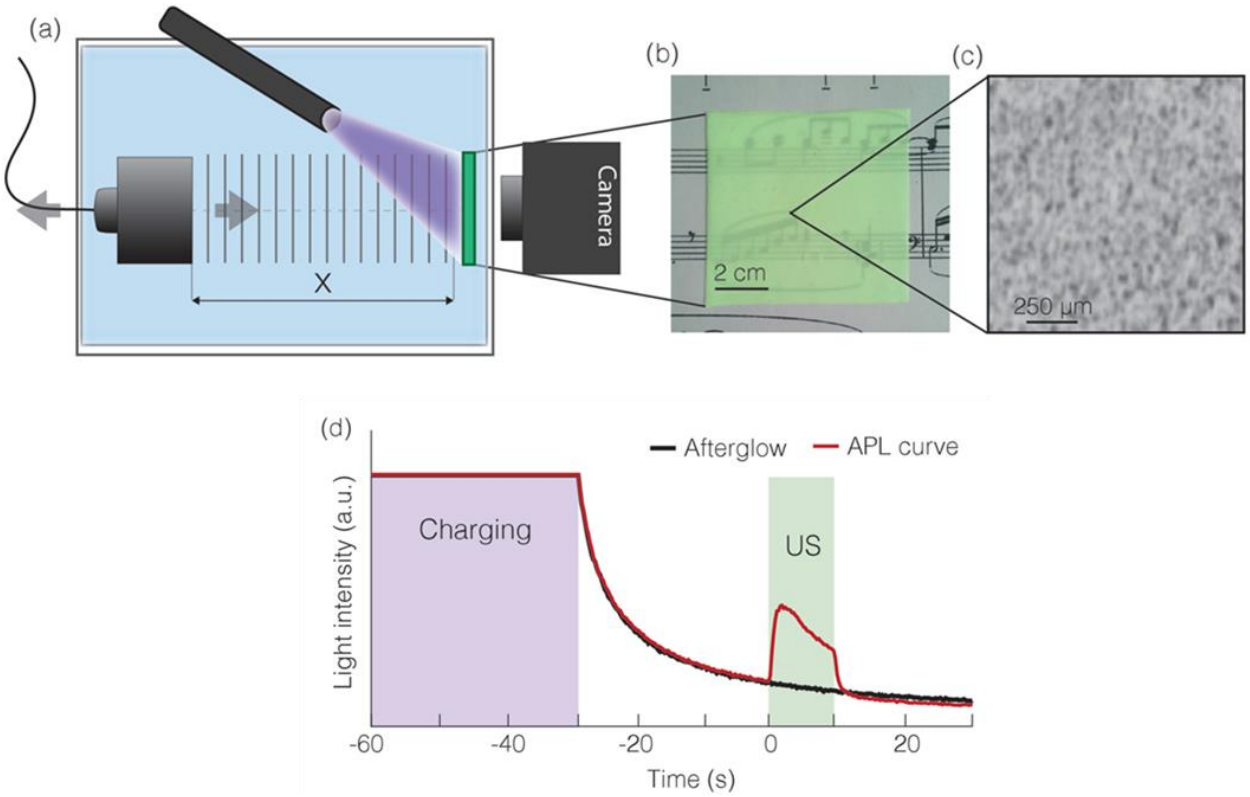

Figure 2.4.4.2(a) Schematic illustration of Us-L setup having a horizontally moveable transducer aimed at the sample membrane, while the emission of light is captured by a monochromatic camera outside the tank. (b) Optical image and (c) X-ray radiographic image of a sample membrane. (d) Plot of the Us-L measurement procedure. The afterglow of the sample membrane, after the turning of the excitation source is represented by a black curve while the red curve shows the afterglow in Us presence from t =0 to t = 10 s. The figure is taken from Ref. [35].

2.4.5. Atomic Force Microscopy (AFM) based:

Kazufumi Sakai et al. used a unique approach different from the previously mentioned techniques for ML measurements. They designed an experimental setup to measure ML from microparticles using an atomic force microscope. This setup can measure light emission by applying a small force to the microparticles, as illustrated in Figure 2.4.5.1(a) [123]. Initially, a glass slide with sample powder ($SrAl_2O_4$: Eu^{2+}) on its surface was placed on the piezo stage of the AFM. To make contact between the transducer and sample with a small force, the stage was moved

vertically along the z-axis. A photomultiplier tube equipped with an optical fiber was used to capture ML from the microparticles, and a photon counting method was employed to count the emitted photons. According to their findings, the number of photons emitted from a single particle was estimated to be several hundred based on the emission intensity of the bulk sample During the ML measurement, the particle size and position were first observed using the AFM. The transducer was then carefully positioned at the center of the particle, and force was applied using the force-curve measuring mode. Concurrently, the emitted photons were measured during the application of force. In the lithography mode, the transducer could be pressed and moved across the sample surface at a stable height. In this method, ML was produced by moving the transducer with a constant velocity of 1 mm/s, inducing friction over the surface of the $SrAl_2O_4$:Eu sample.

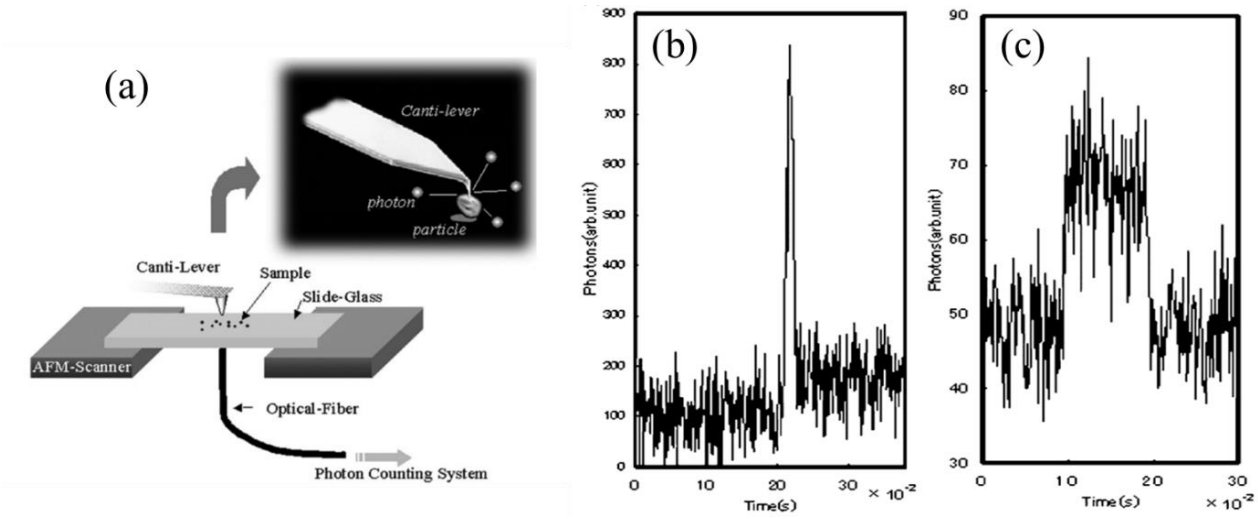

Figure 2.4.5.1(a) Schematic illustration of AFM-based ML measuring setup. (b) Destructive deformation emission during application of large force (c) Frictional ML in the lithograph mode during the movement of the transducer over the sample particles. The figure is taken from Ref. [123].

The graph presented in Figure 2.4.5.1(b) illustrates a sharp peak in ML during the destructive deformation of particles into various shapes due to an applied force (several μN). The radius of the tip, approximately 10 nm, results in an applied stress of tens of GPa, leading to the easy breakage of particles. This sharp peak demonstrates a highly intense ML from $SrAl_2O_4$: Eu^{2+} microparticles, which is consistent with previous ML studies of bulk samples as referenced in [12, 13]. Figure 2.4.5.1(c) shows stable and less intense ML lasting up to 0.1 s during the transducer movement of approximately 100 nm. An AFM image displays the trace of the transducer movement. The researchers hypothesized that the stable ML is caused by the partial destructive deformation of microparticles occurring during the transducer movement. The presented results validate the capability of the experimental setup to measure ML from microparticles with high sensitivity.

2.4.6. Diamond Anvil Cell based:

Hao Wang et al. adopted a distinct experimental approach to measure ML phenomena [124]. They utilized dDAC and a microsecond time-resolved fluorescence system with a

dispersive grating and a fast camera. The dDAC, operated by a piezoelectric actuator, permits varying the pressure at a rate ranging from 0.001 GPa/s up to 600 GPa/s. The experimental procedure initialized from the placing of micro-sized sample particles in a hole (order of 200 micrometers) drilled at the center of a metal gasket present between two parallel and opposite-directed diamond anvils. With the help of diamond anvils, high pressure is generated in the sample chamber. A micro-sized particle of ruby crystal is also situated with the tested sample in the gasket hole, utilized as a spectral pressure sensor. To produce hydrostatic pressure, a pressure-transmitting medium (like silicone oil, a mixture of methanol/ethanol, or nitrogen gas) is used in the sample chamber. Here, the diamond anvils serve as an optical transmission window for optical access to the sample chamber as well as for generating high pressure in the chamber by pressing the anvils toward each other. Hao Wang et al. measured ML of micron-sized grains of wurtzite ZnS:Mn^{2+}, Eu^{3+} using dDAC at various pressure and compression rates without any liquid pressure-transmitting medium. They observed an enormous increase in intensity and color change from yellow to red during various compression rates from ambient to 11 GPa presenting ML. Pressure-induced non-reversible phase transition of ZnS at a pressure near 15 GPa could affect ML. Moreover, authors take into account that luminescence properties of Mn^{2+} related to pressure-induced crossover between $^2T_2$ and $^4T_2$ states quenches luminescence from Mn^{2+} dopants due to increased. This dDAC setup can produce GPa pressures at several sweep rates by controlling applied voltages to piezoelectric actuators (see Figure 2.4.6.1(a)). According to their observation, ML spectra is in good agreement with PL spectra at a definite pressure (refer to Figure 2.4.6.1(b)). The ML exhibited by increasing pressure from 0 to 3 GPa at different rates is captured and presented in Figure 2.4.6.1(c). The extracted result reveals the ML properties of the ZnS: Mn^{2+}, Eu^{3+} can be visible at different rates and pressures. The described experiment proves an attractive use of a dDAC for studying ML, enabling the investigation of the ML properties of materials under dynamic and precisely controlled pressure conditions.

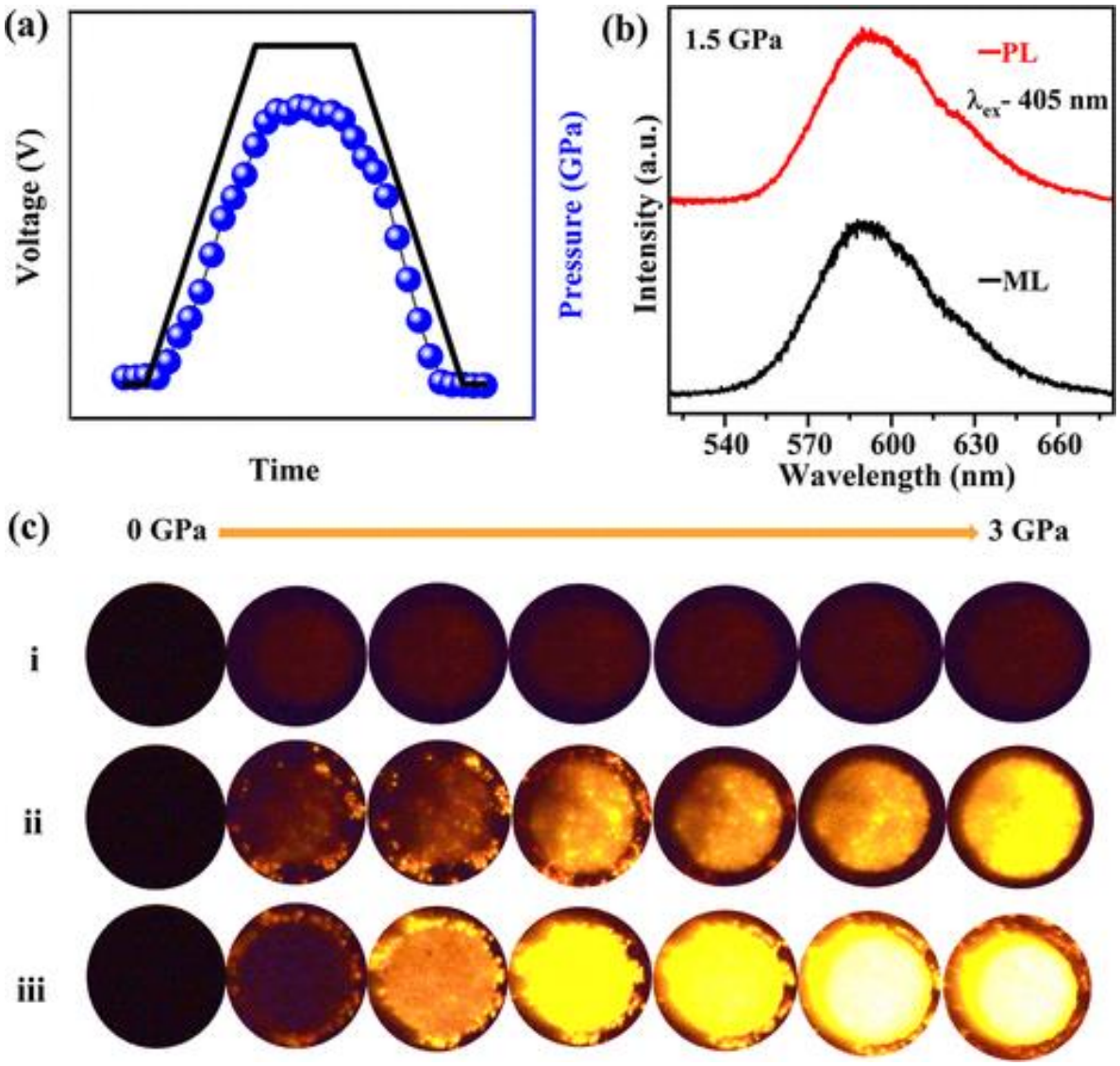

Figure 2.4.6.1 (a) Schematic illustration of time dependence of the voltage values (left y-axis) controlled the piezoelectric actuator movement and the generated pressure values (right y-axis) in the dDAC. (b) Comparison of the ML and photoluminescence spectra at pressure 1.5 GPa. (c) Images of ML of ZnS:Mn^{2+},Eu^{3+} in dDAC, taken at pressures increasing from 0 to 3 GPa, with compression rates of i) 0.3 GPa/s, ii) 1.2 GPa/s, and iii) 4.0 GPa/s. . The figure is taken from Ref. [124].

CHAPTER 3. Self-Designed Experimental Techniques and Setups

This chapter presents comprehensive details regarding the construction and functionality of three purposefully designed setups for ML studies. Each of these setups is developed by using unique and innovative approaches, accompanied by distinct technical specifications. Despite their individuality, these setups share some common components (refer to Table 3.1). Their significance is paramount in the establishment and advancement of a scientific laboratory dedicated to ML and Us-L studies.

<table>
<tr>
<td> 
Airsoft electric gun
(Model = CM122)</td>
<td> 
XCORTECH chronograph
(Model = X3200 MK3)</td>
<td> 
MadBalls plastic bullets
(diameter = 6 mm)</td>
</tr>
<tr>
<td> 

Sample holder for I-ML setup</td>
<td> 
Ultraviolet LEDs
(wavelength ~270 nm)
(Power 10 watt)</td>
<td> 
Photomultiplier tube module
(Model = H10721P-04)</td>
</tr>
<tr>
<td> 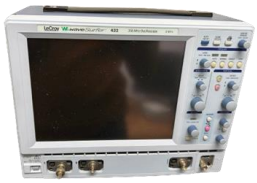
LeCroy digital oscilloscope
(Model = WaveSurfer 432)</td>
<td rowspan="2"> 
Cometech tensile testing machine (Model = QC-506)</td>
<td rowspan="2"> 
Vibra-Cell Ultrasonic Processor 500 watt
(Model = VC 505)</td>
</tr>
<tr>
<td> 
Chameleon®3 Monochrome Camera (Model = CM3-U3-31S4M-CS)</td>
</tr>
</table>

 Ultrasonic transducer setup (Model = CV334)	 Keithley 2000 Multimeter	 Thorlabs fiber collimator (Model = F810SMA-543)

Table 3.1: Exhibits the pictures with model information of a few main components utilized in the construction of setups mentioned below.

The commercially available phosphors materials $CaAl_2O_4:Eu^{2+},Dy^{3+},La^{3+}$, $SrAl_2O_4:Eu^{2+},Dy^{3+}$ and $Sr_{0.95}Ca_{0.05}(SO_4):Mn$ phosphors are used to scrutinize the functioning of ML setups. These phosphors have been bought from Foshan Juliang Photoluminescent Pigment Co., ltd and Guangzhou Shuirun chemical companies. In Figures 3.1(a) and 3.1(b), the excitation and emission spectra (excited at 270 nm) of all three shortlisted materials are presented, respectively. Figure 3.1(b) shows that the peak values of shortlisted phosphors lie at 444 nm, 530 nm and 630 nm belonging to blue, green and red color regions respectively. Among all of them, red powder has low PL intensity. Furthermore, we also measured the TL intensity as a function of temperature for all three materials individually after UV excitation at 270 nm wavelength and shown in Figure 3.1(c). TL glow curves suggested these samples have various traps with different concentrations in each sample. In Figure 3.1(d), the color images of the films containing samples in powder form, after UV excitation of 270 nm are presented. These films are prepared by the method that will be discussed in Chapter 3.

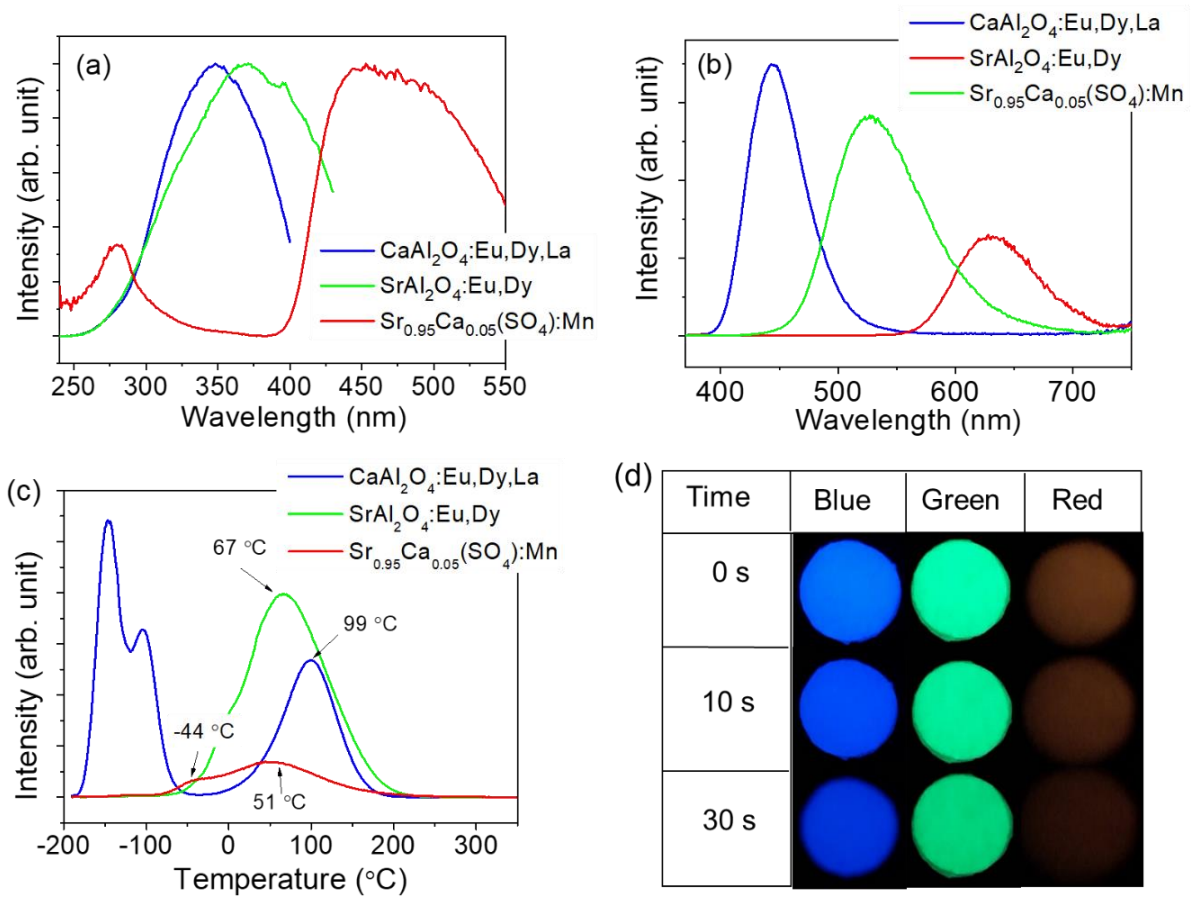

Figure 3.1: (a) PL excitation spectra, (b) PL emission spectra, and (c) TL glow curves for $CaAl_2O_4:Eu^{2+},Dy^{3+},La^{3+}$, $SrAl_2O_4:Eu^{2+},Dy^{3+}$ and $Sr_{0.95}Ca_{0.05}(SO_4):Mn$ phosphor materials, excited at 270 nm. (d) photographs of the films prepared with polypropylene tape $CaAl_2O_4:Eu^{2+},Dy^{3+},La^{3+}$, $SrAl_2O_4:Eu^{2+},Dy^{3+}$ and $Sr_{0.95}Ca_{0.05}(SO_4):Mn$ after excitation of 270 nm.

3.1. Impact-induced ML technique:

The first novel experimental setup is designed for the purpose of impact induced ML studies. In this setup, an airsoft electric gun, speedometers, sample holder, collimator followed by optical fiber, photomultiplier, and digital oscilloscope are employed (refer to Figure 3.1.1). For measuring the I-ML properties of the material, a spherical projectile having a 6 mm diameter with a known mass is fired toward the material film from a 20 cm (changeable) distance, resulting in a sudden emission of photons, which are detected by the photomultiplier via a collimator and an optical fiber. Simultaneously, an electrical signal is generated by a photomultiplier, visualized on an oscilloscope. The intensity and duration of the resulting electrical signal are correlated with the intensity of emitted photons in the consequences of de-trapping of trapped charge carriers by impact mechanical energy. Later, this data is analyzed by MATLAB code. The old technique of using a ball dropped from a height has certain drawbacks, such as multiple uncontrolled collisions, the need for large vertical space for gaining appropriate kinetic energy, etc. Moreover, achieving controlled multiple collisions with consistent impact energies and variable frequencies is not feasible with that method. However, the innovative approach of using an airsoft gun in our

designed setup proves highly effective and overcomes all these limitations. Additionally, we used a rotatable sample holder, which rotates at various incident angles with the direction of the bullet to make the setups more versatile (see Fig. 3.1.1 (b)). This technique is suitable for altering the impact kinetic energy. The incident angles can be changed from 0˚ to at least 40˚or even larger, so the deposited energy (energy transfer between the bullet and sample film) can be adjusted using this approach. The value of deposited energy, ΔE, can be estimated by using the simple formula presented in equation 3.1.1.

$$\Delta E = \frac{1}{2}\left(m{v_i}^2 - m{v_f}^2\right) \tag{3.1.1}$$

Here,

- v_f is the measured velocity of the projectile after striking the target,
- v_i is the measured initial velocity of the projectile before collision,
- m mass of the shooting projectile.

We can also tune kinetic energy by altering the masses of the projectile as described in Table 3.1.1. Figure 3.1.1 (c) shows the optical picture of the whole setup for better understanding.

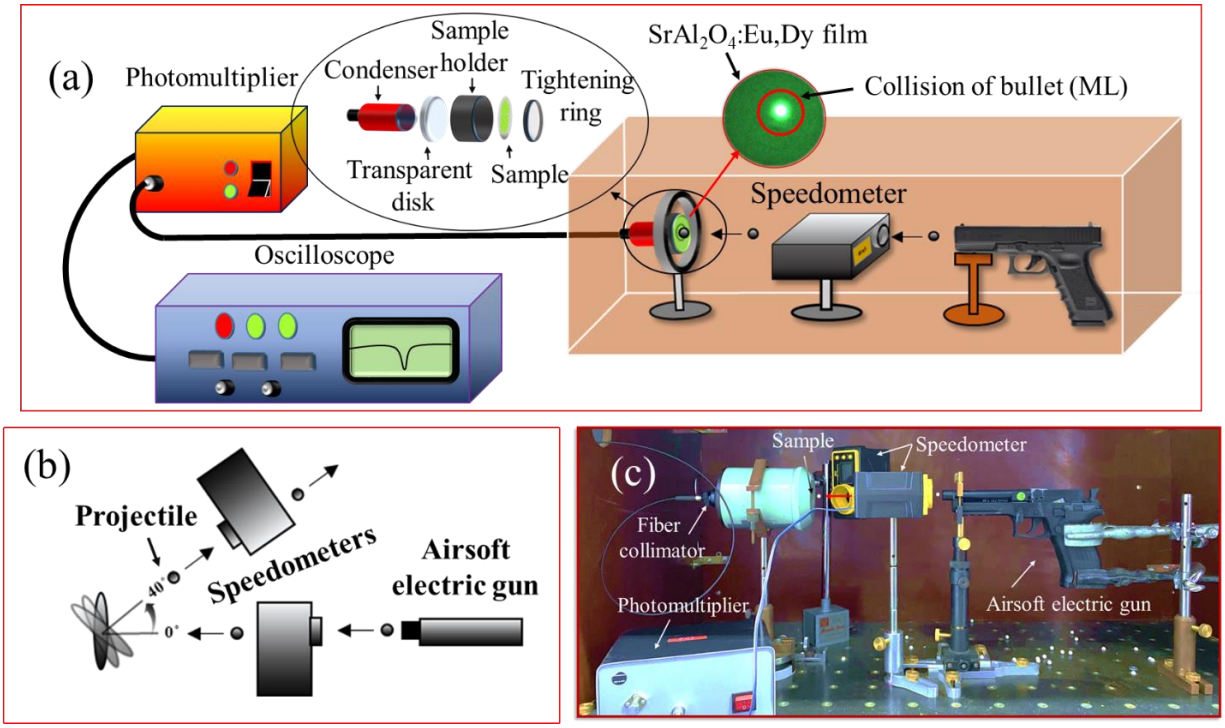

Figure 3.1.1: (a) The schematic illustration of a self-designed I-ML measurement setup, presented with a zoom portion of the same holder and I-ML from the $SrAl_2O_4$:Eu,Dy sample film. (b) Schematic diagram of the rotatable sample holder technique for variable impact kinetic energy. (c) The photograph of the I-ML setups with the labeling of each component.

S.no	Mass (g)	Speed (m/s)	Kinetic Energy (mJ)
1.	0.2	61 ± 0.2	372 ± 2.5
2.	0.23	57 ± 0.2	373 ± 2.5
3.	0.25	53 ± 0.2	351 ± 2.5
4.	0.28	45 ± 0.2	283 ± 2.5

Table 3.1.1: Dependence of initial kinetic energy and speed on the mass of projectiles fired by airsoft electric gun.

For I-ML measurements, the sample film is prepared by dispersing an appropriate amount of finely ground ML materials over the sticky surface of polypropylene tape. The edges of the tape are covered with para-film within a circular mask. Subsequently, a sandwich structure is formed by placing two similar sheets with ML powder onto each other, after removing the para-film mask. The resulting sample should exhibit flatness, evenness, homogeneity, and be relatively thin, with a surface area significantly larger than the diameter of the projectiles intended to impact it. In our experiments, we utilized 35 µm thick polypropylene adhesive tape. The radius of the circular section is around 1 cm. The surface density and layer thickness of the powder is dependent on the ML materials. A schematic diagram of the entire procedure is provided in Figure 3.1.2.

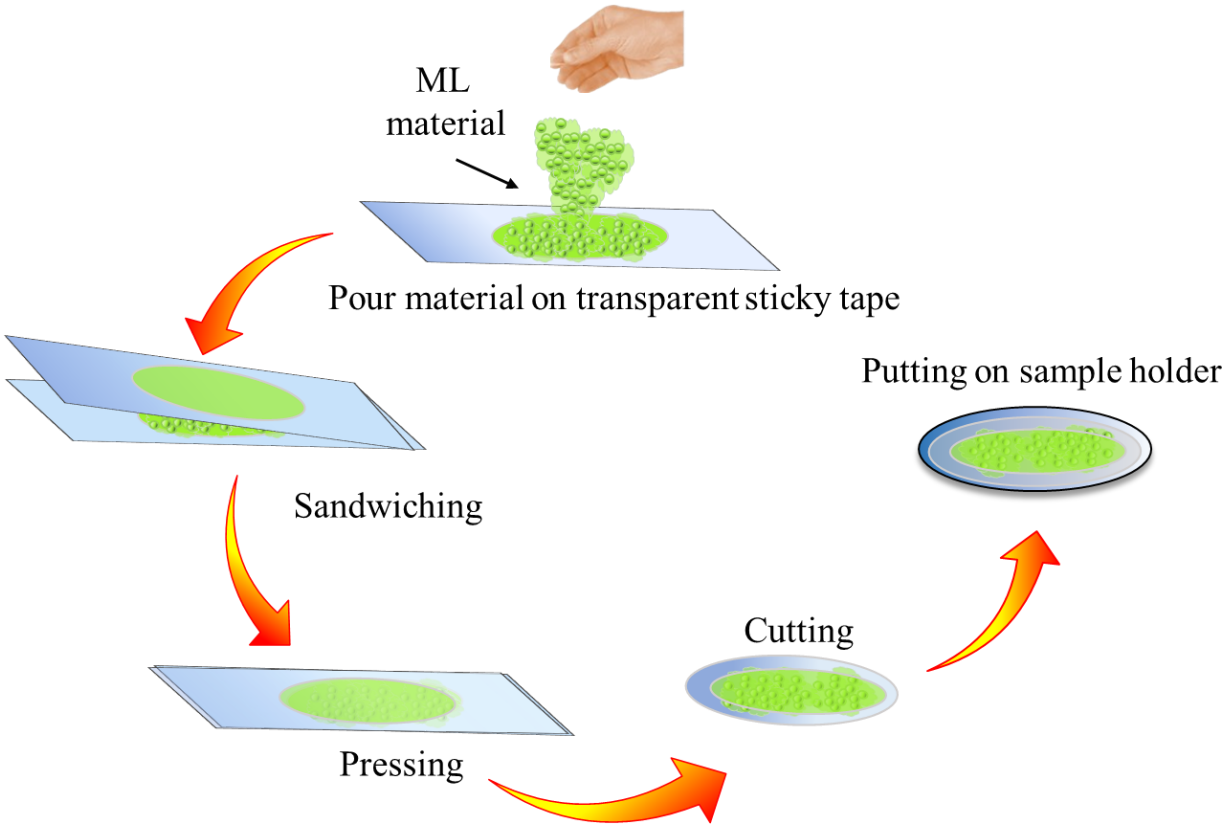

Figure 3.1.2: Steps for fabrication of ML material's thin film for I-ML measurements.

The constructed setup is tested by employing three commercially available phosphor materials (i) $CaAl_2O_4$:Eu,Dy,La, (ii) $Sr_{0.95}Ca_{0.05}(SO_4)$:Mn and (iii) $SrAl_2O_4$:Eu,Dy. The same procedure as described in Figure 3.1.2 was used for the preparation of the films containing phosphor. The photographs showing the PersL of prepared films are presented in Figure 3.1.3(a)

exhibiting the homogenous distribution of phosphor over the surface of the sticky tape. Moreover, the polypropylene tape's UV transparency is experimentally validated by the transmission spectrum presented in Figure 3.1.3(b). In Figure 3.1.3(c), the PL, PersL and ML spectra of the phosphors are demonstrated. $Sr_{0.95}Ca_{0.05}(SO_4)$:Mn and $SrAl_2O_4$:Eu,Dy exhibit broadband luminescence, ranging from 450 nm to 650 nm with a maximum at 523 nm and from 550 nm to 750 nm with a maximum at 630 nm, respectively. For both phosphors, the PersL and ML spectra have identical shapes and positions as their PL spectra, validating that Eu ions in the case of $SrAl_2O_4$:Eu,Dy, and Mn ions in the case of $Sr_{0.95}Ca_{0.05}(SO_4)$:Mn are the only centers for radiative deactivation of energy stored in the trapping states.

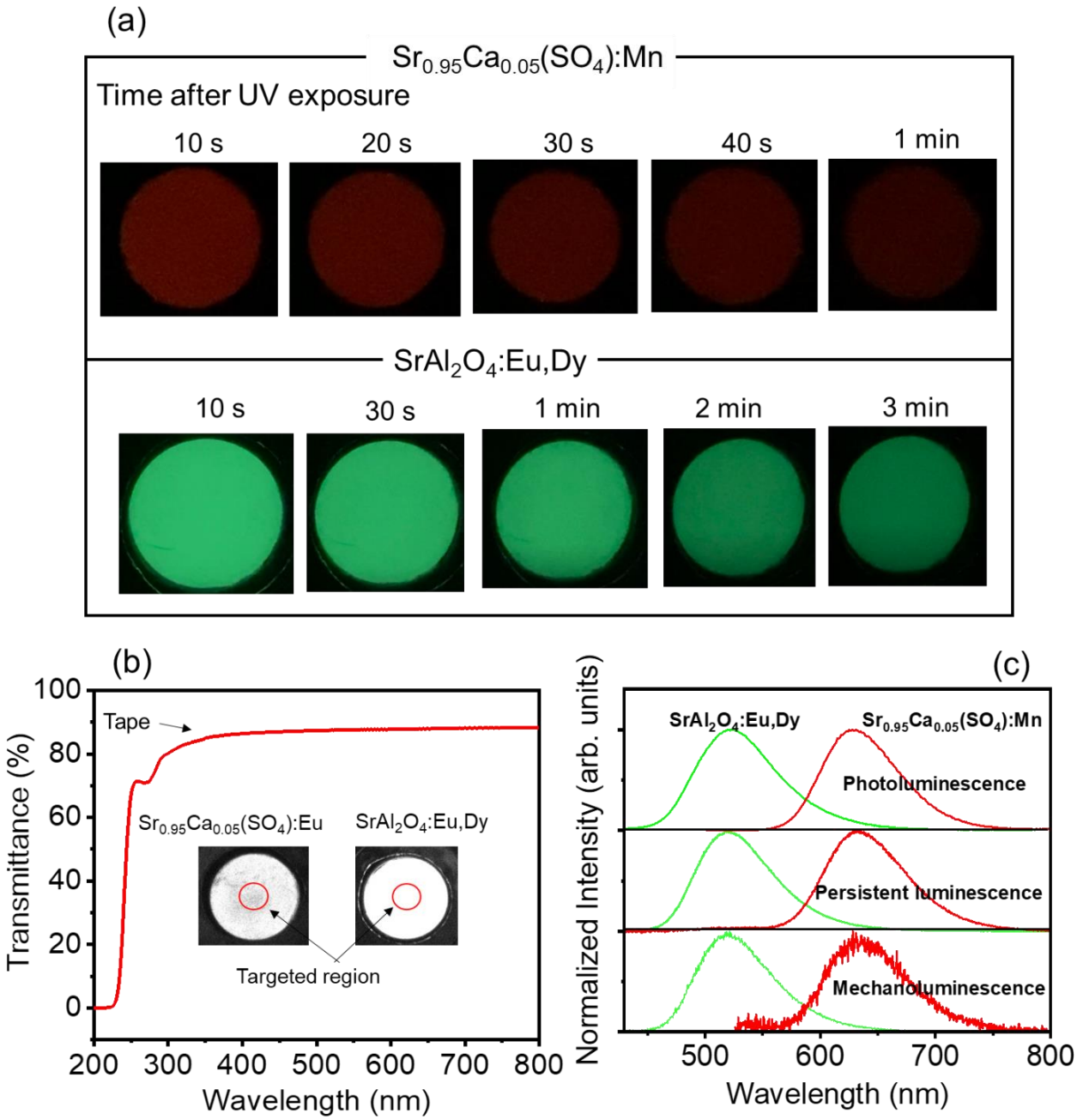

Figure 3.1.3: (a) Photographs of PersL of $SrAl_2O_4$:Eu,Dy and $Sr_{0.95}Ca_{0.05}(SO_4)$:Mn powder films after 1 min UV excitation confirms the homogenous distribution of phosphor over the entire surface of the films. (b) Transmission spectra of polypropylene adhesive tape with inset

pictures of $Sr_{0.95}Ca_{0.05}(SO_4)$:Mn and $SrAl_2O_4$:Eu,Dy films pointed with region of collision. (c) PL, PersL and ML spectra $Sr_{0.95}Ca_{0.05}(SO_4)$:Mn and $SrAl_2O_4$:Eu,Dy samples.

3.1.1. Measurement of ML with non-ML material composites:

Figure 3.1.1.1 illustrates the experimental results of I-ML measurements of composites of ML materials ($Sr_{0.95}Ca_{0.05}(SO_4)$:Mn and $SrAl_2O_4$:Eu,Dy) with non-ML Al_2O_3, obtained from the above mentioned I-ML setup. The primary reason for preparing these composites with reduced concentrations of ML powder with non-ML Al_2O_3 is that as the ML powder concentration decreases, the ML intensity is expected to decrease linearly. This approach provides a highly effective and straightforward method for evaluating the performance of the designed setup. The composite films are irradiated with a UV photodiode (270 nm) for 1 min before shooting a projectile. I-ML are measured after 30 sec waiting in case of $Sr_{0.95}Ca_{0.05}(SO_4)$:Mn and 1 min for $SrAl_2O_4$:Eu,Dy. The initial velocity of the bullet (with a radius of 3 mm and mass of 0.28 g) is 45 m/s and remains constant to a good approximation until the moment of impact with the sample film. With the dilution of ML powder with Al_2O_3, it is expected that in the area impacted by the projectile, the ML will decrease. This pattern should be clearly observable as the concentration of non-ML (Al_2O_3) in ML materials ($Sr_{0.95}Ca_{0.05}(SO_4)$:Mn and $SrAl_2O_4$:Eu,Dy) is enhanced, the measured I-ML is reduced linearly (see Figure 3.1.1.1(a) and 3.1.1.1(b)). The peak I-ML and the total I-ML intensity (calculated as ML signal intensity integrated over time) are also plotted as a function of Al_2O_3 amount in ML material in Figure 3.1.1.1 (c) and Figure 3.1.1.1(d). A linear relation between peak ML intensity and mixing concentration of Al_2O_3 is observed for both $Sr_{0.95}Ca_{0.05}(SO_4)$:Mn and $SrAl_2O_4$:Eu,Dy compounds with correlation coefficients R^2 larger than 0.95 (refer to Figure 3.1.1.1(c)). Moreover, a linear relationship of the total ML intensity with the amount of non-ML (Al_2O_3) is also observed in the graph presented in Figure. 3.1.1.1(d). It can be observed that both samples exhibit different slopes, which occurs due to their different ML intensity values ($Sr_{0.95}Ca_{0.05}(SO_4)$:Mn have low ML intensity cause low slope). The extracted outcomes of performed measurements for both materials validate the I-ML setup's accurate functioning and reliability with significant sensitivity.

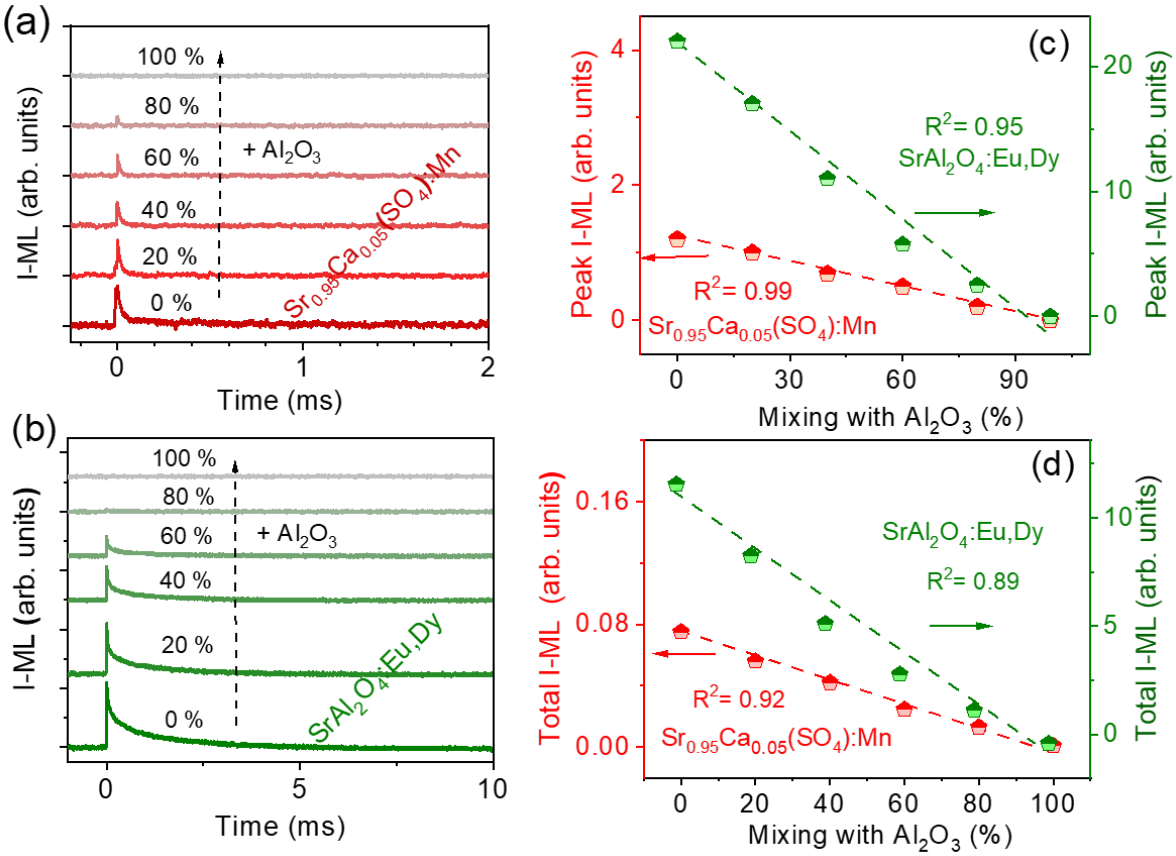

Figure 3.1.1.1: I-ML signal vs. time at different mixing percentages for (a) $Sr_{0.95}Ca_{0.05}(SO_4)$:Mn and (b) $SrAl_2O_4$:Eu,Dy. (c) peak ML intensity and (d) total ML intensity as a function of mixing amount of Al_2O_3 in ML materials.

3.1.2. I-ML reproducibility testing:

The time-dependent I-ML after UV irradiation can be also studied using the designed I-ML setup for measuring the ML retentivity of the material. Figure 3.1.2.1(a) and (b) reveals the results of I-ML at 2, 4, 5, 10, and 60 min after UV exposure of the $CaAl_2O_4$:Eu,Dy,La, and $SrAl_2O_4$:Eu,Dy samples, respectively. Figure 3.1.2.1(b) shows the I-ML at 30 s and 1 min after UV exposure for sample $Sr_{0.95}Ca_{0.05}(SO_4)$:Mn. The $CaAl_2O_4$:Eu,Dy,La and $SrAl_2O_4$:Eu,Dy have excellent ML intensity with good ML recoverability even after one hour of UV exposure. While $Sr_{0.95}Ca_{0.05}(SO_4)$:Mn powder has less ML intensity without ML recoverability exhibits. For better understanding, the peak and total I-ML of $SrAl_2O_4$:Eu,Dy are plotted as a function of time after UV excitation in Figure 3.1.2.1(d). It can be observed that at 2 min, the I-ML shows prominent peak ML intensity and total ML intensity. However, after an hour, the I-ML becomes too weak. The color visuals during projectile shooting upon film as a function of time are also displayed in Figure 3.1.2.1(e). The results demonstrate that $CaAl_2O_4$:Eu,Dy,La and $SrAl_2O_4$:Eu,Dy can retain the I-ML properties for a long time after UV excitation. Conversely, $Sr_{0.95}Ca_{0.05}(SO_4)$:Mn reveals much shorter ML retentivity.

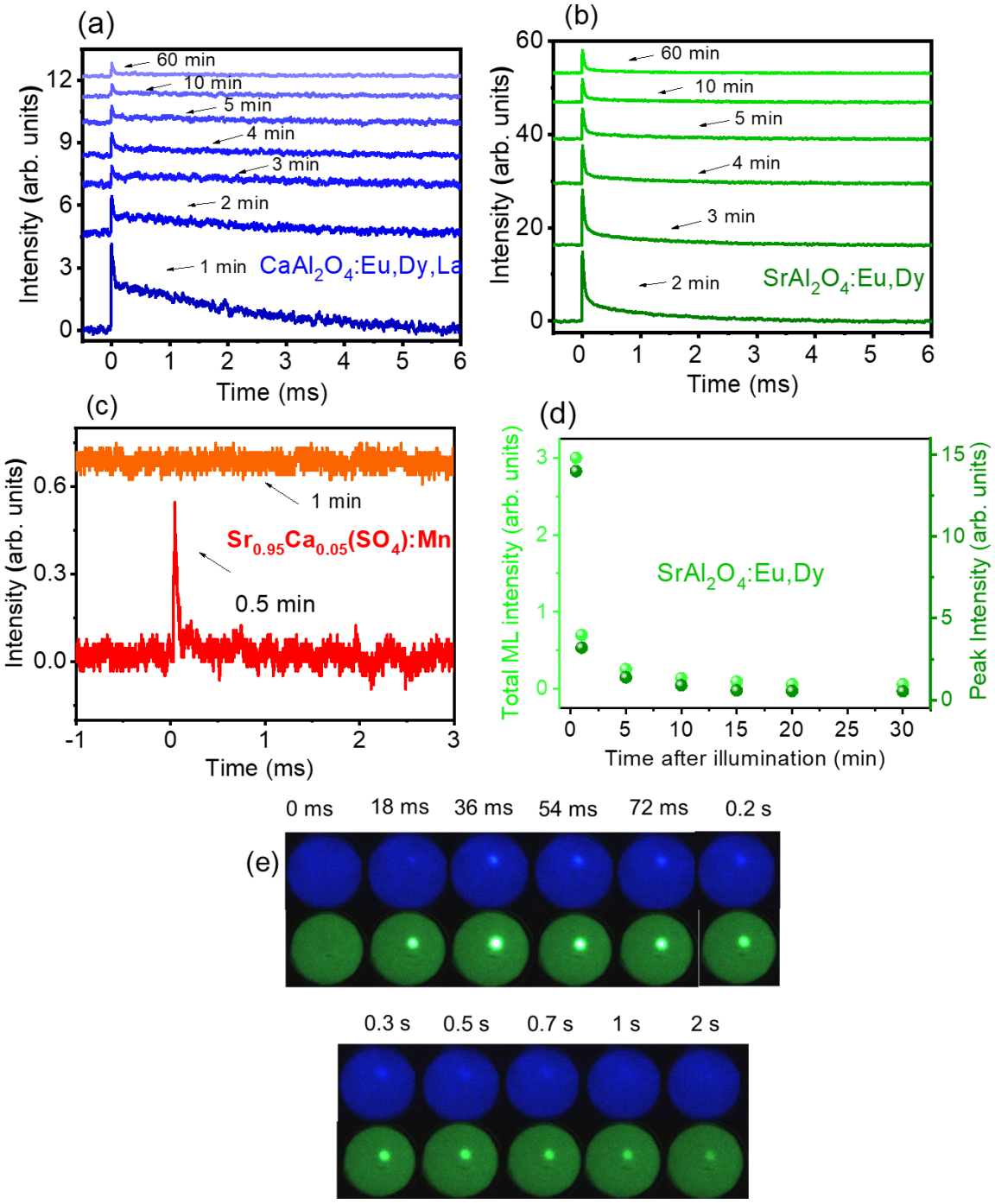

Figure 3.1.2.1: I-ML Intensity vs. time for (a) $CaAl_2O_4$:Eu,Dy,La. (b) $SrAl_2O_4$:Eu,Dy and (c) $Sr_{0.95}Ca_{0.05}(SO_4)$:Mn at different time after UV illumination, (d) total ML intensity and peak ML intensity as a function of time after illumination for $SrAl_2O_4$:Eu,Dy. (e) color images with time during I-ML measurement for $CaAl_2O_4:Eu^{2+},Dy^{3+},La^{3+}$ and $SrAl_2O_4:Eu^{2+},Dy^{3+}$ materials.

3.1.3. I-ML signal by tuning incident angle:

A unique modification is employed by using the rotatable sample holder adjustable at different incident angles from 0° to 40°, beneficial for deposited energy-dependent I-ML study. During these measurements, the initial kinetic of the projectile are kept constant by using identical mass bullets. The transfer of kinetic energy from the bullet to the film is maximum at 0° angle,

however this energy transfer is gradually reduced by increasing the incident angle up to 40̊. As mentioned in the setup description, impact kinetic energy transfer of the bullet represent deposited energy onto the ML material film. I-ML of $Sr_{0.95}Ca_{0.05}(SO_4)$:Mn and $SrAl_2O_4$:Eu,Dy at different deposited energies from 205 mJ to 269 mJ are measured at incidence angles from 40̊ to 0̊ presented in Figure 3.1.3.1. Figures 3.1.3.1(a) and 3.1.3.1(b) reveal the total and peak I-ML of $Sr_{0.95}Ca_{0.05}(SO_4)$:Mn increases exponentially as the deposited energy increases from 205 to 269 mJ. Similar outcomes are observed for $SrAl_2O_4$:Eu,Dy, validated by Figures 3.1.3.1(c) and 3.1.3.1(d). The observed results validate that the de-trapping of the electrons from deep traps correlates with the deposited energies. A large increase in I-ML is observed for the perpendicular shooting of the projectile to the target (0^0), for which the deposited energy is high. Maybe heating of the target due to the impact is also the cause of this increase of I-ML response of the material. As observed for both examined phosphors, the deposited energy is the largest for shooting perpendicular to the target with the phosphor ($\alpha = 0$), and it is almost equal to energy of the incident projectile (99% of incident energy). If the shooting angle is increased, the deposited energy decreases. The deposited energy is related to the change of the velocity perpendicular to the target, it should be proportional to the $\cos^2(\alpha)$ (if the incident speed practically the same for different shots). The plot of the deposited energy as a function of $\cos^2(\alpha)$ is presented in Figure 3.1.3.1(e). These outcomes confirmed that the proposed setup is highly functional and reliable for the study of energy-dependent I-ML experiments.

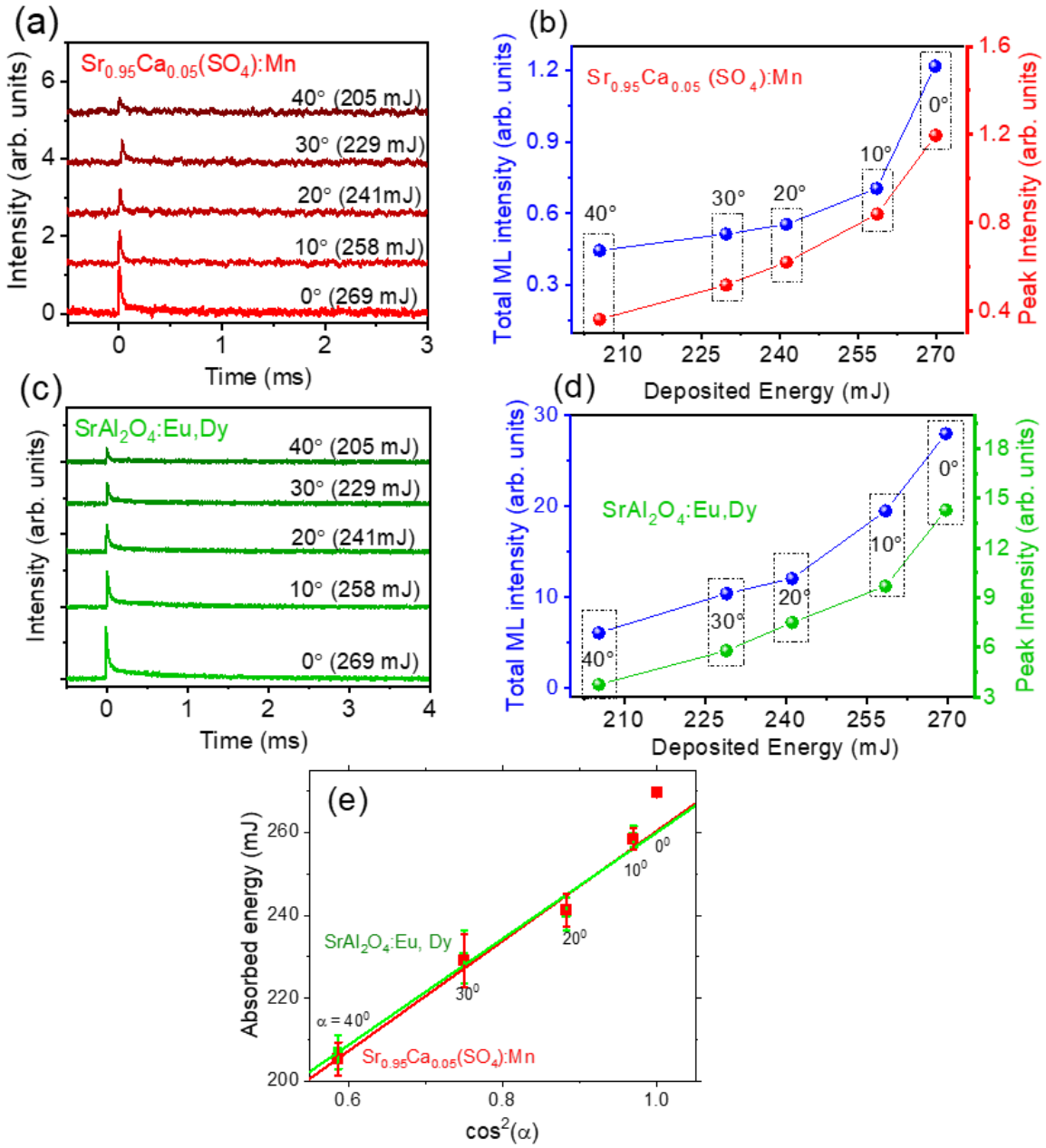

Figure 3.1.3.1: I-ML signal vs. time at various energy transfer or angle of shooting for (a) $Sr_{0.95}Ca_{0.05}(SO_4)$:Mn and (c) $SrAl_2O_4$:Eu,Dy, total and peak I-ML intensity as a function of deposited energy for (b) $Sr_{0.95}Ca_{0.05}(SO_4)$:Mn and (d) $SrAl_2O_4$:Eu,Dy, (e) The dependences of absorbed energy by the target as a function of $cos^2(\alpha)$ (α - angle of incidence) for both examined phosphors. The deposited energy was calculated as an average for five shots.

3.1.4. I-ML measurements for multiple shots:

One of the significant advantages of the proposed setup over the previously constructed "drop tower" setup is the ability to measure I-ML for a series of shots (refer to Chapter 2). The frequency of shooting projectiles can be controlled. Figure 3.1.4.1 illustrates the comparison of I-ML and PersL at several frequencies of shooting projectiles for the $SrAl_2O_4$:Eu,Dy material. At 0.06 Hz (shooting with a 15 s gap), the ML curve follows a similar pattern as the PersL. It's suggested that ML at this frequency is caused only by shallow traps. However, at higher

frequencies such as 0.1 Hz (shooting with a 10 s gap) and 0.2 Hz (shooting with a 5 s interval), the I-ML curves diverge from the PersL curve. This divergence hints that deep traps are also taking part in ML at higher shooting frequencies. Upon ceasing shooting, curves with I-ML attempt to follow the same pattern as the PersL curve, as seen in Figures 3.1.4.1(b) and 3.1.4.1(c). These types of measurements are highly beneficial for investigating the shallow trap states (responsible for PersL + ML) and deep trap states (responsible for ML) of the testing material. For the $SrAl_2O_4$:Eu,Dy material, it appears that de-trapping of carriers from deep trap states also occurs during the ML process at higher shooting rate.

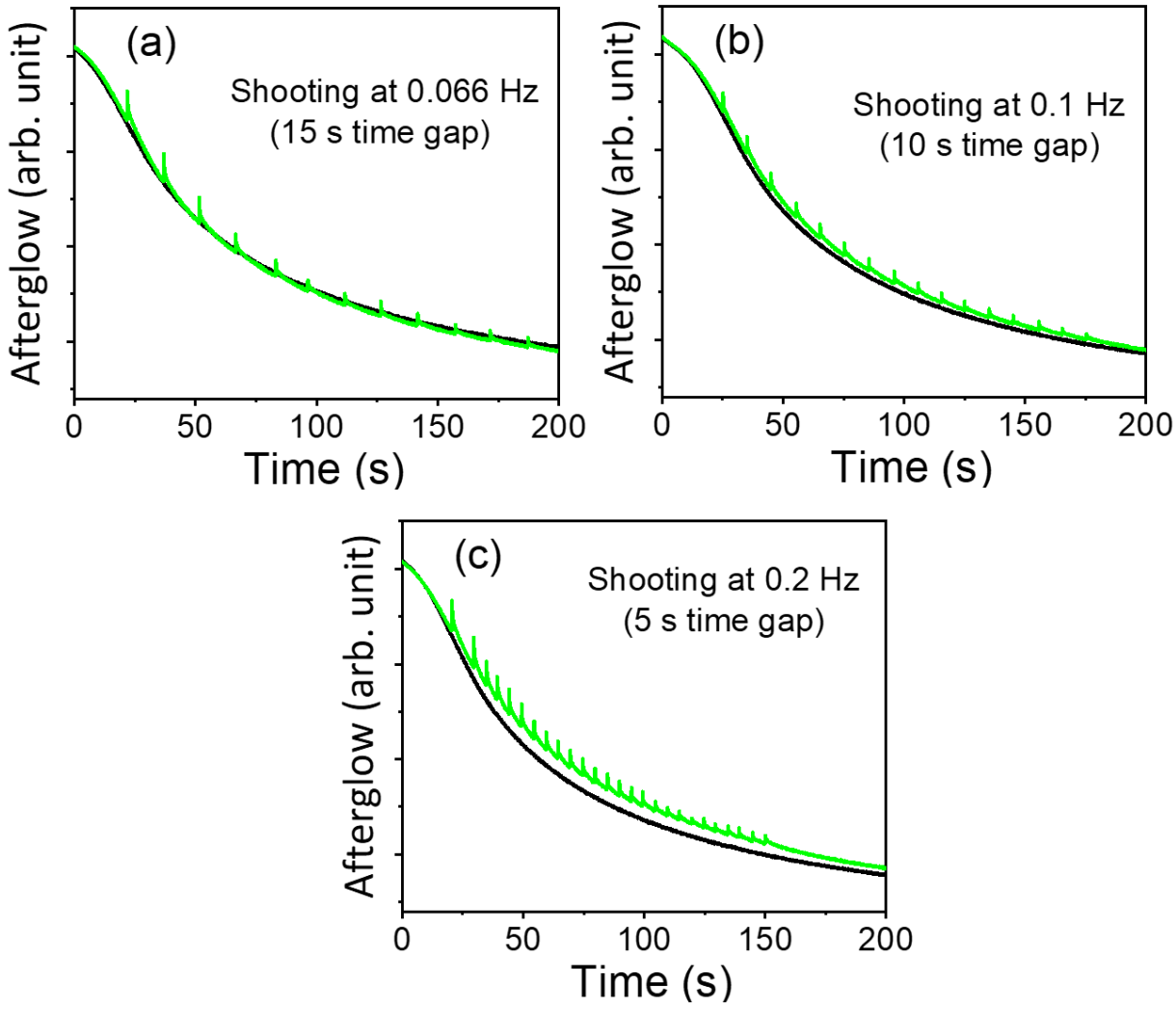

Figure 3.1.4.1: PersL intensity (black line) and PersL with I-ML signal for series of shot (green line) vs. time at (a) 0.066 Hz, (b) 0.1 Hz and (c) 0.2 Hz frequencies.

3.2. Stress induced ML technique:

The second setup is designed for measuring stress-induced ML properties of materials. This setup worked on the principle of previously published ideas of measuring ML properties with some modifications [13, 122]. In the presented design, a tensile testing machine is used for applying stress upon the cylindrical (or any other form or shape) composite pellet made up of ML

material and stress transmission medium, simultaneously ML was captured using a high-frame-rate and high-resolution (2048 x 1536) monochromatic camera (Chameleon®3 Model: CM3-U3-31S4M-CS) in the form of optical visuals. Afterward, the series of these extracted images are utilized for the investigation of stress-sensing ML properties of the material with the help of self-designed LabVIEW codes and Origin software. In this setup, we can study the stress distribution within a tested pellet by measuring ML at different force's application speeds (from 0 mm/min to 800 mm/min) and various deformation. The deformation in the structure is studied by observing the changes in dimension parameters measured by a tensile testing machine. Figure 3.2.1 (a) shows the schematic illustration and the photographs of the S-ML setup, exhibiting the construction and functioning of the setup, respectively.

For S-ML experiments, we selected optical epoxy (EPO-TEK® 305) for composite preparation, due to its high shore A hardness, which is beneficial for transferring stress from the medium to the ML material. Additionally, it offers reasonable optical transmission, with approximately 67% transmission in the UV (260 nm) region and approximately 95% transmission in the visible and IR regions. Both UV and visible transmission are important for the excitation of the material and the measurement of ML, respectively. Typically, we prepared cylindrical pellets of epoxy with a composition ratio of 9:1 with the ML material. These pellets have a thickness of 10 mm and a diameter of 22 mm. To examine the functioning and measurements reliability of the constructed setup, $SrAl_2O_4$:Eu,Dy phosphors material is utilized for preparation of the cylindrical composite pellet using optical epoxy (EPO-TEK® 305) with a mass ratio 1:5 ($SrAl_2O_4$:Eu,Dy/epoxy), respectively.

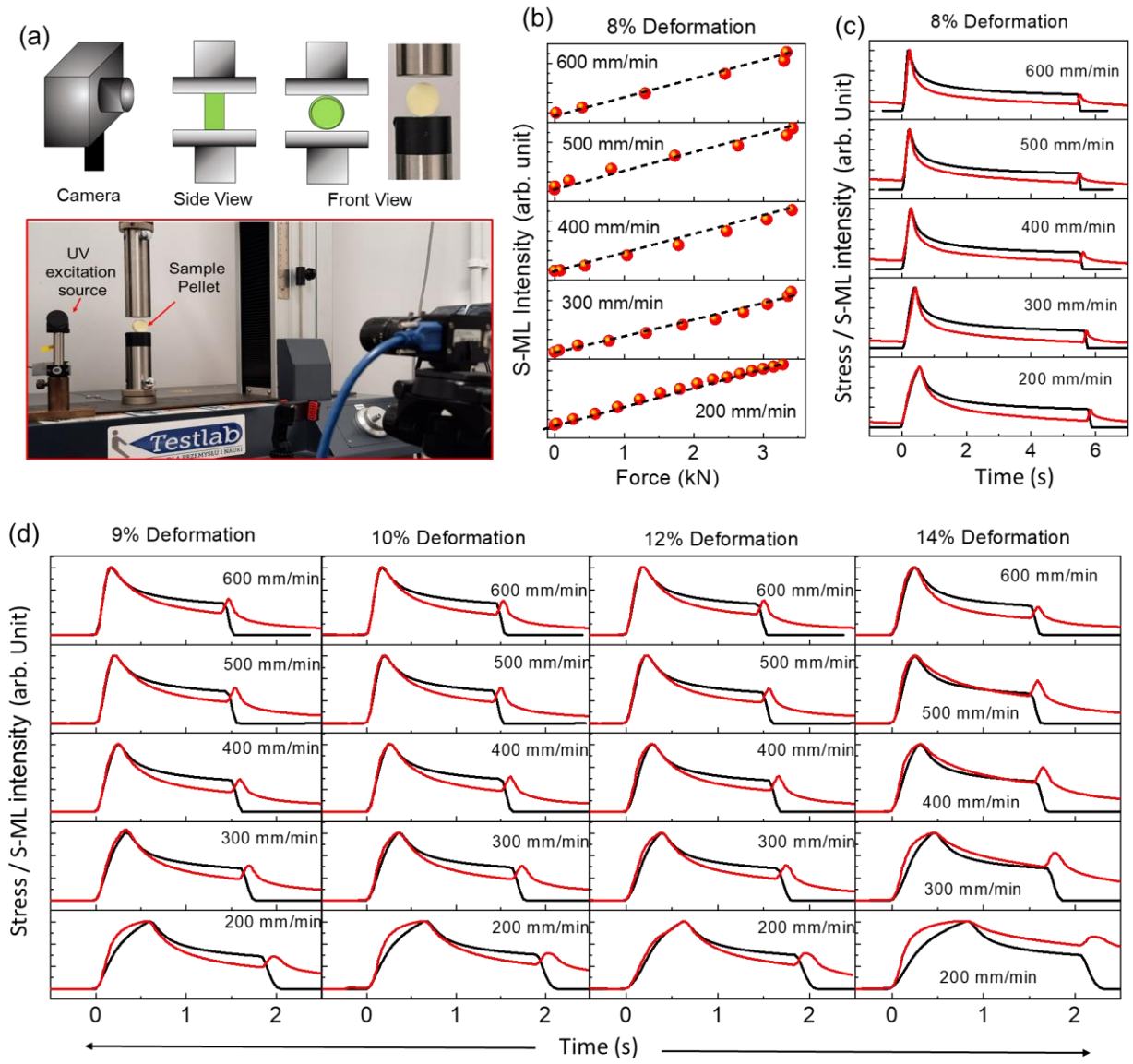

Figure 3.2.1. (a) Schematic diagram and photograph of the S-ML setup with the labeling of each object existing in the setup. (b) S-ML intensity as a function of applied force at various speeds from 200 to 600 mm/min up to 8% maximum deformation. (c) Overlapped curves of applied force magnitude (black curve) and S-ML Intensity (red curve) vs. time at variable stress application speeds from 200 to 600 mm/min up to 8% maximum deformation with a 5 s delay between applying and releasing of stress for $SrAl_2O_4$:Eu,Dy/epoxy pellet. (d) Overlapped curves of applied force magnitude and S-ML intensity as a function of time at variable stress application speeds from 200 to 600 mm/min up to 9%, 10%, 12% and 14% maximum deformation values with a 1 s delay between applying and releasing of stress for $SrAl_2O_4$:Eu,Dy/epoxy pellet.

For evaluating the functioning of the S-ML setup, the S-ML measurements of $SrAl_2O_4$:Eu,Dy/epoxy pellet are performed under various experimental conditions and presented in Figures 3.2.1(b-d). Figure 3.2.1(b) shows the linear relationship between applied force (black curve) and the measured S-ML intensity (red curve) at different application rates up to 8% deformation. Similarly, in another measurement, S-ML intensity signal of $SrAl_2O_4$:Eu,Dy

demonstrates perfect alignment with the applied force magnitude, validating its significant ability to sense and measure applied mechanical stress. Figure 3.2.1(c) illustrates a good correlation between the force magnitude values received from the tensile testing machine and the S-ML intensity emitted by $SrAl_2O_4$:Eu,Dy/epoxy pellet at different force application speeds ranging from 200 mm/min to 600 mm/min, up to 8% maximum deformation. Moreover, an abrupt change in S-ML intensity is observable upon stress release even after a 5 s long delay, indicating the ability to sense stress release. S-ML of $SrAl_2O_4$:Eu,Dy/epoxy pellet are also observed at 9%, 10%, 12% and 14% maximum deformations, as presented in Figure 3.2.1(d). It can be found that at large maximum deformations and low speeds, the S-ML curves of $SrAl_2O_4$:Eu,Dy/epoxy pellet deviate from the force magnitude curves. This may have occurred because the applied force was too large, likely causing most of the charges to be detrapped before reaching that maximum force. Additionally, at low speeds, the change in the piezoelectric field is weak. Moreover, the time evolution of the applied load transferred to the ML powder grains embedded in polymer cylinder and the time evolution of the ML response differ. It can be observed that the $SrAl_2O_4$:Eu,Dy/epoxy pellet exhibits ML during both mechanical actions, i.e., the application and release of stress. During the release of stress, the epoxy pellet stretches, exerting a mechanical effect on the ML powder, causing the emission of ML light. Figure 3.2.2 displays another experimental demonstration of the S-ML by the same composite epoxy pellet containing $SrAl_2O_4$:Eu,Dy phosphors under mechanical stress, visualized in optical images form. The photographs of a cylindrical pellet during the application of stress at a constant rate (200 mm/min) until reaching 9% deformation reveal the invisible stress spreading within the structure by visible green color S-ML. These outcomes elucidate the concept of S-ML measurements under different conditions and underscore the significance of the setup for the study of S-ML properties of materials.

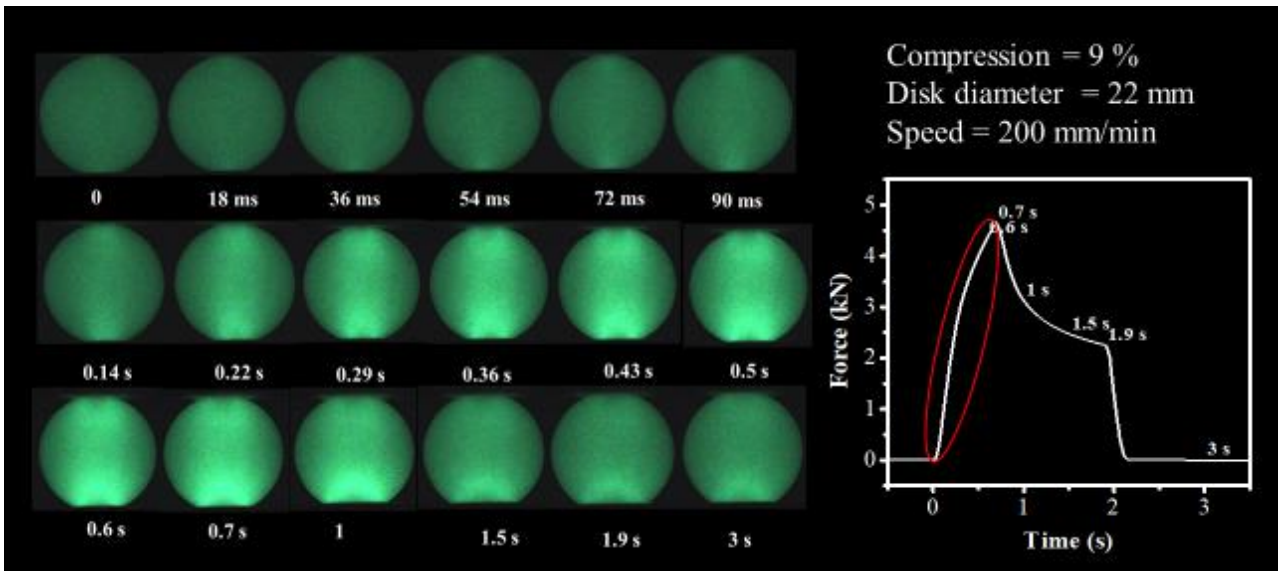

Figure 3.2.2: The ML visuals of $SrAl_2O_4$:Eu,Dy/Epoxy pellet during deformation by applying mechanical force.

3.3. Ultrasound-induced Luminescence technique:

A setup for ultrasound-induced luminescence operating at a frequency of 20 kHz was designed, consisting of an ultrasound transducer (model: CV334, vibracellTM, SONICS), a

photomultiplier (model: H10720P-04), and a 3-D printed plastic stage to hold the sample with an optical collimator underneath (see Figure 3.3.1 (d)). The Us transducer, with a diameter of 13 mm, was utilized, featuring a maximum vibrating amplitude of 120 µm (100%), adjustable between 24 µm and 120 µm. The experimental procedure involved placing a plexiglass sheet with the sample film covered by an Us-gel layer over the 3-D printed plastic stage. An optical collimator was fixed beneath the stage to capture Us-L. Subsequently, the vibrating transducer was positioned perpendicular to the center of the film, aligning the vibrating transducer, film center, and collimation in a vertical axis to ensure sufficient light capture during sonication, which was then transferred to the photomultiplier. The distance between the transducer and sample can be adjustable, while the distance between the sample and collimator was 4 mm. Once the setup was configured, the sonicator was programmed to control the Us On/Off duration and the number of cycles. Time-dependent luminescence curves were generated using a LabVIEW code connected with a Keithley 2000 multimeter that received electrical signals from the photomultiplier (refer to Figure 3.3.1 (c)). An increase in the measured intensity emitted by the sample was observed during exposure to Us waves, indicating the Us-L (see Figures 3.3.1 (a) and (b)). Upon pausing sonication, the intensity signal decreased. The decay behavior of the signal depended on the phosphor material, typically exhibiting an exponential decrease (like PersL). Figure 3.3.1 (e) represents the photograph of the top and side view of the setup. For Us-L measurements, the sample film was produced by thoroughly mixing the ML powder in a specific ratio with PDMS resin or epoxy, and then the curing agent was added. The mixture was poured into an especially dedicated container to solidify.

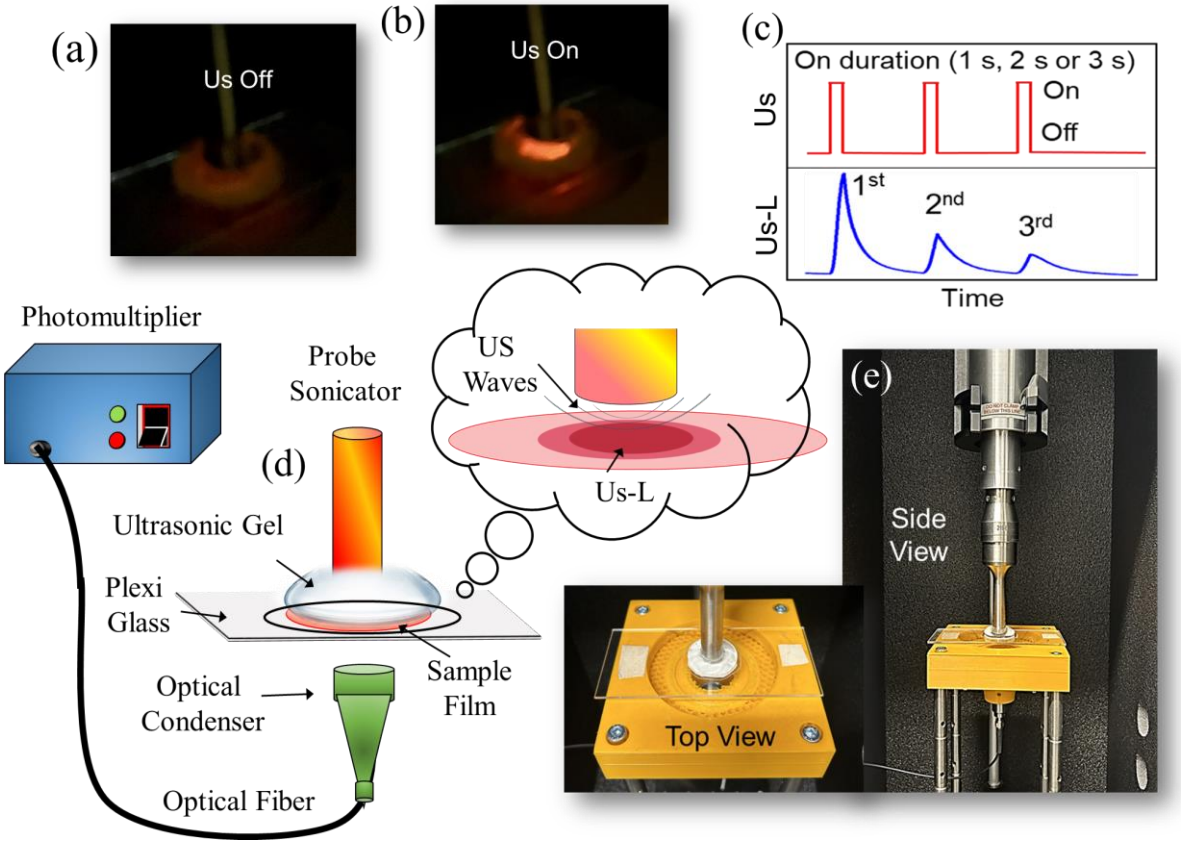

Figure 3.3.1: the photograph of the PDMS/$LiTaO_3$:Pr sample film (a) without Us exposure and (b) during Us exposure. (c) The graphical representation of the Us wave signal and the resultant

luminescence signal. (d) The schematic demonstration of the self-constructed Us-L setups worked at 20 kHz frequency. (e) The photographs of the setup from top and side views.

For the purpose of calibration and monitoring the functioning of the setup, commercially available phosphor materials ($CaAl_2O_4$:Eu,Dy,La and $SrAl_2O_4$:Eu,Dy) embedded on 1 mm epoxy (EPO-TEK® 305) film with mass ratio 1:9/phosphor:epoxy are employed. The three different types of measurements are conducted namely (i) Us pulse duration dependent (ii) Us amplitude dependent and (iii) temperature dependent Us-L measurements. The outcomes of these measurements are presented below, which confirmed the better functioning and diverse measuring capabilities of the setup.

3.3.1. Us-L Measurements at different Us pulse's duration:

In the designed setup, we can control the Us pulse on/off duration and number of cycles. Us pulse off duration is also an important parameter, it gives time to the sample to reduced it PersL. This feature allows for the evaluation of Us-L properties based on different Us pulse durations. Experimental results for various Us pulses on/off ratios in seconds (1 s/19 s, 3 s/17 s, 5 s/15 s, 7 s/13 s, and 10 s/10 s) up to five cycles for $CaAl_2O_4$:Eu,Dy,La and $SrAl_2O_4$:Eu,Dy are presented in Figures 3.3.1.1 (a) and (b). It is worth mentioning here that for example, 1 s/19 s means 1 second Us is 'on' and 19 seconds Us is 'off'. Before each measurement, the samples are consistently excited with UV radiation for a few seconds. The change in intensity of the phosphors during sonication represents the Us-L. It can be observed that both phosphors exhibit the highest Us-L at a 5 s/15 s ratio. At low Us 'on' duration (1 s/19 s and 3 s/17 s), there is insufficient energy provided to the phosphors to emit high-intensity Us-L. Conversely, at high Us 'on' duration (7 s/13 s and 10 s/10 s), the phosphors do not have enough time to reduce their PersL intensity, resulting in a smaller difference in intensity (Us-L). Thus, for the phosphor materials mentioned, a 5 s/15 s ratio is optimal for observing intense Us-L.

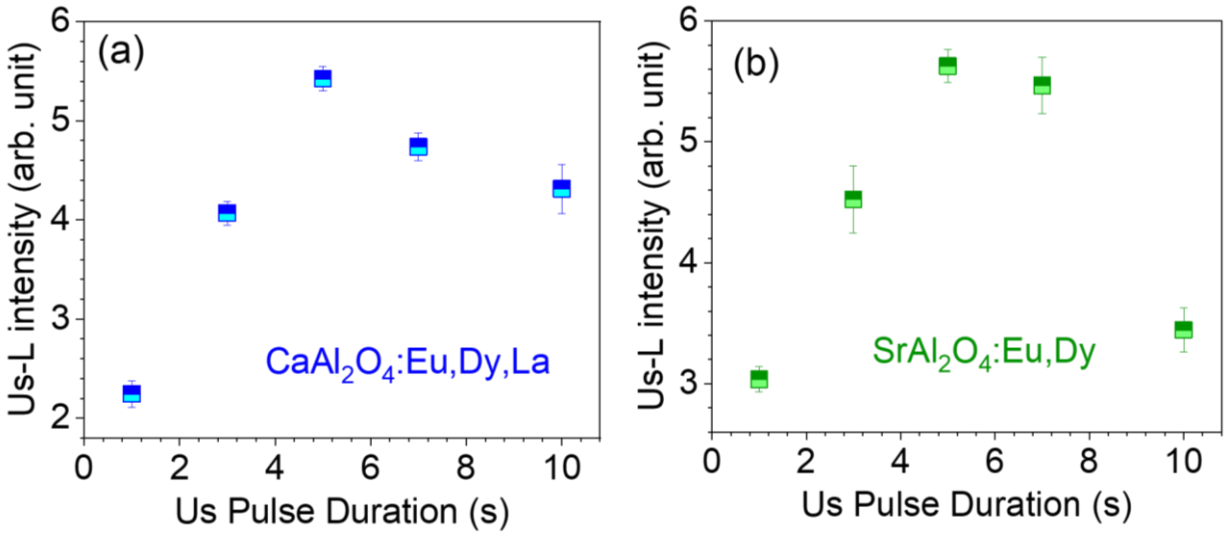

Figure 3.3.1.1: The Us-L intensity as a function of Us pulse On duration time for samples (a) $CaAl_2O_4$:Eu,Dy,La and (b) $SrAl_2O_4$:Eu,Dy at 20 kHz and 40% (48 µm) amplitude.

3.3.2 Us amplitude dependent Us-L Measurements:

Another built-in feature of the Us transducer is utilized in amplitude-dependent Us-L measurements. This feature allows control of the vibration amplitude of the Us transducer from 0 to 100% (120 µm). During the measurement at each amplitude, the sample was first excited with UV light for a short duration. After switching off the UV, the measurement was then started. Figure 3.3.2.1 (a) and (b) show the amplitude-dependent Us-L properties of $CaAl_2O_4$:Eu,Dy,La and $SrAl_2O_4$:Eu,Dy phosphors, respectively. Both phosphors exhibit a linear relationship between the emitted Us-L and the applied Us amplitude, albeit with different slopes. These measurements are beneficial for studying the dependence of Us-L on the amplitude of applied Us waves. The linear relation between the vibrational amplitude (directly related to force) of Us sonication and Us-L indicates the ML (prominent) nature of Us-L at 20 kHz.

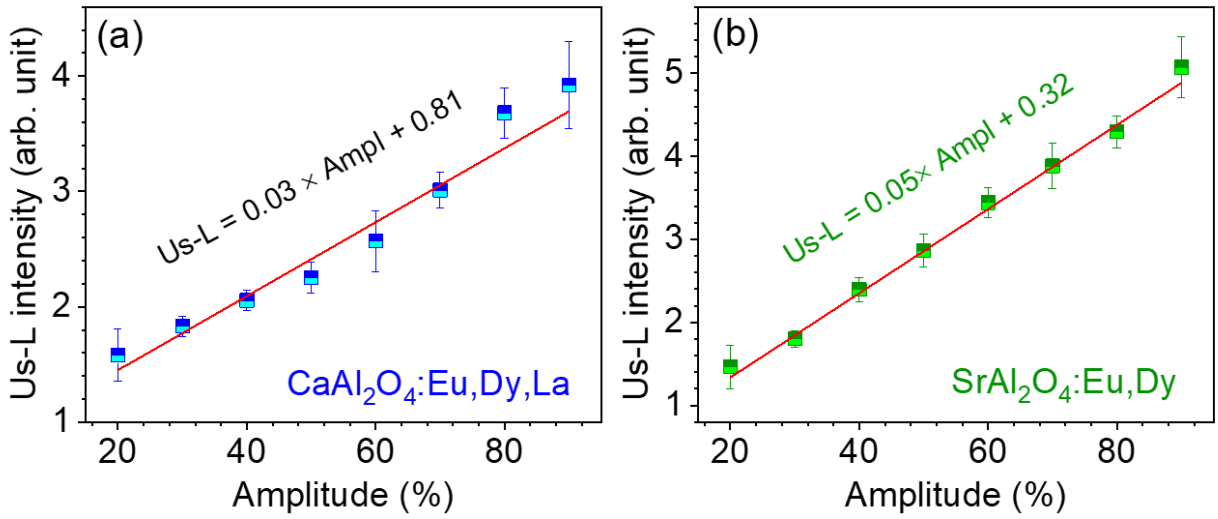

Figure 3.3.2.1. The Us-L intensity versus amplitude of applied Us waves for (a) $CaAl_2O_4$:Eu,Dy,La and (b) $SrAl_2O_4$:Eu,Dy phosphors at 20 kHz with Us On/Off ratio set at 1 s/19 s.

3.3.3. Temperature dependent Us-L Measurements:

For the temperature-dependent Us-L measurements, the sample is heated to the desired temperature in a water beaker. Immediately after removing the sample from the beaker, Us-L measurements are performed using the selected parameters. Although some change in temperature is observed during the transfer from the beaker to the measurement setup and application of Us gel, it does not significantly affect the results, as these measurements aim to estimate Us-L behavior at temperatures close to room temperature. Figures 3.3.3.1 (a) and (b) show the temperature-dependent retentivity of Us-L intensity for $CaAl_2O_4$:Eu,Dy,La and $SrAl_2O_4$:Eu,Dy phosphors, respectively. It can be observed that at lower temperatures, the overall Us-L intensity is lower while the retentivity is good. This may occur due to high-energy traps; at low temperatures, the amount of thermal energy is insufficient to effectively de-trap charge carriers. However, as the temperature increases, the charge carriers are de-trapped more readily, leading to a reduction in Us-L retentivity. Figures 3.3.3.1 (c) and (d) show the Us-L intensity as a function of temperatures for $CaAl_2O_4$:Eu,Dy,La and $SrAl_2O_4$:Eu,Dy phosphors, respectively. It is observed

that at 50°C, both samples exhibit higher Us-L intensity. This occurs due to the presence of high-energy traps, as validated by the TL measurements (see Figure 3.1(c)). At lower temperatures, Us waves are unable to remove a large number of charge carriers. Furthermore, these samples lack traps at room temperature. It appears that 50°C is the optimal temperature for Us waves to effectively release a significant number of charge carriers from the traps. The extracted results from multiple measurements of Us-L at 20 kHz validate the performance and reasonable functioning of the designed setup.

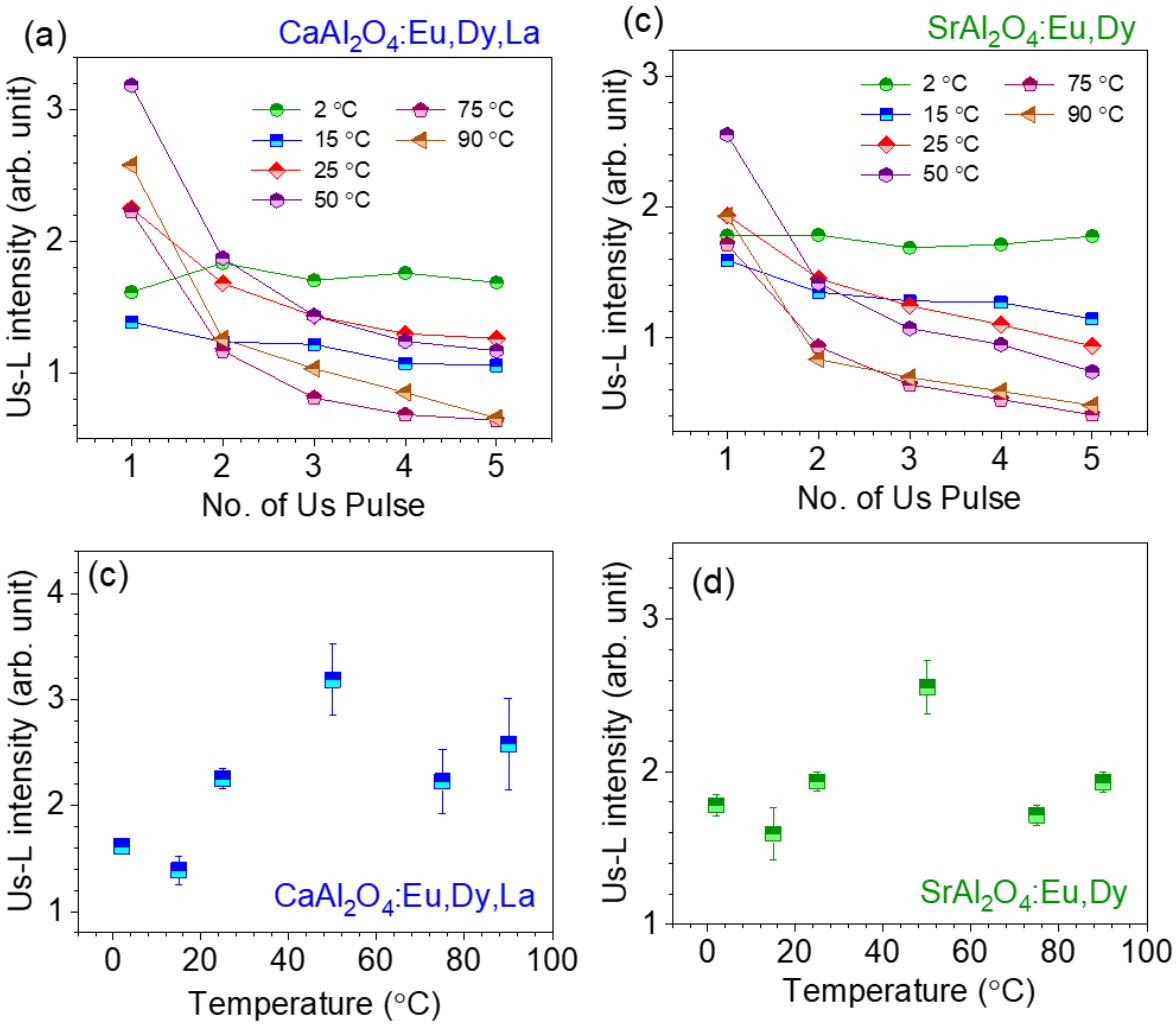

Figure 3.3.3.1. The Us-L intensity versus number of Us pulses for (a) $CaAl_2O_4$:Eu,Dy,La and (b) $SrAl_2O_4$:Eu,Dy phosphors at several pre temperatures 2°C, 15°C, 25°C, 50°C, 75°C, and 90°C. The average Us-L with error bar as a function of temperature before measurement for (c) $CaAl_2O_4$:Eu,Dy,La and (d) $SrAl_2O_4$:Eu,Dy phosphors.

CHAPTER 4. Mechanoluminescence Properties of $LiTaO_3$:Pr

As mentioned in the introduction, ML is divided into several categories, including triboluminescence, fractoluminescence, elastico-mechanoluminescence (E-ML) [10, 11], etc. Among these, E-ML is particularly significant for various industrial and medical applications due to its linear dependence on applied mechanical stress or impact. Moreover, E-ML should be reproducible without any structural damage to the material. E-ML occurs in trap-controlled materials through three main steps: (i) trapping of charge carriers in shallow and deep traps (achieved by pre-UV excitation), (ii) de-trapping of these carriers by mechanical action, and (iii) emission of light due to carriers recombination in luminescent centers. [10]. For E-ML studies and applications, a suitable piezoelectric host structure with an appropriate band gap and proper luminescent dopant elements (typically rare earth or transition metals) is essential. During exposure to high-energy photons or UV radiation, charge carriers are trapped in levels created by impurities (dopants) or structural defects. These carriers may remain trapped even after the exposure ends. The energy structure of these trap levels is a crucial factor in determining the material's ML capability. Current research focuses on the intensity, sensitivity, reproducibility, and linearity of ML intensity in response to applied mechanical stimuli. Gun Jin Yun et al. investigated the stress-sensing performance of $SrAl_2O_4$:Eu (SAOE) and $SrAl_2O_4$:Eu,Dy (SAOED) ML materials, finding that SAOED exhibited superior ML stress-sensing properties with higher sensitivity and no saturation of ML intensity under applied forces [76]. The recently discovered ML properties of rare-earth-ion-doped piezoelectric $LiTaO_3$ host materials have attracted attention for stress-sensing applications across various engineering fields [57, 65]. However, the limited literature and less comprehensive studies on doped $LiTaO_3$ hinder its commercialization. For example, $LiTaO_3$ doped with transition-metal ions such as Cr^{3+} can emit light in the far-red region, which is also of interest for ML applications [125]. This chapter focuses on a comprehensive examination of ML generated by various mechanical stimuli. Three different ML experimental setups are utilized to measure ML under various stress conditions with high sensitivity. Additionally, the correlation of ML intensity with mechanical impact energy, force, and impulse is thoroughly examined.

4.1. Synthesis process:

$LiTaO_3$ powder samples doped with Pr ions were synthesized using the high-temperature solid-state reaction method by Magdalena Baran. Analytical grade tantalum oxide Ta_2O_5 (Aldrich), lithium carbonate Li_2CO_3 (Sigma Aldrich), and praseodymium oxide Pr_2O_3 (Lehmann & Voss & Co.) served as precursor materials. The Pr^{3+} doping concentrations were fixed at 1, 3, and 5 mol % for samples S1, S2, and S3, respectively. The reagents were accurately weighed and thoroughly mixed using a planetary ball mill (Pulverisette 7, Fritsch), with ethanol as the wet grinding medium. The resulting powder was dried at 120 °C for 12 hours. The extracted semi-product was then ground in an agate mortar and sintered at 1100 °C for 12 hours in an air atmosphere. The thin film preparation for I-ML measurements was previously described in Chapter 3. For S-ML measurements, cylindrical pellets with a diameter of 22 mm and a thickness of 10 mm were prepared by thoroughly mixing the ML material ($LiTaO_3$:Pr) with epoxy in a 1:9 ratio. This viscous mixture was poured into a cylindrical Teflon die and placed in an oven at 60

°C for 1 hour to solidify. After solidification, the $LiTaO_3$:Pr/epoxy pellets were removed from the die.

4.2 Characterization techniques:

The quality and purity of the synthesized samples were examined using X-ray diffraction (XRD) and X-ray photoelectron spectroscopy (XPS). XPS measurements were performed by Dr. Anna Wolska of IP PAS. XRD measurements were conducted with a Rigaku SmartLab 3kW X-ray diffractometer, equipped with a copper lamp and a D/tex Ultra 250 solid-state detector, operating at 40 kV and 30 mA. The XRD patterns were collected with a scanning step of 0.02° at a speed of 3.03°/min. XPS spectra were recorded using a Scienta R4000 hemispherical analyzer (pass energy 200 eV) with monochromatic Al Kα (1486.7 eV) excitation (Scienta MX-650), operating at 300 W with charge neutralization. XPS data were processed with Shirley-type background subtraction and fitted with a Gaussian-Lorentzian function using CasaXPS software. PL excitation and emission, PersL, and TL measurements were performed using Horiba Fluorolog and Linkam temperature control systems. To measure PL spectra across a wide wavelength range up to 1000 nm, a Shamrock 500i spectrometer with a TEC iDus420 camera (Andor Technology) was used.

To explore the ML properties, three experimental approaches were employed: (i) Friction induced ML, (ii) Impact induced ML, and (iii) Stress induced ML. The first setup controlled by LabVIEW software was used to measure the F-ML spectrum mentioned in Chapter 2. For I-ML measurements, a self-designed I-ML measurements setup was employed, as mentioned in Chapter 3. S-ML measurements were performed with a universal tensile testing machine, which compressed the cylindrical pellet (material/epoxy) at a constant rate, causing S-ML. The description of the setup is provided in Chapter 3. For measuring ML in the IR region, a photomultiplier with a detection range from 185 nm to 870 nm was used, along with a filter that blocked ML below 650 nm, allowing only IR ML to pass through.

4.3. Results and Discussion:

4.3.1. XRD and XPS analysis:

The measured XRD patterns of the tested powders and the $LiTaO_3$ standard number PDF 04-002-5060 are shown in Figure 4.3.1.1 (a). The XRD pattern of sample S1 matches perfectly with the $LiTaO_3$ standard PDF 04-002-5060. In the case of samples S2 and S3 synthesized with higher praseodymium dopant concentrations (3% and 5%, respectively), the analysis using the whole powder pattern fitting method (WPPF) revealed the presence of small amounts of additional phases. Specifically, lithium praseodymium tantalum oxide ($Li_2Pr_{0.67}Ta_2O_7$) and praseodymium tantalum oxide ($PrTaO_4$) were found in samples S2 (5.3%) and S3 (4.5%), respectively, whereas sample S1 consisted solely of the pure $LiTaO_3$ phase. These results confirm that the Pr ions doped into the host lattice do not disrupt the crystalline trigonal structure of the R3c space group. The crystallographic parameters of the prepared samples, along with the percentages of other unintentional phases, are presented in Table 4.3.1.1. It appears that a higher Pr dopant concentration during synthesis leads to the formation of additional Pr-based phases. Consequently,

the actual dopant concentration in the $LiTaO_3$ crystal lattice for samples S2 and S3 is lower than the intended concentration used during their synthesis.

According to Wilkinson et al.'s proposed antisite defect model present in the $LiNbO_3$, lithium vacancies are the dominant inherent defects, which is also applicable to $LiTaO_3$ [126]. To balance charges in the $LiTaO_3$ crystal lattice, some Ta^{5+} ions occupy Li^+ sites, forming antisite Ta_{Li}^{4+} defects, facilitated by the similar ionic radii of Li^+ (0.64 Å) and Ta^{5+} (0.76 Å) [65]. When Pr^{3+} ions are doped into the $LiTaO_3$ matrix, additional defects are created at the octahedral Li^+ and Ta^{5+} sites, leading to the formation of trap states. During calcination, Pr^{3+} partially oxidizes to Pr^{4+}, while Ta^{5+} captures these electrons and reduces to Ta^{4+}. This Pr^{3+} to Pr^{4+} conversion results in decreased luminescence centers. Therefore, XPS measurements were conducted on the synthesized $LiTaO_3$:Pr powders to estimate the percentage distribution of Pr^{3+} and Pr^{4+} in each sample, as shown in Figure 4.3.1.1 (b-d). The binding energy range of the measured XPS spectra for the S1, S2, and S3 samples is between 920 and 945 eV, with similar peaks at approximately 929 and 933 eV corresponding to Pr^{3+} and Pr^{4+} ions, respectively [127]. The XRD and XPS results confirm that each synthesized sample predominantly contains the $LiTaO_3$ phase and maintains a similar percentage ratio of Pr^{3+} to Pr^{4+} ions in the crystal lattice, as depicted in Figure 4.3.1.1(e).

Sample no.	$LiTaO_3$	a = b (Aº)	c(Aº)	V(Aº)^3	Other phases		Pr^{3+}/Pr^{4+}
					$Li_2Pr_{0.67}Ta_2O_7$	$PrTaO_4$	
S1.	100 %	5.1572	13.7701	317.168	-	-	0.7/0.3 %
S2.	94.7 %	5.1537	13.7691	316.717	5.3 %	<1 %	1.8/0.9 %
S3.	95.5 %	5.1541	13.7646	316.662	<1 %	4.5 %	3.1/1.6 %

Table 4.3.1.1: Crystallographic parameters and percentages of other minor unintentionally synthesized phases present in S1, S2 and S3 samples.

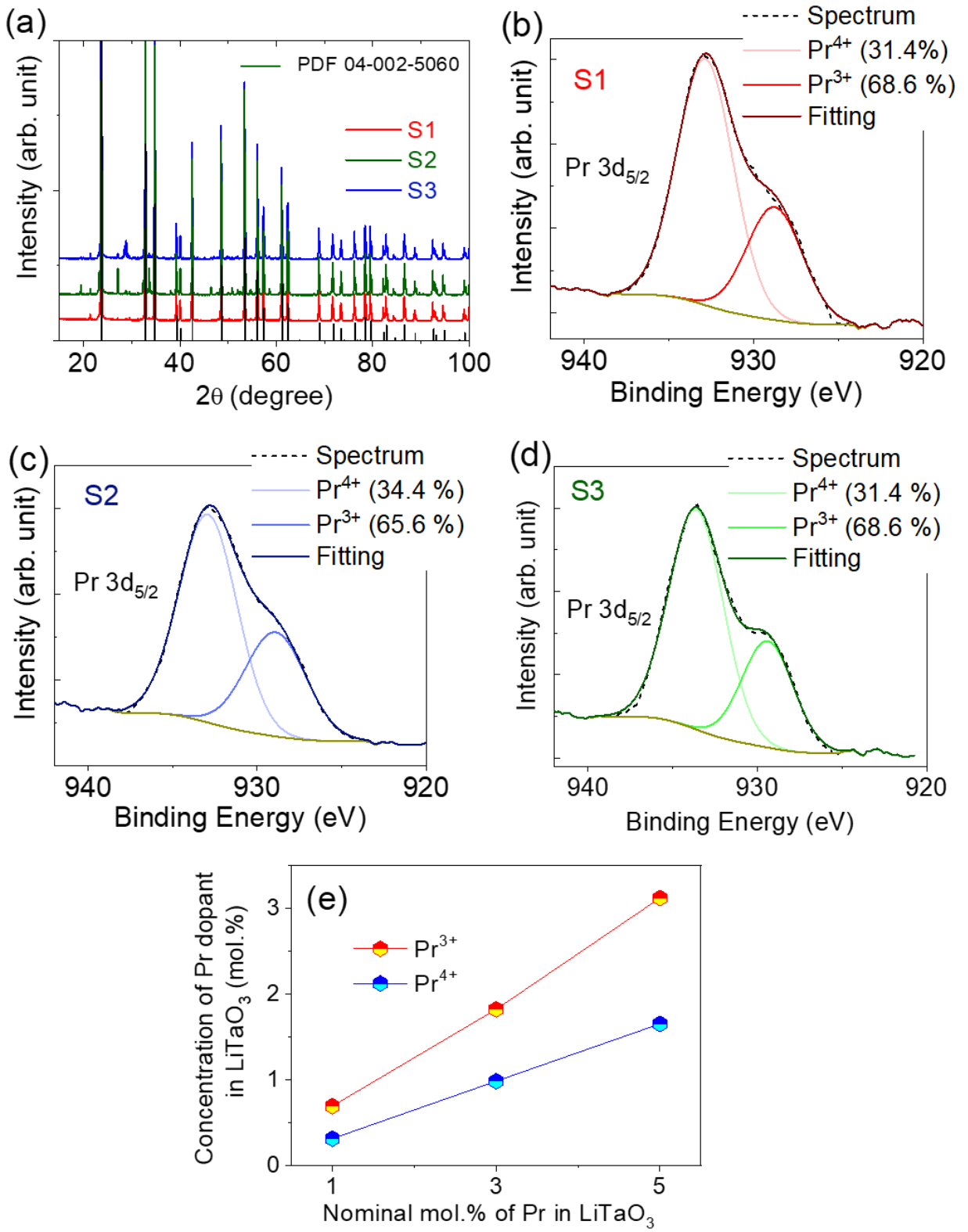

Figure 4.3.1.1: (a) The XRD patterns of the S1, S2, and S3 samples are compared with the standard PDF 04-002-5060 of $LiTaO_3$. The XPS spectra are presented for the (b) S1, (c) S2, and (d) S3 samples. (e) The concentration of Pr^{3+} and Pr^{4+} dopants in the $LiTaO_3$ lattice is shown as a function of the nominal mol.% of Pr doping in $LiTaO_3$.

4.3.2. Absorption and photoluminescence:

The optical band gaps for each sample were determined using the model proposed by Tauc, Davis, and Mott (Eqs. 4.3.2.1 and 4.3.2.2) from the square of the absorption coefficient presented in Figure 4.3.2.1(a).

$$(F(R_\infty))^n = C(hv - E_g) \qquad (4.3.2.1)$$

Here,

- "$F(R_\infty)$" represents the Kubelka-Munk function,
- "hv" is the photon energy,
- "E_g" is the optical bandgap energy, n, and C are the constants.

$$F(R_\infty) = \frac{K}{S} = \frac{(1-R)^2}{2R} \qquad (4.3.2.2)$$

Here,

- S is the scattering coefficient,
- K is the absorption coefficient,
- R is the reflection coefficient.

By extrapolating the linear portion of the absorbance spectra to the photon energy axis, the optical band gaps were estimated to be 4.47 eV, 4.35 eV, and 4.29 eV for the S1, S2, and S3 samples, respectively. This indicates a small decrease in the optical band gap as the Pr dopant concentration increases [65, 128, 129].

Figure 4.3.2.1(b) shows the PL excitation and emission spectra for the $LiTaO_3$ samples. The excitation spectra measured at an emission wavelength of 616 nm reveal two broad bands centered at 250 nm and 298 nm in the ultraviolet (UV) region, along with additional narrow peaks in the visible region beyond 435 nm. The broad bands are likely attributed to charge transfer in the oxide site and 4f→5d transitions of Pr^{3+} ions, while the sharp peaks are associated with $^3H_4 \rightarrow {}^3P_J$ (j=0,1,2) transitions [130, 131]. The emission spectra of each sample, excited at a wavelength of 298 nm, display two prominent peaks around 510 nm and 616 nm, corresponding to cyan and red emissions, respectively. Additionally, peaks observed at 500 nm, 512 nm, 563 nm, 616 nm to 650 nm, 673 nm, 712 nm, and 890 nm are attributed to the transitions $^3P_1 \rightarrow {}^3H_4$, $^3P_0 \rightarrow {}^3H_4$, $^3P_1 \rightarrow {}^3H_5$, $^1D_2 \rightarrow {}^3H_4/{}^3P_0 \rightarrow {}^3H_6/{}^3P_0 \rightarrow {}^3F_2$, $^3P_0 \rightarrow {}^3F_3$, $^1D_2 \rightarrow {}^3H_5$ and $^1D_2 \rightarrow {}^3H_6$ [129, 132-135]. All samples exhibit identical peak positions and intensities in their excitation and emission spectra, indicating that they possess similar luminescence centers [129]. Figure 4.3.2.1(c) illustrates the peak intensities at 511 nm and 616 nm as a function of Pr^{3+} concentration. This graph demonstrates that increasing the concentration of Pr dopant results in a reduction in peak intensities, attributed to the quenching effect of higher Pr ion concentrations. [136].

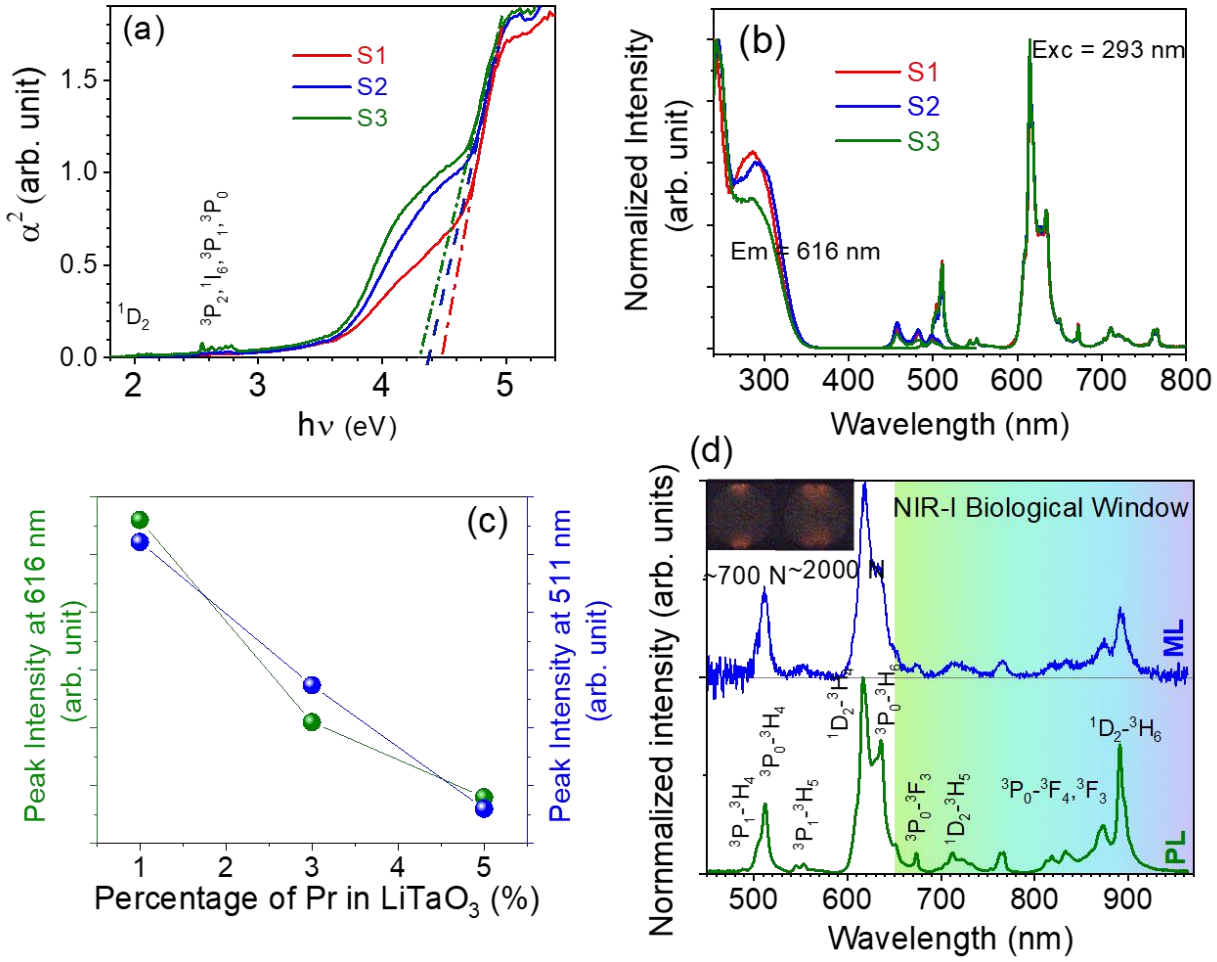

Figure 4.3.2.1: (a) Square of the absorption coefficient of S1, S2, and S3 samples, extracted from the diffuse reflection spectra. (b) Normalized PL excitation and emission spectra for S1, S2, and S3 samples. (c) Comparison of peak intensities at 511 nm and 616 nm for varying Pr^{3+} concentrations. (d) Comparison of the ML spectrum with the PL spectrum of S1, excited at 280 nm, including inset images of the S1 sample pellet under applied force.

4.3.3. Mechanoluminescence properties:

The ML spectrum of the S1 sample, measured using the F-ML setup, is compared with the PL spectrum in Figure 4.3.2.1(d). The figure also includes information on the NIR-I biological window and images of the S1 sample pellet under applied force. Both emission spectra (ML and PL) exhibit similar patterns with identical peak positions in the cyan, red, and infrared regions. This indicates that ML originates from the same luminescence centers as PL. Additionally, the ML spectrum shows that some emission peaks from the $LiTaO_3$:Pr sample fall within the NIR-I biological window, which could be beneficial for medical applications.

The experimental results of I-ML measurements for $LiTaO_3$:Pr (1% to 5%) are plotted in Fig. 4.3.3.1(a-c). The sharp peaks in the intensity vs. time curves indicate I-ML produced by the mechanical energy transfer from the projectile to the ML material during a collision [4]. Throughout the experiments, the UV exposure period (3 minutes) was fixed to ensure adequate loading of charge carriers into the shallow and deep traps. All samples exhibited a strong I-ML

signal at identical impact kinetic energies (~0.25 J), determined by the mass and speed of the projectiles. Fig. 3(a-c) shows the intensity curves of the samples (S1, S2, and S3) for 5 consecutive shots with a 1-minute delay between shots, following the cessation of UV exposure. No UV excitation occurred between the shots, and the impact kinetic energies were maintained at ~0.25 J for each shot. The peak I-ML intensity was normalized to 1 measured at the first shot (after a 1-minute delay), which decreased to 0.67 by the fifth shot (after a 5-minute delay) (see Figure 4.3.3.1(a)). The S2 sample exhibited a similar trend, with peak intensity at 0.92 for the first shot, decreasing to 0.62 by the fifth shot, compared to the S1 sample, as shown in Figure 4.3.3.1(b). The S3 sample displayed a significantly higher I-ML peak intensity, up to 2.1 times that of the S1 sample at the first shot, and retained 1.5 times the intensity by the fifth shot, as illustrated in Figure 4.3.3.1(c). Moreover, S3 demonstrated excellent retentively, up to 0.71. The normalized peak intensities for multiple shots are plotted as a function of time elapsed since the UV exposure was turn off for the S1, S2, and S3 samples in Figure 4.3.3.1(d). These experimental results indicate that the S3 sample has superior I-ML intensity and retentivity compared to the S1 and S2 samples.

To explore the energy-dependent I-ML properties of $LiTaO_3$:Pr samples, projectiles of varying masses (0.28 g, 0.25 g, 0.23 g, and 0.2 g) were used to shoot the samples. Figure 4.3.3.1(f) shows the normalized I-ML intensities of the S1, S2, and S3 samples at approximately 0.25, 0.26, 0.27, and 0.29 J energies (with S1 peak I-ML intensity values at different energies set as equal to 1). The normalized I-ML intensity for the S2 sample decreases from 1.7 to 1.1 as the impact kinetic energy declines. Similarly, for the S3 sample, it decreases from 4.4 to 3.1. These results indicate that the S2 and S3 samples do not exhibit the same ratio of charge carriers de-trapping at different energies compared to the S1 sample, confirming that they have trap levels with different energy depths and densities. Among all the samples, S3 has the optimal concentration of luminescence centers and trap levels for superior I-ML properties.

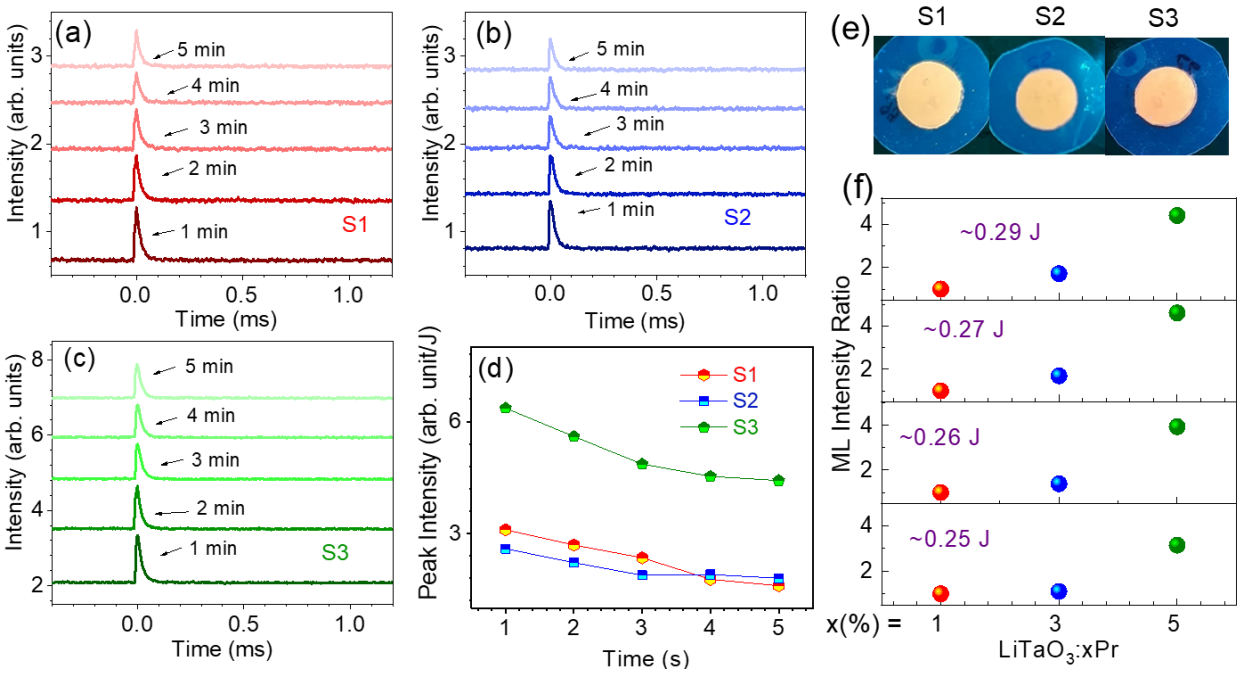

Figure 4.3.3.1: I-ML signals vs. time for (a) S1, (b) S2, and (c) S3 samples, (d) normalized peak intensity vs. time after UV exposure, (e) optical images of the powder films under UV exposure

confirming uniform distribution, and (f) I-ML intensity ratio for S1, S2, and S3 samples at different impact energies.

As the I-ML measurements indicated, S3 has good ML properties. Thus, only S1 (for comparison) and S3 samples are utilized for the exploration of S-ML properties. During S-ML measurements, mechanical stress is applied to cylindrical composite pellets (S1/Epoxy and S3/Epoxy) at uniform speeds (200, 300, 400, 500, and 600 mm/min) up to maximum compressive deformation (case 1 = 9% and case 2 = 14%). An optical camera captures S-ML visuals at high frame rates (55 fps), which helps to visualize the stress transformation within the pellet during mechanical impact. The S-ML is produced as a result of the de-trapping of charge carriers from the trap levels due to the local piezoelectric field created by applied mechanical stress [10]. Consequently, high-stress regions emit more intense light than low-stress regions, as seen in the images in Figure 4.3.3.2. The comparison of optical visuals of the S1 and S3 samples during applied mechanical stress at 600 mm/min until 14% deformation confirms the superior S-ML properties with less background persistent luminescence of the S3 sample. From 18 ms to 200 ms, the anvil continuously applied stress at a constant speed, producing intense S-ML in high-stress regions visible in the captured images. At 0.3 s, the pellet deformed up to 14%, and the anvil stopped with weak S-ML. The extracted pictures clearly exhibit the transformation of invisible stress within the structure as a function of time, proves $LiTaO_3$:Pr a suitable candidate for remote and real- time stress imaging applications.

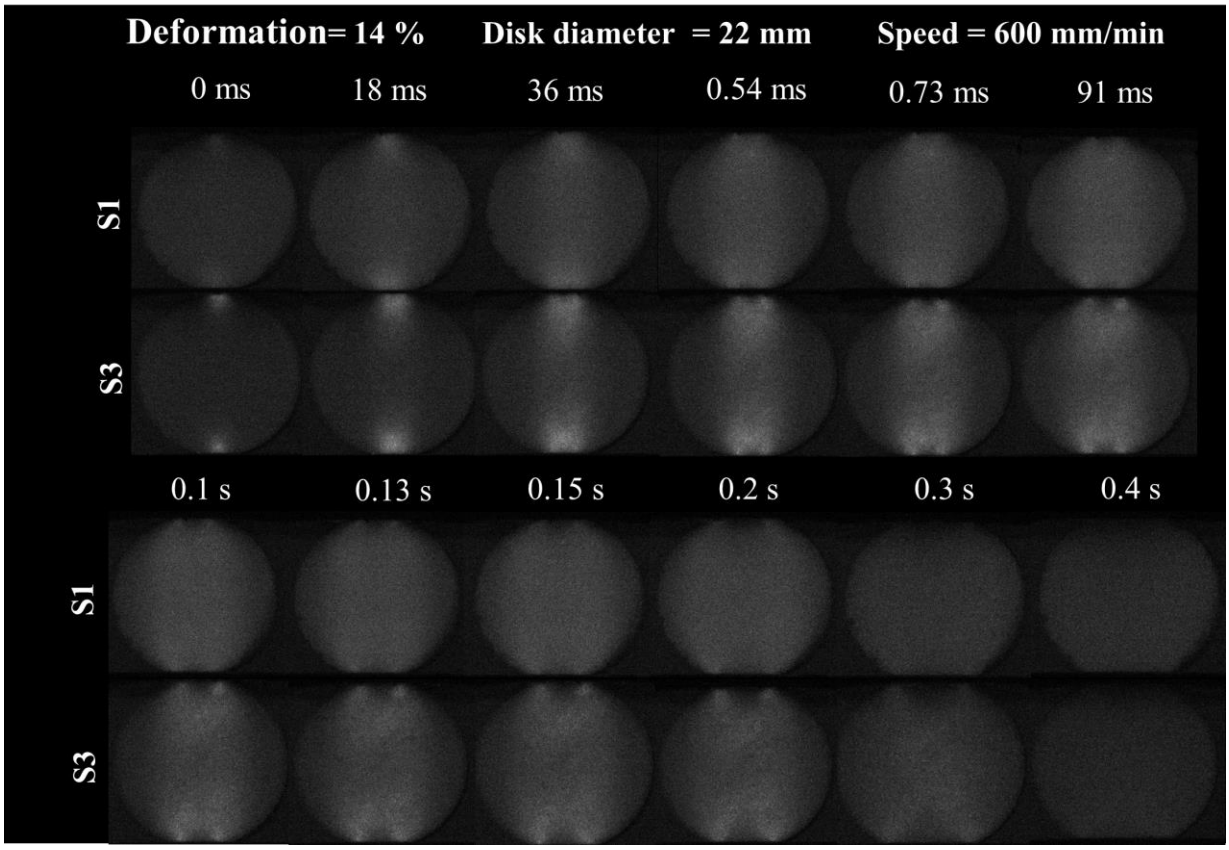

Figure 4.3.3.2: Comparison of S-ML images of stress transformation within S1 and S3 cylindrical pellets at 600 mm/min speed and maximum 14% deformation, captured at 55 fps.

By image processing of captured S-ML visuals at different speeds and deformation conditions, graphs are plotted and presented in Figure 4.3.3.3(a) and 4.3.3.3(b). These graphs describe the linear correlation between S-ML intensity and applied mechanical force as a function of time, indicated by a red dotted circle. Figure 4.3.3.3(a) shows the curves of applied force and S-ML intensity as a function of time at various speeds from 200 to 600 mm/min and up to 9% and 14% deformation of the S1 pellet. It can be observed that S-ML intensity perfectly follows the same pattern as the applied mechanical force with some deflection at low speed. These deflections may arise because most of the charge carriers are detrapped before reaching the maximum force. This suggests that at higher forces with slower rates, fewer charge carriers remain available in the trap states causing a decrease in ML intensity. Similar results are observed for the S3 sample with good intensity and overlapping between applied force and S-ML signals, as shown in Figure 4.3.3.3(b).

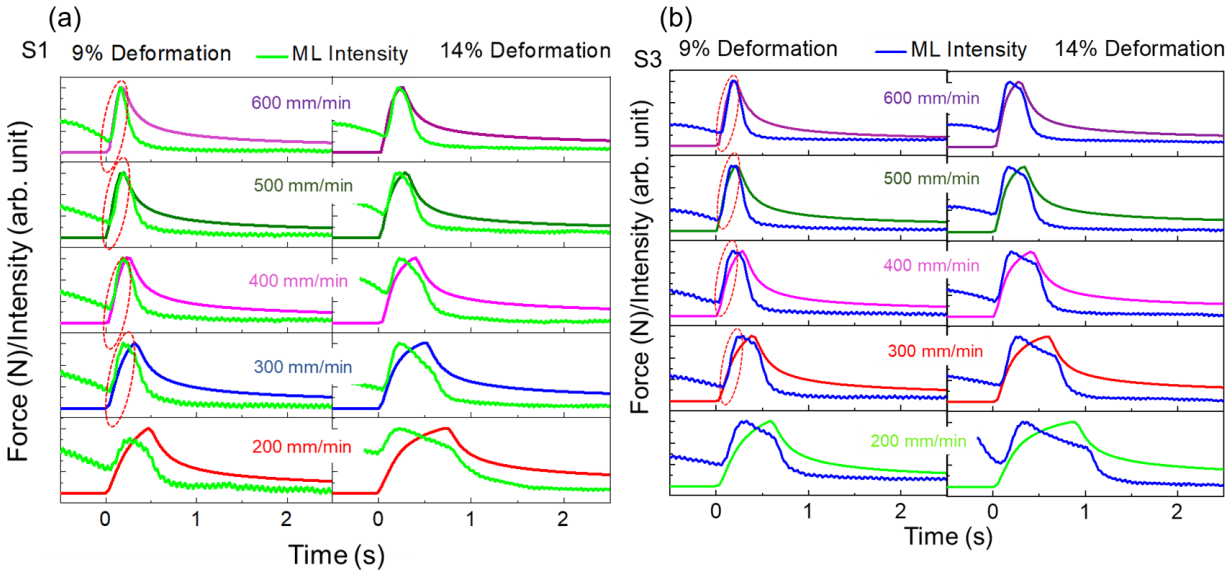

Figure 4.3.3.3: Overlapped applied force and S-ML intensity vs. time graphs at speeds ranging from 200 to 600 mm/min, with up to 9% and 14% maximum deformation for (a) S1 and (b) S3 cylindrical pellets (dimensions thickness = 10 cm, Diameter = 22 cm).

Additionally, the comparison between maximum force and S-ML intensity as a function of mechanical impact speeds for S1 and S3 samples is plotted in Figures 4.3.3.4(a) and 4.3.3.4(b) at 9% and 14% deformation, respectively. In all cases, peak S-ML intensities follow the same behavior as the maximum force at different speeds. These graphs show that the S-ML signal of S3 is more intense than S1. The extracted results of S-ML measurements prove that S3 is a suitable candidate for stress-sensing applications.

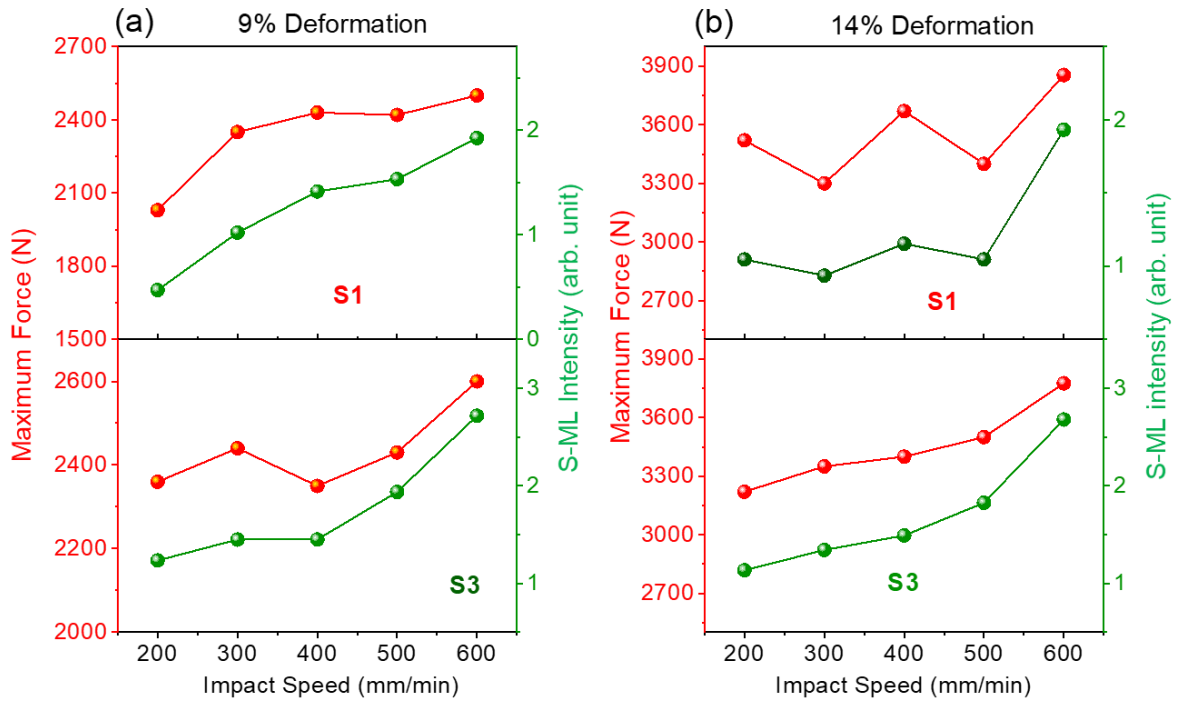

Figure 4.3.3.4: Comparison of maximum applied force and S-ML intensity as a function of impact speed for S1 and S3 samples at (a) 9% and (b) 14% deformation.

Furthermore, the curves demonstrating the correlation between the applied mechanical impulse and emitted integrated ML light intensity are plotted at 9% and 14% compression for the S1 and S3 samples (see Figure 4.3.3.5). Equations (4.3.3.1) and (4.3.3.2) are employed on the time-dependent force and intensity curves, respectively, for the calculation of the applied impulse and integrated ML light intensity. [137].

$$Impulse = \int f(t)\, dt \qquad (4.3.3.1)$$

$$Emitted\ light = \int I(t)\, dt \qquad (4.3.3.2)$$

Here,

- "$f(t)$" is the applied force,
- "$I(t)$" is the S-ML intensity,
- "t" is the time.

Figures 4.3.3.5(a) and 4.3.3.5(b) verify the linear correlation between the emitted light (captured by the camera) and the applied mechanical impulse for both samples. This indicates that the de-trapping of charge carriers depends not only on the imposed mechanical force but also correlates with the applied mechanical impulse.

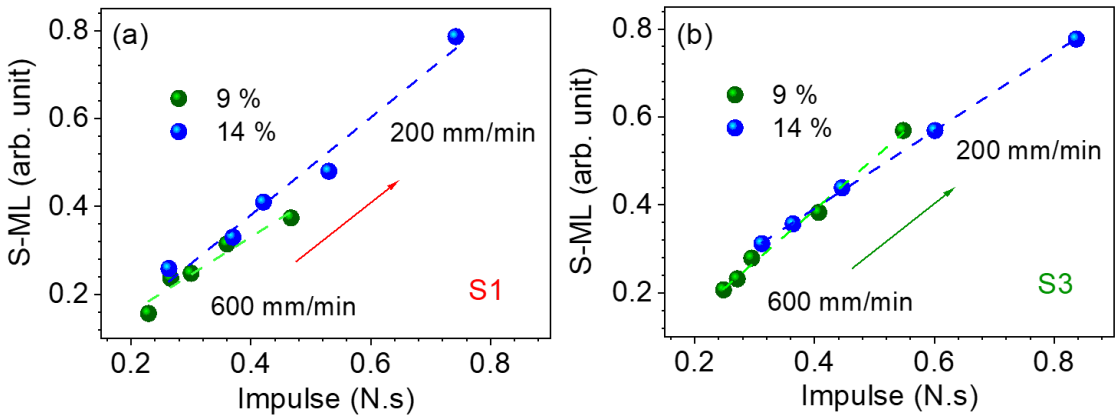

Figure 4.3.3.5: S-ML as a function of mechanical impulse at 9% and 14% maximum compressive deformation for (a) S1 and (b) S3 samples.

To capture S-ML in the infrared (IR) region, a photomultiplier was used instead of a camera, with a detection range from 185 nm to 870 nm with a glass filter that transmitted only wavelengths longer than 700 nm. Figures 4.3.3.6(a) and (b) compare the applied mechanical force and S-ML intensity in the IR region as a function of time for S1 at 9% and 14% compressive deformation, respectively. The results show that the IR S-ML intensity increases as force is applied to the S1 samples at various speeds and both deformation levels. These findings suggest that the IR S-ML produced in $LiTaO_3$:Pr material could be highly beneficial for stress sensing in biological applications. Additionally, the correlation between the emitted IR light (captured by the photomultiplier) and the applied mechanical impulse is plotted in Figure 4.3.3.6(c). The same equations (4.3.3.1) and (4.3.3.2) were used to calculate the emitted IR light and impulse. It is evident that the emitted IR light is also linearly related to the applied mechanical impulse, similar to the visible region, as shown in Figure 4.3.3.5(a).

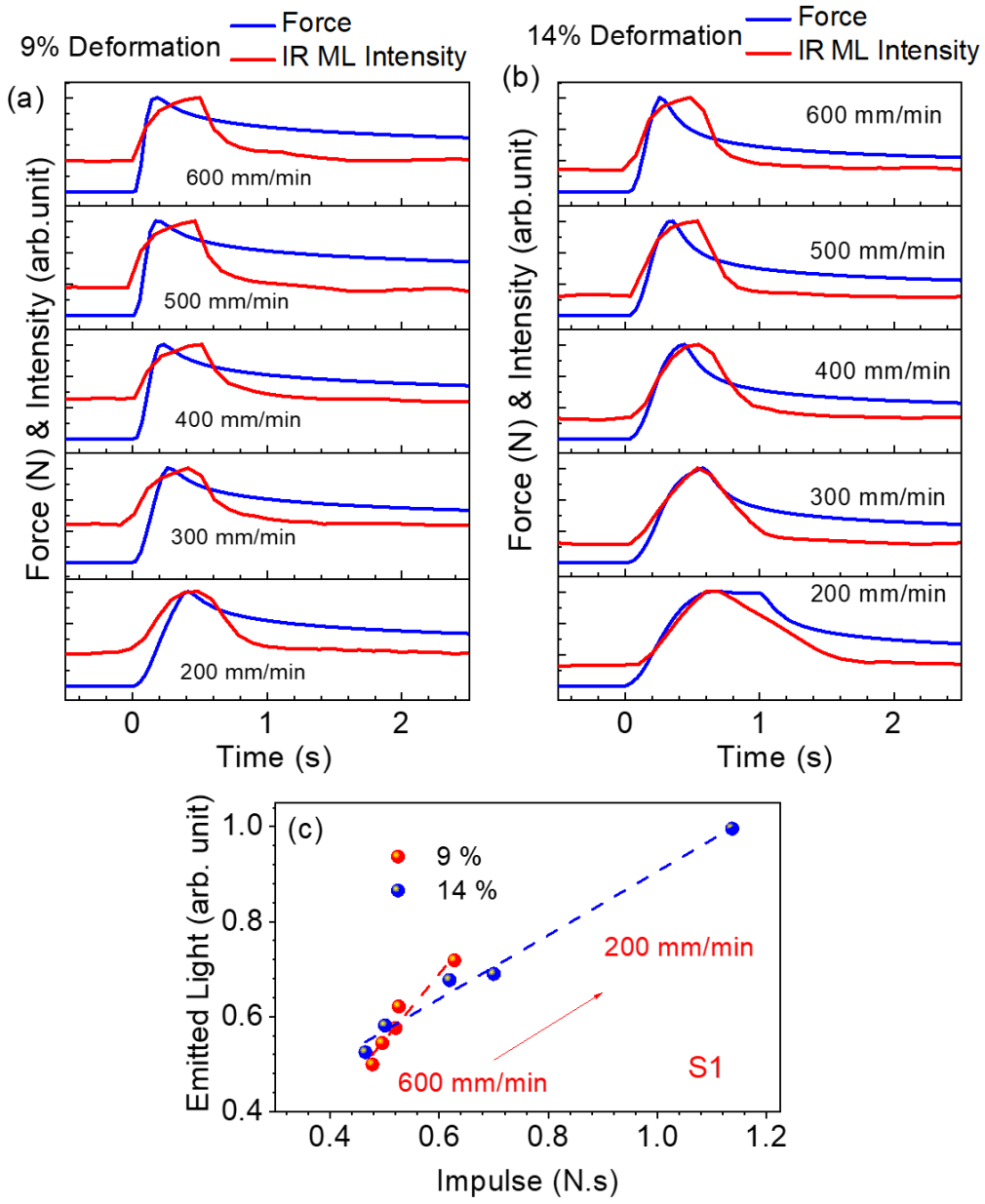

Figure 4.3.3.6: Overlapped applied force and IR S-ML Intensity curves as a function of time at (a) 9% and (b) 14% deformation for S1 sample, (c) Emitted IR radiation vs. applied impulse during stress application at 9% and 14 % deformation for S1 sample.

4.3.4. Persistent luminescence and Thermoluminescence:

To investigate PersL, all samples were irradiated with a 275 nm for 3 minutes, followed by measurement of the time-dependent intensity decay (PersL). Figure 4.3.4.1(a) displays the comparison of PersL curves for S1, S2, and S3 samples. The results indicate that S1 exhibits a stronger PersL compared to S2 and S3. This improved performance is likely due to S1 having a higher number of shallow traps. The majority of shallow traps in S1 lead to more efficient de-trapping of charge carriers at room temperature, thus enhancing the PersL of the S1 samples. PersL and ML arise from the trapping and de-trapping of charge carriers in trap levels. Therefore, it is crucial to examine the properties of these trap levels in the S1, S2, and S3 samples, including their types, concentrations, and energy depths [138-140]. To achieve this, TL measurements are

performed. In TL analysis, the peak intensity corresponds to the concentration of trapped charge carriers, while the peak position indicates the energy depth of the trap levels [141]. Figure 4.3.4.1(b) shows the TL curves for S1, S2, and S3 samples, measured after 3 minutes of 275 nm UV excitation, over a temperature range of -100 °C to 450 °C. The TL glow curves reveal several broad and narrow bands with varying peak positions, indicating the presence of multiple trap levels. Peaks observed between -100 °C and 150 °C are considered to shallow trap levels, while peaks above 150 °C correspond to deep traps. The TL curves support the findings from ML and PersL measurements: S1 exhibits a relatively higher concentration of shallow traps at room temperature compared to S2 and S3, which enhances its PersL. Additionally, Figure 4.3.4.1(c) compares the PersL curves of S1 with and without mechanical stress. Under the application of a 3500 N mechanical force at a speed of 10 mm/min, the luminescence increases during stress and sharply decreases when the stress is removed. This result confirms that both shallow and deep traps contribute to ML. ML is typically caused by deep trap levels resulting from point defects in the host material. These defects can arise from luminescent impurity doping or elemental deficiencies during the crystal synthesis process [15, 122]. The ML mechanism in $LiTaO_3$:Pr is relatively complex. Under UV exposure, both $LiTaO_3$ and Pr^{3+} ions absorb energy, which excites electrons from the valence band to the conduction band. These excited electrons then transfer energy to Pr^{3+} activators through transition states, potentially involving charge transfer states (CTS) [142]. Electrons in the excited states of Pr^{3+} ions eventually return to their ground states, emitting photoluminescence, while some are captured in shallow and deep trap states. After UV exposure is removed, electrons in shallow traps can easily escape at room temperature, whereas those in deep traps require additional energy stimulation, such as mechanical, thermal, or infrared radiation. During mechanical stimulation of piezoelectric materials, a locally induced piezoelectric field can enhance the rate of de-trapping, leading to the recombination of carriers at luminescence centers and producing ML. To illustrate the discussed ML mechanism, a schematic diagram is provided in Figure 4.3.4.1(d). The high ML efficiency observed in the S3 sample needs further explanation. As depicted in Figure 4.3.2.1(c), PL intensity decreases with increasing Pr concentration in the $LiTaO_3$ matrix, a phenomenon attributed to concentration quenching. This effect also impacts the TL results (see Figure 4.3.4.1(b)). Rough estimates of trap depths, E_{trap} (eV), based on TL peak positions, T_{TLpeak}, using the formula E_{trap} (eV) = T_{TLpeak} (K) / 500, yield values between 0.44 eV and 1.1 eV [143]. The TL intensity data reveal that samples S2 and S3 have relatively higher concentration of traps compared to sample S1. Although the I-ML efficiency of sample S2 is comparable to that of sample S1, this can be attributed to the relatively higher concentration of traps in sample S2 despite concentration quenching (see Figure 4.3.3.1(b)). The significantly higher I-ML efficiency of sample S3, compared to S2 and S1, is likely due to the increased Pr concentration in S3 (5% nominally, versus 3% in S2). This higher Pr concentration may limit energy migration to quenching centers, enabling a greater number of Pr^{3+} ions to be efficiently excited by mechanical impact. An intriguing observation from XPS is the substantial proportion of praseodymium ions in the Pr^{4+} oxidation state across all samples, which could be relevant for ML efficiency. Pr^{4+} ions might act as electron traps or quenching centers [144]. The role of Pr^{4+} ions in ML efficiency warrants further investigation, which will be addressed in future research.

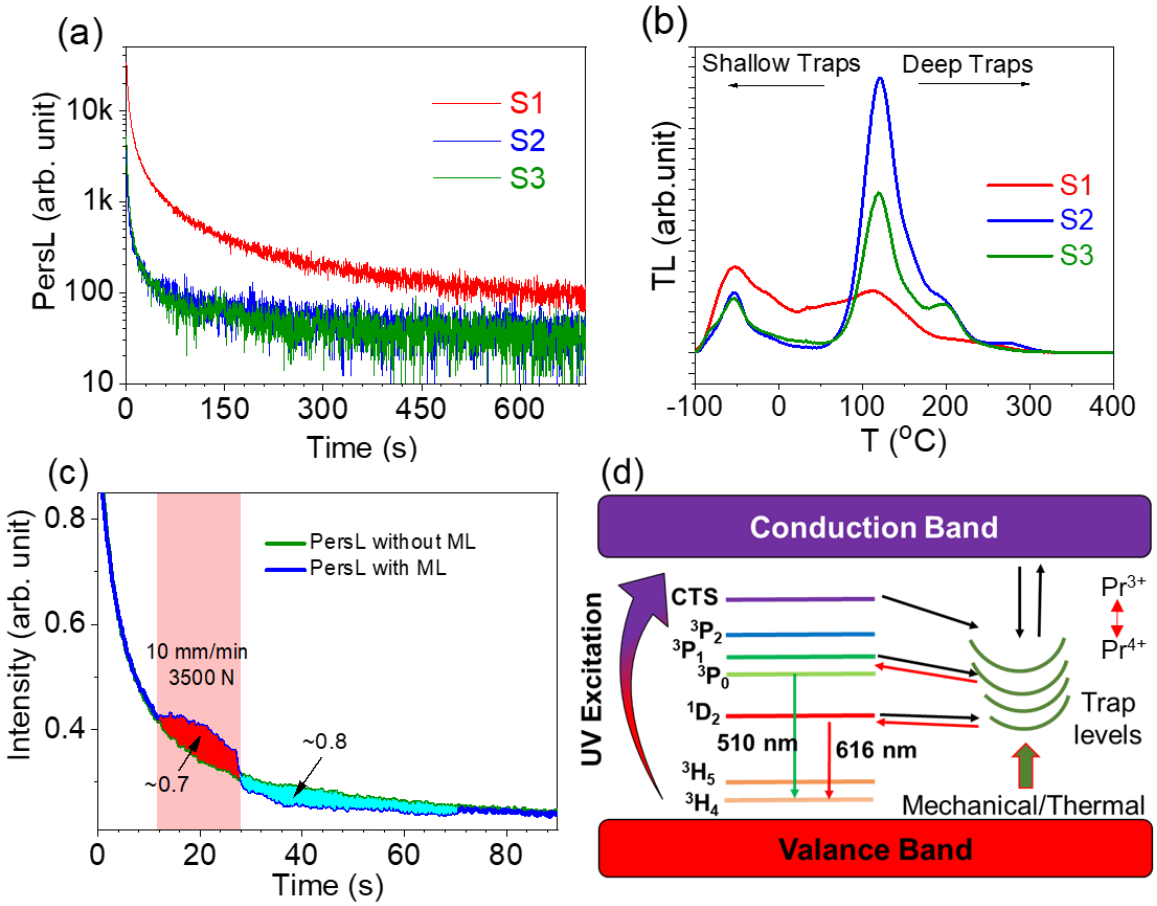

Figure 4.3.4.1: (a) the comparison of PersL curves of S1, S2, and S3 samples measured at room temperature. (b) Thermoluminescence glow curves of the S1, S2, and S3 samples, pre-excited at 275 nm. (c) Comparison of PersL as a function of time with and without mechanical stimulation upon S1/Epoxy pellet. (d) Schematic diagram illustrating the mechanisms of ML.

CHAPTER 5. Ultrasound-induced Luminescence of $LiTaO_3$: Pr

Recently, a distinct kind of luminescence has been observed by scientists during the exposure of ultrasound waves upon various luminescence materials as explained in Chapter 1. Commonly, it is known as ultrasound induced luminescence or ultrasound induced ML [28, 36]. In earlier investigation, we utilized $LiTaO_3$:Pr samples to comprehensively study their impact induced and stress induced ML properties [145]. Furthermore, we noted that these materials also exhibit infrared emission within the first biological window (NIR-I), rendering them valuable for medical applications. Following an extensive literature review, it became apparent that $LiTaO_3$ remains largely unexplored in terms of ultrasound-induced luminescence studies. Consequently, this knowledge gap motivated us to investigate the Us-L properties of $LiTaO_3$ host material doped with various concentrations of praseodymium. These varying amounts of Pr dopant were utilized to modulate the concentration and excitation energy of distinct traps beneficial for unveiling diverse behavior of Us-L. To the best of our knowledge, this is the first study to analyze the light emission from $LiTaO_3$:Pr at low (20 kHz) and high (3.3 MHz) frequency Us waves and various environmental temperatures, and documented with a complete set of information under the influence of ultrasound waves.

5.1. Experimental:

5.1.1. Preparation of $LiTaO_3$:Pr embedded PDMS films:

For the Us-L measurements, $LiTaO_3$:Pr (S1, S2 and S3) embedded PDMS films were prepared by homogeneously mixing 0.9 g PDMS and 0.1 g $LiTaO_3$:Pr powder. Later, 0.1 g of hardener is added. The final mixer is poured on the plastic mold having a hexagonal shape with a maximal diameter of 3 cm. The film is dried in an oven at 60 °C for 24 hours. The thickness of the films is 1 mm. The films are presented in Figure 5.1.1.1 under normal light and UV.

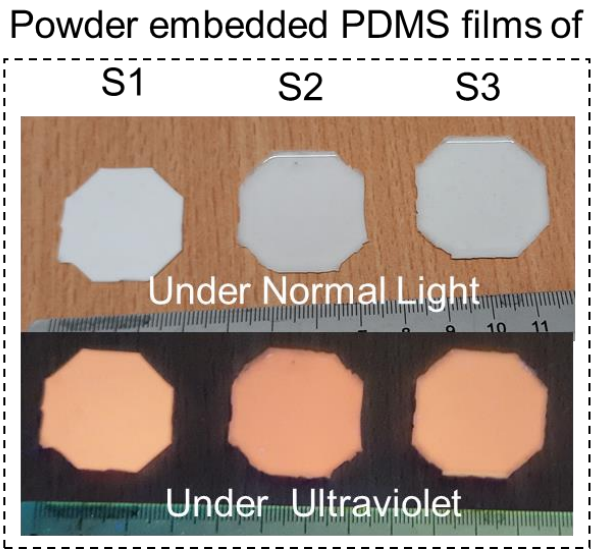

Figure 5.1.1.1: The optical photographs of the $LiTaO_3$:Pr powder embedded in PDMS films under normal light and ultraviolet light.

5.1.2. Measuring techniques:

Us-L experiments were conducted at a low frequency of 20 kHz using a self-designed experimental setup described in Chapter 3. The transducer was positioned perpendicular to the center of the film, aligning the transducer, film center, and collimation in a vertical axis to ensure sufficient light capture during sonication, the light emission during sonication was measured by photomultiplier. The distance between the transducer and the sample was fixed at 1 mm. Time-dependent luminescence intensity detected by the PMT was recorded using a multimeter and LabVIEW code run by computer. For temperature-dependent Us-L experiments at 20 kHz, first, the sample is brought in thermal equilibrium with water of a certain temperature (5°C, 23°C, 50°C, and 90°C. Secondly, the sample is UV excited in ambient air for 20 s, after which the Us starts. The temperature curves (measured by a thermocouple) as a function of time during the experiment are presented in Figure 5.1.2.1. During the Us-L experiments, the average temperature values are (12±2)°C, (23±2)°C, (31±3)°C, and (53±6)°C.

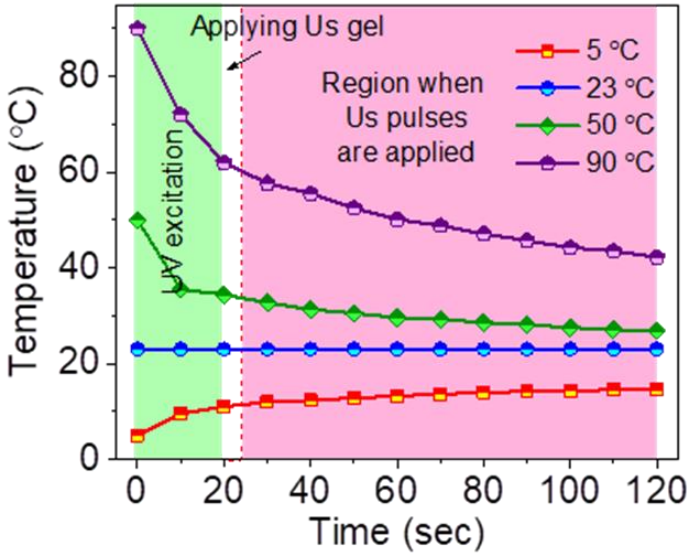

Figure 5.1.2.1: The change in temperature with time after removing from the fixed temperature beaker for temperature dependent Us-L measurements at 20 kHz.

For Us-L measurements at a higher frequency (3.3 MHz), we utilized a purpose-designed experimental setup explained in Chapter 2 [35, 146]. The UV excitation time for each sample was 3 minutes and the waiting time before Us beam exposure was 30 seconds. For measuring Us-L, the samples were exposed to the Us beam for 10 seconds. These parameters were identical for each sample in temperature and distance-dependent Us-L measurements. For Us-L intensity estimation, first calculate the mean of pixel values of each image by using open-source software ImageJ, then take the difference between lowest mean value (before Us exposure) and the maximum mean value (during the Us exposure). During temperature-dependent measurements at 3.3 MHz, the temperature of the water tank was maintained uniformly and constant at the desired value, and the distance between the sample and the Us transducer was fixed at 3 cm.

TL measurements were performed by the Horiba Fluorolog spectrometer and Linkam temperature control system. Before TL measurements, all the samples were preheated up to 450

°C for a few minutes to remove all the charge carriers from the energy traps. Later the samples were excited at 270 nm wavelength UV excitation source of Horiba Fluorolog for 5 min at -100 °C. The TL curves were captured in the temperature range from -100 °C to 450 °C at a heating rate of 0.5 °C/s, 1 °C/s, 1.5°C/s, and 2 °C/s.

5.2. Results and discussion:

The two distinct purposed-designed experimental setups are employed to investigate the Us-L properties. The first setup operates at a frequency of 20 kHz, resulting in acoustic cavity formation, growth, and collapse of vapor/gas bubbles in the medium, while the other setup operates at 3.3 MHz frequency, leading to acoustic streaming and the possible formation of convective cells, enhancing heat transfer [147, 148]. Different responses from S1 – S3 samples are related to dissimilar frequency-dependent ultrasonic phenomena active in these experiments.

5.2.1. Us-L properties at 20 kHz frequency:

First, we analyzed the Us-L properties of samples at different on/off durations (1 s/19 s, 2 s/18 s, and 3 s/17 s) with transducer vibrational amplitudes of 60 µm and 120 µm (see Figure 5.2.1.1(a)). Before conducting Us-L measurements, we exposed the samples to a UV source (LED diode refer to Chapter 3) with a wavelength of 270 nm for 2 minutes, followed by a 1 minute waiting period before applying the Us pulse. The experimental conditions for all samples were identical. Figure 5.2.1.1(a) displays distinct Us-L curves for different Us wave "On" durations (1 s, 2 s, and 3 s), with consistent 20 s interval cycles, repeated up to three times, represented by different peaks. These multiple peaks (marked in violet) indicate reproducible Us-L. Sample S1 exhibited significantly higher intensity (~10 times) compared to S2 and S3, attributed to a wide distribution of carrier traps and weaker concentration quenching. Increasing the pulse duration from 1 s to 3 s resulted in higher peaks and enhanced total intensity for S1 and S2, whereas S3 only experienced an increase in total intensity. Additionally, a zoomed-in view of the rectangular marked region of Figure 5.2.1.1(a), presents the first peak of each curve at 120 µm vibrational amplitude, clarifying the distinct Us response of all three samples (see Figure 5.2.1.1(b)). S1 showed a response to Us waves without peak intensity saturation up to the maximum pulse duration. It may happened because the presence of a larger number of 'intermediate' traps (around RT) can lead to significant retrapping, causing the observed emission to go via the relatively shallow traps (i.e. the ones giving TL around 0°C). This 'delays' the response, meaning that a longer Us exposure leads to the observed 'rise' in emission. S2 demonstrated low Us-L intensity without saturation up to the maximum pulse duration, while S3 exhibited a fast response with peak intensity saturation even after a 1s pulse duration, potentially due to concentration quenching. S2 not only exhibited excellent Us-L retention but also showed an increase in Us-L with an increasing number of pulses, particularly at a 120 µm vibrational amplitude. This behavior may be due to the retrapping of charge carriers from deep to shallow traps. It's worth noting that the S2 sample has a larger concentration of deep traps compared to S1 and S3 (see Figure 5.2.3.1(b)).

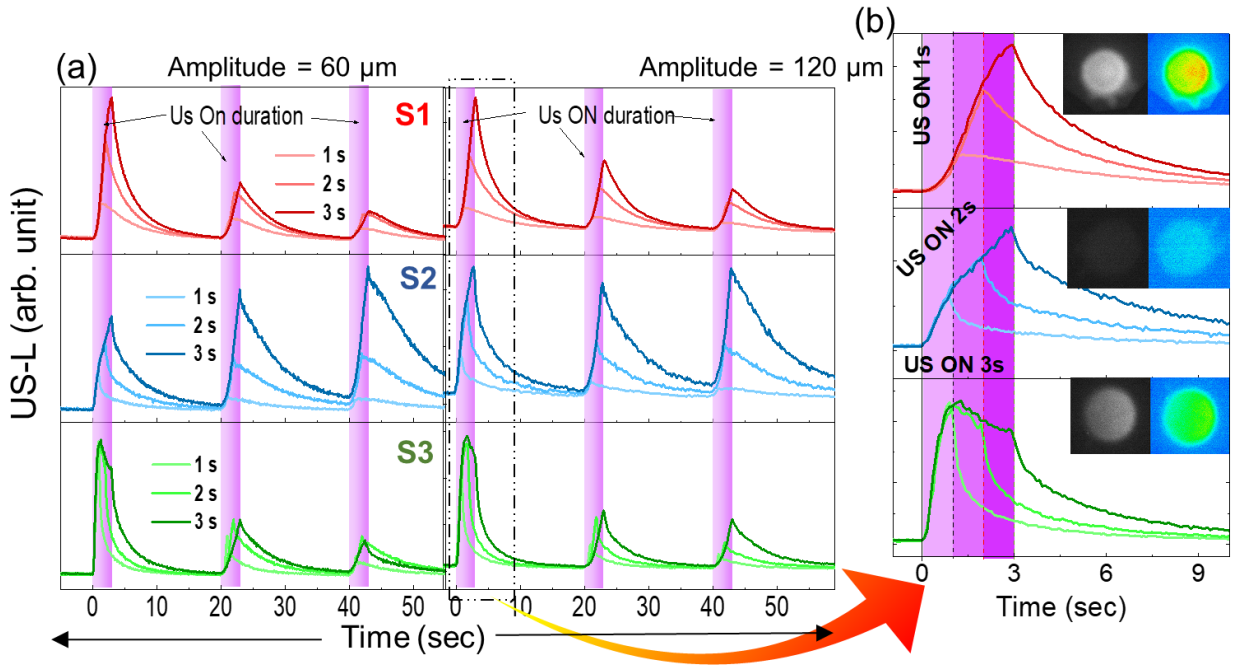

Figure 5.2.1.1: (a) Pulse duration (1s, 2s, 3s) dependent Us-L versus time curves for samples S1, S2, and S3 at 60 µm and 120 µm vibrational amplitude. Each curve displays three distinct Us-L peaks, corresponding to apply Us pulses with a 20 s time cycle. (b) Enlarged view of first Us-L peaks of each sample (marked with dotted rectangular) in graph (b) at 120 µm amplitude with an inset grayscale and contour images of emitted Us-L by each sample.

5.2.1.1. Vibrational amplitude-dependent Us-L:

Us-L intensity dependencies as a function of vibrational amplitudes from 24 to 120 µm with a step size of 24 µm were measured. The Us wave was applied in a cycle of 2 s/18 s (on/off) up to three times without UV exposure in-between. The UV excitation wavelength, UV exposure time, and waiting duration are 270 nm, 2 min, and 1 min, respectively. Figures 5.2.1.1.1(a – c) represent the relation of the peak value of Us-L with amplitude for each peak of S1, S2, and S3 samples, while the relation of the total Us-L value (calculated as the Us-L signal intensity integrated over each cycle of 20 s) of Us-L with amplitude is presented in Figures 5.2.1.1.1(d – f). For the S1 sample, peak Us-L and total Us-L are linearly related to the amplitude of Us waves with decreasing slope for consecutive peaks (see Figures 5.2.1.1.1(a) and (d)). The peak Us-L of the S2 sample also exhibits linear behavior with amplitude, surprisingly having the same slopes for each Us-L peak (see Figures 5.2.1.1.1(b)). The overlapping of the 2nd and 3rd peaks for S2 suggests the identical behavior of their peak Us-L emission for consecutive pulses, indicating the good retention of Us-L in the S2 sample. In contrast, the slope of total Us-L gradually increases with the number of peaks (see Figures 5.2.1.1.1(e)). It may happen because of the retrapping of charge carriers in shallow traps by initially applied Us pulses, which became available for upcoming applied Us pulses causing increases in total Us-L.

Let us consider the S3 sample, its peak Us-L shows the identical performance to the S1 sample which means the slope decreases with a peak's number (see Figures 5.2.1.1.1(c)). While the slope of the total Us-L is similar for each peak suggested the retrapping of charge carriers in shallow

traps like S2 sample (see Figures 5.2.1.1.1(f)). The slope represents the relative response of the Us-L peaks upon the applying Us pulse. Since force is linearly related to amplitude, it means Us-L at 20 kHz also linearly correlates with the applied force by the transducer. This observation suggests that the Us-L at 20 kHz may be produced as the result of the detrapping of the charge carriers by forced-induced piezoelectric field. The outcomes proposed that Us-L at 20 kHz is mainly induced by mechanical stimulus (pressure waves), and consecutive piezoelectric field. A heating of the ultrasound transmitting medium may also occur, however it seems to occur for longer times of exposure to Us.

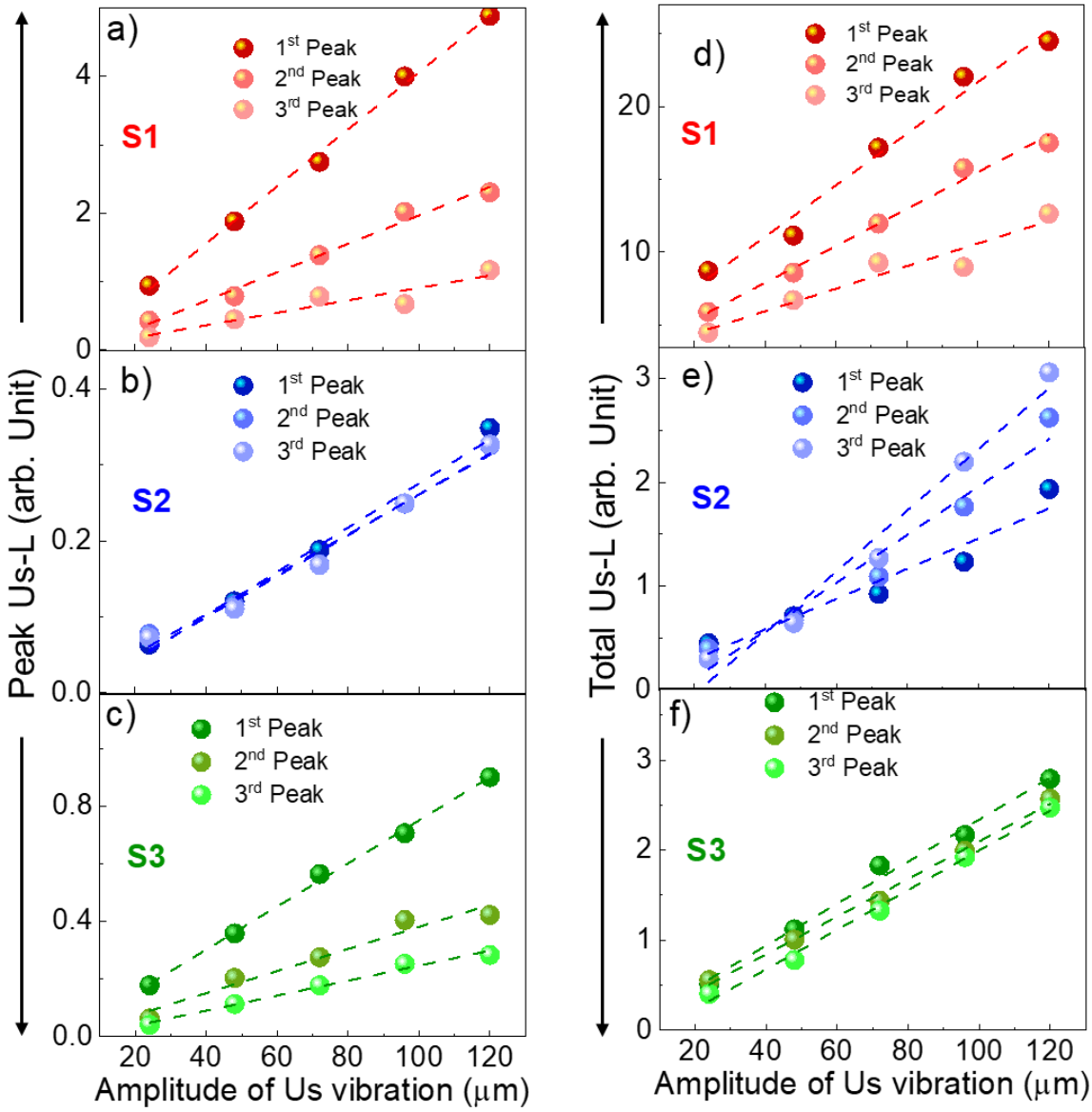

Figures 5.2.1.1.1: The Peak Us-L intensity of (a) S1, (b) S2, and (c) S3 versus vibrational amplitude of applied Us waves at 20 kHz and 2 s/18 s (on/off ratio). Total Us-L intensity of (d) S1, (e) S2, and (f) S3 versus vibrational amplitude of applied Us waves at 20 kHz and 2 s/18 s (on/off ratio).

5.2.1.2. Temperature-dependent Us-L:

To study the effect of temperature and verify the ML nature of Us-L emitted from $LiTaO_3$:Pr at 20 kHz, we implement a specific experimental procedure explained in the experimental section. The outcomes are plotted in Figure 5.2.1.2.1. Figure 5.2.1.2.1(a) shows the Us-L dependencies upon temperature during the application of multiple Us pulses (each for 2 s on) with an off-duration of 18 s at a measured temperature of 12°C, 23°C, 31°C, and 53°C. In S1, a gradual decrease in Us-L of each peak is observed by increasing temperature. However, in the S2 sample, Us-L of the 1st peak decreased with the temperature's increase while other peaks remained constant. In contrast, the first two peaks of the S3 sample decreased whereas others remained the same at different temperatures. For detailed analysis, the peak and total Us-L of the first two peaks are plotted as a function of temperature in Figures 5.2.1.2.1(b) and (c) respectively. The peak and total Us-L of S1 decrease linearly with temperature and lowest at 53°C for both peaks. In the S2 sample, only the peak Us-L of 1st peak is decreased while its total Us-L and Us-L values of the 2nd peak remain constant with small fluctuations at different temperatures. The observed behavior of the S2 sample validates its good Us-L retentive properties up to 53°C. The S3 sample shows diverse behavior, a sudden decrease in Us-L at high temperatures is observed in the 1st peak while the 2nd peak shows constant behavior with a slight decrease in peak Us-L. The outcome of temperature-dependent measurements indicates that the Us-L associated with the 1st peak tends to be higher at lower temperatures across various samples (see inset graphs in Figure 5.2.1.2.1(b)). This may happen because, at low temperatures, persistent luminescence does not occur, as the majority of charge carriers are trapped and prevented from detrapping and recombination before ultrasound exposure. The results of temperature-dependent Us-L also validate the ML nature of Us-L at 20 kHz. Since $LiTaO_3$:Pr shows emission in the IR region as well (see Figure 5.2.1.2.1(d)), we also measured the temperature-dependent Us-L in the Infra-red region at 12°C, 23°C, 31°C, and 53°C for S1, S2, and S3 samples presented in Figures 5.2.1.2.1(d-f). Identical outcomes are observed in the IR region as in the visible region. This would suggest that the recombination at Pr3+ occurs at a relatively high energy levels. S1 and S3 samples have good IR Us-L at low temperatures while IR Us-L of S2 is not much affected by temperature (see Figures 5.2.1.2.1(e) and (f)).

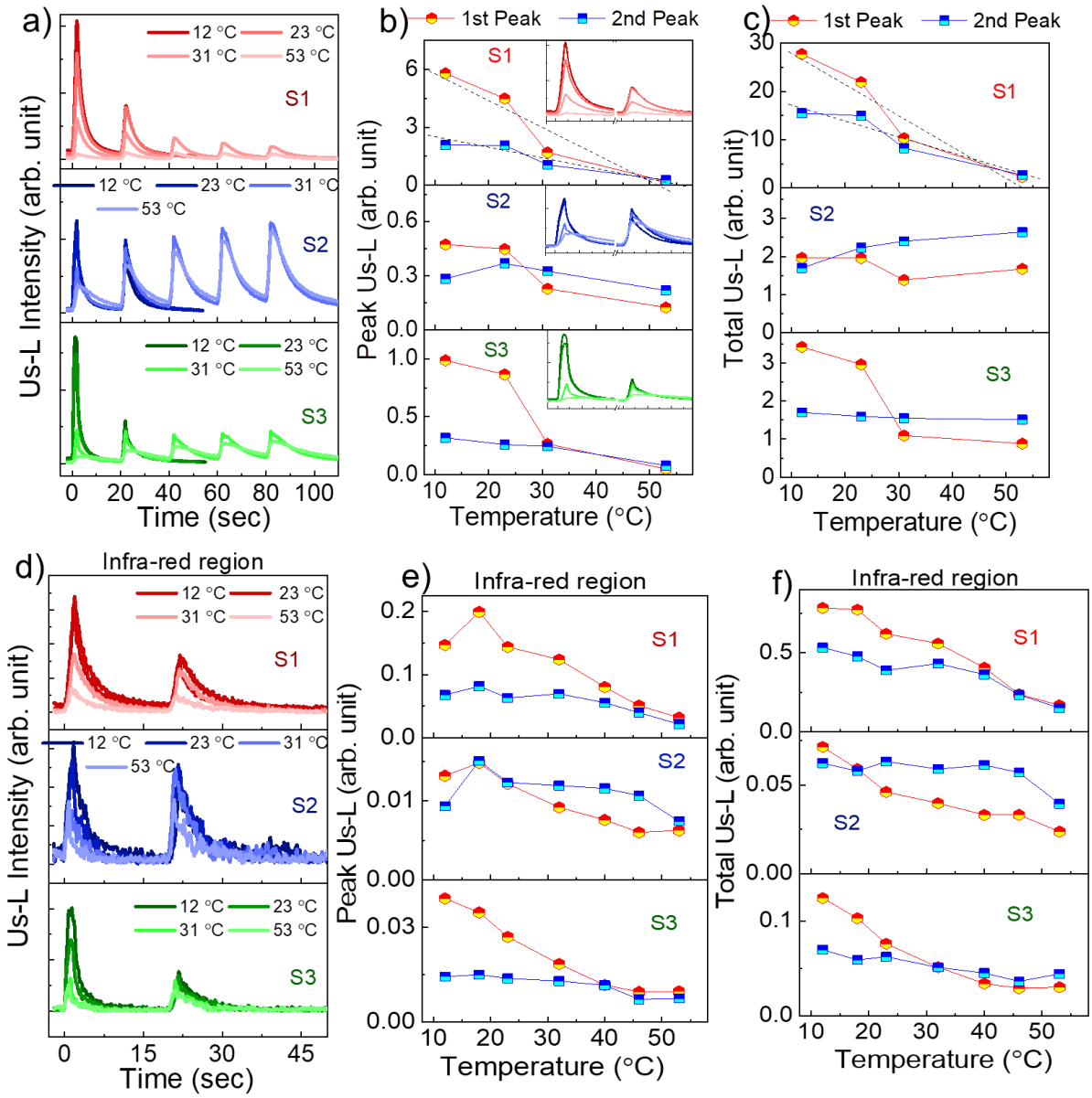

Figure 5.2.1.2.1: (a) Us-L Intensity in the visible region as a function of time during application of ultrasound pulses for 2 s with 96 µm vibrational amplitude at 12 °C, 23 °C, 31 °C and 53 °C for S1, S2, and S3. Temperature-dependent (b) Peak Us-L values and (c) Total Us-L values for the 1st and 2nd peak of S1, S2 and S3 samples. (d) Us-L Intensity in IR region as a function of time during application of ultrasound pulses for 2 s with 96 µm vibrational amplitude at 12 °C, 23 °C, 31 °C and 53 °C for S1, S2, and S3. (e) Peak IR Us-L values and (f) Total IR Us-L values for the 1st and 2nd peak of S1, S2 and S3 samples.

To better understand how higher temperatures affect the retention of Us-L in $LiTaO_3$:Pr samples, we created plots showing normalized (normalized by the value of 1st Us-L peak of S1 sample) peak and total values of Us-L as a function of the number of peaks (refer to Figure 5.2.1.2.2(a) and (b)). At 31°C, the peak Us-L values for S1 and S3 decrease as the peak numbers increase, while S2 shows an incremental trend. On the other hand, the total Us-L values for S2 and S3 increase with the peak number, indicating a dense occurrence of deep traps in these samples, which is beneficial for high-temperature Us-L properties. In contrast, S1, reliant solely

on shallow traps, shows a different behavior. A distinct pattern is observed in the peak and total values of S3 due to Us-L saturation, as explained previously. At 53°C, shallow traps are unable to be filled via UV exposure, leaving only deep traps available for Us-L emission. In this scenario, the presence of a high concentration of deep traps in S2 and S3 becomes significant.

The graph in Figure 5.2.1.2.2(c) shows the Us-L retention assessment of each sample at ambient temperature. These measurements are important for using $LiTaO_3$:Pr samples in the reproducible Us-L sensing domain. The cyclic Us-L signals are generated at 20 kHz under ambient conditions with direct contact between sample film and transducer, ranging up to 28 cycles. The graph confirms that sample S2 displays the best Us-L retention, likely due to its high density of deep traps. On the other hand, samples S1 and S3 exhibit lower Us-L retention compared to sample S2. Remarkably, the graph shows that achieving Us-L retention without exposure to UV excitation between cycles demonstrates that $LiTaO_3$:Pr is a suitable choice for industrial and medical applications. Additionally, the response and recovery time of samples S1, S2, and S3 are estimated by the Us-L signal, sensing a 1 second duration of Us wave pulse at 20 kHz as presented in Figures 5.2.1.2.2(d-f). The S2 and S3 sample demonstrates a fast response and recovery time to Us wave exposure, validating its significant ultrasonic sensing capability compared to samples S1. The difference between S2 and S3 should not be overinterpreted, as the lower signal for S2 (and thus, possibly some background noise effects).

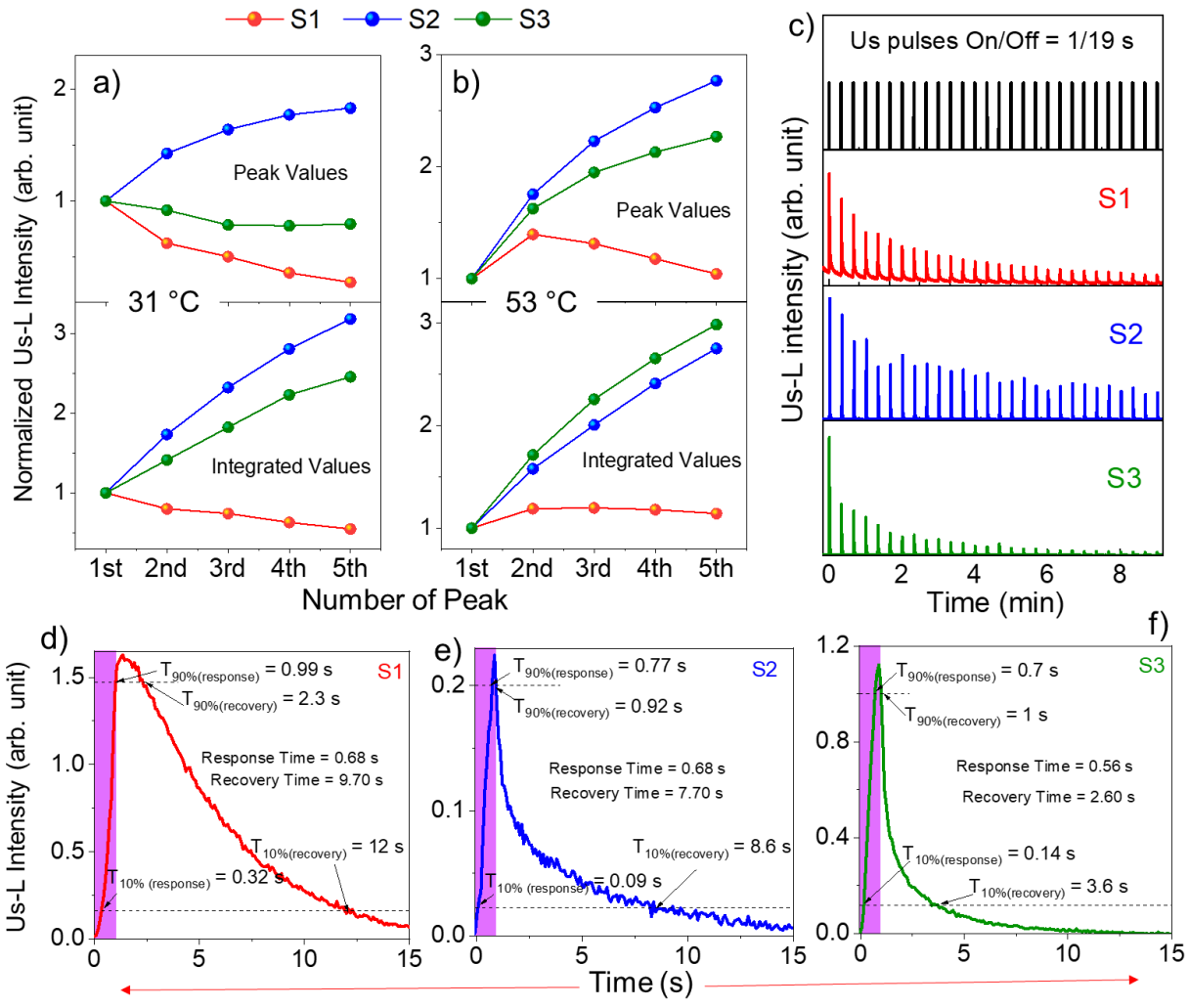

Figure 5.2.1.2.2: Normalized Us-L peaks and total values versus the number of peaks of S1, S2, and S3 samples at (a) 31 °C and (b) 53 °C temperatures. (c) Us-L reproducibility test at direct contact (without Us gel) between transducer *(20 kHz) and the sample films at room conditions up to 28 cycles 1/19 s on/off ratio. The Us wave sensing ability of (d) S1, (e) S2, and (f) S3 samples in the form of the Us-L signal exhibiting response and recovery time.*

5.2.2. Us-L at 3.3 MHz frequency:

The experimental observation of high frequency (3.3 MHz) temperature-dependent Us-L for S1, S2, and S3 samples, are presented in Figure 5.2.2.1(a-d). The calculated wavelength of the Us waves in a water medium is 0.45 mm, which is less than the sample thickness (1 mm). Notably, a linear increase in Us-L intensity with the water medium temperature is observed for S1 up to 30 °C (see Figure 5.2.2.1(a)), while S2 and S3 exhibit this trend up to 40 °C (see Figures 5.2.2.1(b) and (c)). This distinctive temperature dependence is attributed to variations in trap distribution and concentration within each sample. S2 and S3, characterized by relatively higher concentration of deep traps, demonstrate a sustained linear relation with temperatures up to 40 °C. This phenomenon suggests the advantageous role of deep traps, particularly at elevated temperatures, in enhancing Us-L intensity. However, this linear behavior of Us-L with the temperature of the medium is not fit to any established theory, it is just an experimental observation. In contrast, overall Us-L intensity is comparatively higher for S1 samples, owing to the good combination of trap distribution and concentration, particularly at lower temperatures. This result highlights the importance of a balanced distribution of traps across different energy levels influencing Us-L emission. We expected intense Us-L emission at 10°C and 20°C, mirroring outcomes observed in a 20 kHz setup. However, experimental results, indicate low Us-L emissions for all samples at low temperatures. This unexpected finding aligns with the conclusions drawn by Michels et. al. that Us-L is caused by the thermal release of trapped carries instead of ML-driven [35], asserting that at lower temperatures, the thermal energy imparted by the ultrasound waves is insufficient to trigger the de-trapping of a substantial number of traps, resulting in low Us-L emission. As the temperature rises, a discernible increase in Us-L emission is observed across all samples. This observation corresponds with the idea that, at higher temperatures, the thermal energy generated by high-frequency ultrasound waves becomes more effective in facilitating the removal of traps, leading to intensified Us-L emission. Particularly, S2 displays a more pronounced increase in Us-L compared to S1 and S3. This enhancement in Us-L can be attributed to the relatively higher concentration of deep traps in S2, suggesting a correlation between trap concentration and the observed increase in Us-L intensity. Moreover, at the highest temperature (50°C), the S2 sample has the strongest Us-L among them justified by its relatively high concentration of deep traps (refer to bar plot Figure 6.2.2.1(d)). Overall Us-L for each sample is low at 50°C because the thermal energy of the medium already removes most of the charge carrier from traps in between UV and ultrasound exposure. Our finding perfectly aligns with Michels et. al.'s conclusion that the Us-L at MHz frequency is caused by the de-trapping of charge carriers due to thermal energy produced during ultrasound exposure representing TL [35, 146].

Furthermore, distance-dependent ultrasound measurements were conducted at distances of 3, 5, 10, and 15 cm between the Us source and the sample film. The extracted results from these measurements, as presented in Figure 6.2.2.1e, indicate that the S1 sample possesses a long-range

capability of Us wave detection, extending up to 15 cm. In contrast, S2 and S3 samples exhibit a shorter range of detection, up to 10 cm. This difference in detection range can be attributed to the high concentration of shallow traps present in S1 compared to S2 and S3, as well as distance-dependent variations in the radiation field of the employed ultrasound transducer (3.3 MHz) [33].

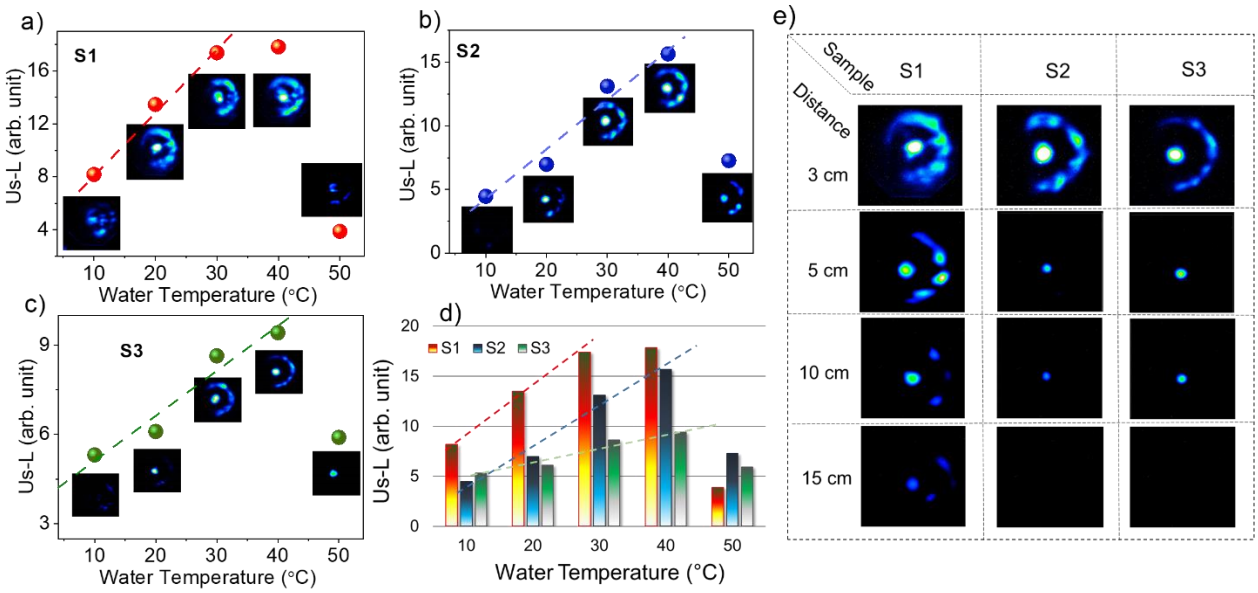

Figure 5.2.2.1: Us-L at 3.3 MHz frequency setup as a function of water temperature of (a) S1, (b) S2, and (c) S3 at 3.3 MHz, distance b/w transducer and sample film is 3 cm, intensity is 2 W/cm^2. (d) Bar plot to exhibit the Us-L trend with the medium temperature for each sample. (e) Us-L images of samples at different distances from 3 to 15 cm of S1, S2, and S3. (Linear behavior is not fit to any theory, just an experimental observation).

5.2.3. Thermoluminescence and trap analysis:

To understand the diverse behavior of Us-L properties exhibited by S1, S2, and S3 samples, we estimated the depths of the traps (thermal activation energies) using the Hoogenstraaten method [149]. Figures 6.2.3.1(a-c) shows the TL curves measured at heating rates of 0.5, 1, 1.5 and 2 °C/s. Among them, the S2 sample has a relative higher concentration of deeper traps validated by the TL intensity while S3 has a moderate concentration of traps. The TL glow curve of S1 exhibits lower intensity and relatively broader bands compared to the TL glow curves measured for S2 and S3. This suggests that the concentration of traps in S1 is smaller, and the activation energy distribution of these traps is broader than in the case of S2 and S3 samples. Figures 6.2.3.1(d-f) show the estimated values of energy depth of each trap by employing the Hoogenstraaten method for S1, S2, and S3, respectively. The Hoogenstraaten method uses the correlation between the heating rate (β) and the temperature (T_{max}) of the peak in a glow curve described by the Equation (6.2.3.1).

$$\frac{\beta E}{kT_{max}^{\ 2}} = se^{\left(-\frac{E}{kT_{max}}\right)} \qquad (5.2.3.1)$$

Where,

- k is the Boltzmann constant,
- β is the linear heating rate,
- T_{max} is the temperature of the peak in a glow curve,
- E is the energy of the trap, and s is the frequency factor.

Since the eqn. 5.2.3.1 refers that $ln\left(\frac{T_{max}^2}{\beta}\right)$ is proportional to $(kT_{max})^{-1}$ with a coefficient equal to E, we evaluate activation energies of the prominent traps present in S1, S2, and S3 samples by the slope of the linear fitting. The outcomes demonstrate that all three samples have five visible traps from shallow to deeper regions. In the case of S1, two traps (T5-1.44 eV and T4-0.98 eV) are considered deeper (see Figure 6.2.3.1(d)). The reason behind the high-intensity Us-L of the S1 sample may be the value of energy difference between the traps (ΔE_{2-1} = 0.08 eV, ΔE_{3-2} = 0.1 eV, ΔE_{4-3} = 0.35 eV, ΔE_{5-4} = 0.46 eV) that is not too high, cause easy transfer of charge carriers at low activation energy from deeper to shallow traps and later recombine at luminescence centres. Moreover, the S1 has relatively higher concentration of shallow traps (in comparison to S2 and S3 samples) and also enhances its Us-L and PersL (Chapter 4) among them. In the case of the S2 sample, the significant energy gap (ΔE_{2-3} = 0.46 eV) between the deeper and shallow traps enhances its ability to store charge carriers for a long into the deeper traps (see Figure 6.2.3.1(e)). Furthermore, relatively higher concentration of deeper traps in comparison to others also improves its retentivity and Us-L performance at high-temperature medium. The S3 sample has a different behaviour because of its intermediate trap distribution (see Figure 6.2.3.1(f)). In the S2 and S3 samples, the difference of about 0.45 eV between T2 and T3 traps plays a positive role in enhancing their response to Us waves, resulting in the fastest response and recovery times. TL results prove that the concentration of Pr dopant effectively modulates the distribution and concentration of traps. Due to the dissimilar concentration and distribution of energy traps in different percentages of Pr dopants in $LiTaO_3$ samples, diverse Us-L properties are observable and would be beneficial for a wide range of ultrasonic sensing and imaging applications.

Figures 5.2.3.1(g-i) illustrate the relationship between band gap changes and activation energy variations with different concentrations of Pr. It is observed that the deeper trap, T5, exhibits a pattern similar to the typical for a deep electron trap energy dependence., i.e. its energetic position in the band gap is independent of the band-gap energy. Therefore decrease in the band gap results in a decrease of the transition energy between the trap and the bottom of the conduction band. The other traps show an opposite trend (see Figures 5.2.3.2). This suggests that T5 might be associated with an electron trap, whereas the other traps are likely related to holes. Additionally, it is suspected that there might be six traps in total, as T2, visible in the S1 sample, appears to shift to higher energy levels in the S2 and S3 samples. However, it is possible that T2 either disappears or becomes too weak to detect in S2 and S3.

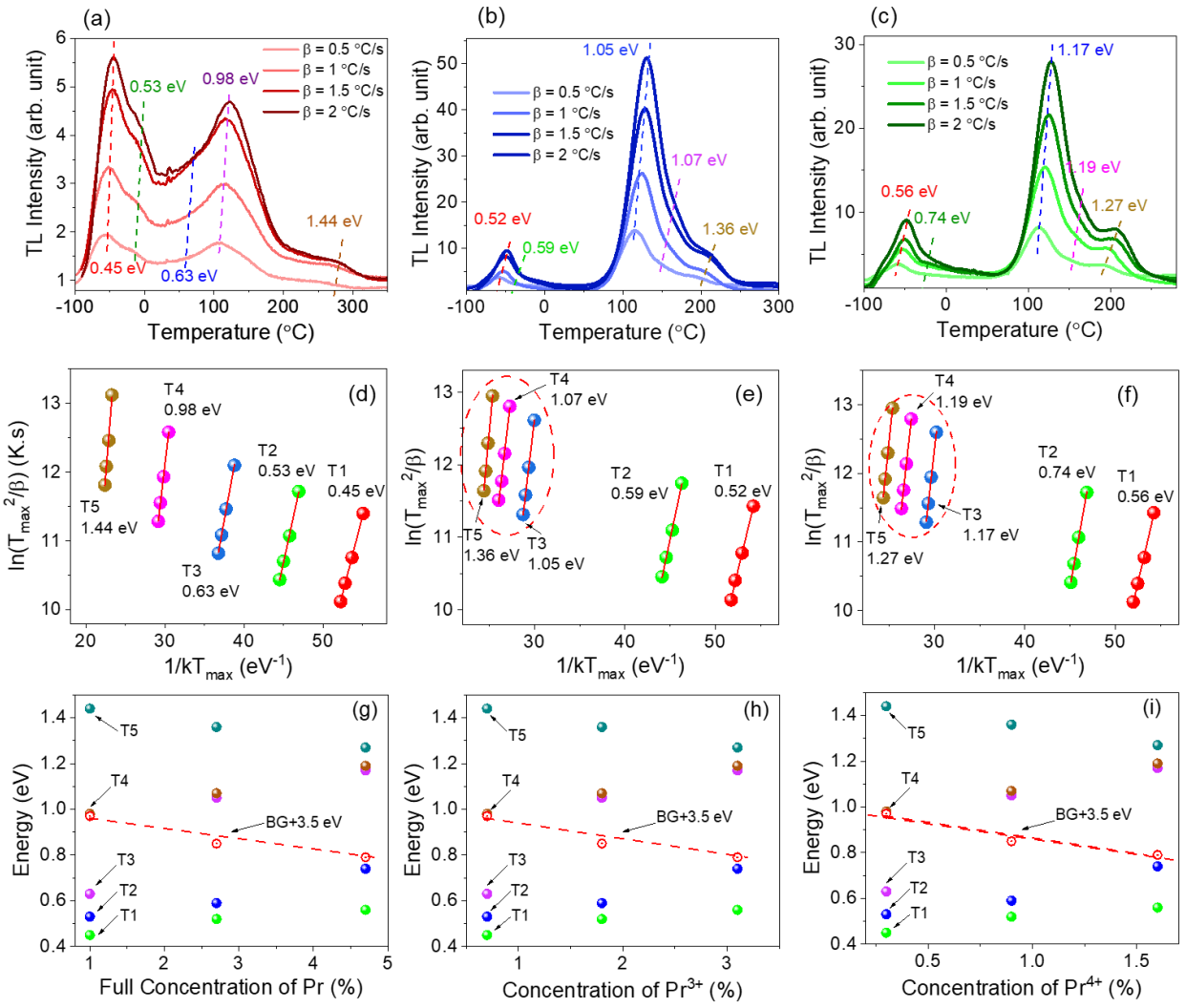

Figure 5.2.3.1: Thermoluminescence spectra of (a) S1, (b) S2, and (c) S3 samples measured at heating rates of 0.5, 1, 1.5, 2 °C/s. $ln\left(\frac{T_{max}^2}{\beta}\right)$ *as a function of* $(kT_{max})^{-1}$ *for the estimation of energy depth of each trap for (d) S1, (e) S2 and (f) S3 samples. Activation energy of different traps presented in S1, S2 and S3 as a function of (g) full concentration of Pr, (h) concentration of* Pr^{3+} *and (i) concentration of* Pr^{4+} *with band gap energy curve.*

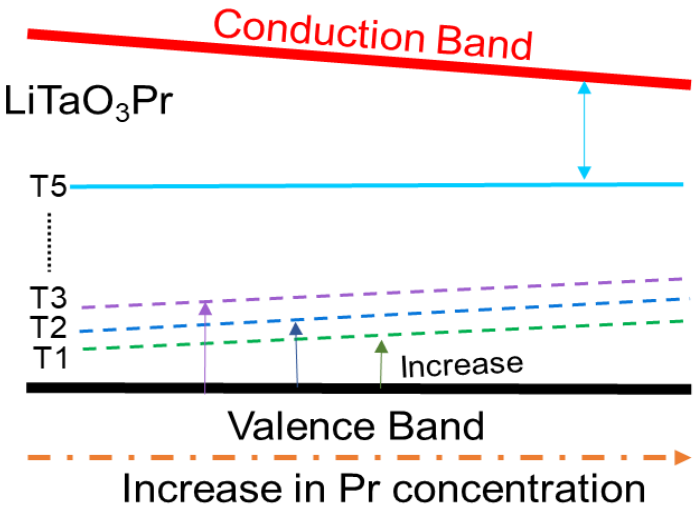

Figure 5.2.3.2: Schematic representation of tentative model of activation energies of various energy traps in $LiTaO_3$:Pr samples.

The results of TL can be affected by the temperature antiquenching behaviour of the photoluminescence, described in detail in the next chapter. The effect is observed in the region of temperatures between 100 ^oC and 220 ^oC, so it can affect the traps which appear in the glow curves in this region, probably slightly increasing the estimated values of their trapping depths. The extracted activation energy values for each trap, along with the estimated errors and s-factors for each sample, are summarized in Tables 5.2.3.1, 5.2.3.2, and 5.2.3.3.

Trap no.	E (eV)	ΔE (eV)	s-factor (s^{-1})	Δs (s^{-1})
1	0.45	0.01	2.9 E+09	0.9 E+09
2	0.53	0.01	2.9 E+09	1.7 E+09
3	0.63	0.01	1.5 E+09	0.7 E+09
4	0.98	0.01	4.2 E+11	2.2 E+11
5	1.44	0.09	1.3 E+13	2.9 E+13

Table 5.2.3.1: The estimated values of activation energies and s-factors of different energy traps presented in S1 samples.

Trap no.	E (eV)	ΔE (eV)	s-factor (s^{-1})	Δs (s^{-1})
1	0.52	0.01	1.1 E+11	0.6 E+11
2	0.59	0.01	3.6 E+10	1.4 E+10
3	1.05	0.01	2.1 E+12	0.2 E+12
4	1.07	0.06	1.5 E+11	2.5 E+11
5	1.36	0.02	3.4 E+13	2.2 E+13

Table 5.2.3.2: The estimated values of activation energies and s-factors of different energy traps presented in S2 samples.

Trap no.	E (eV)	ΔE (eV)	s-factor (s^{-1})	Δs (s^{-1})
1	0.56	0.02	1.7 E+12	1.2 E+12
2	0.74	0.01	8.7 E+13	3.6 E+13
3	1.17	0.02	1.2 E+14	0.7 E+14
4	1.19	0.01	6.5 E+12	2.8 E+12
5	1.27	0.01	3.6 E+12	1.4 E+12

Table 5.2.3.3: The estimated values of activation energies and s-factors of different energy traps presented in S3 samples.

CHAPTER 6. Thermal Anti-Quenching Properties of $LiTaO_3$:Pr

The thermal quenching analysis of $LiTaO_3$:Pr samples reveals that this material exhibits thermal anti-quenching behavior (prominent at temperatures range 373–523 K). A literature review highlights that such properties hold significant potential for applications in luminescence thermometry. Luminescence thermometry is a technique used to measure temperature based on the luminescent properties of phosphor materials, tailored to specific applications. The concept of temperature measurement using luminescence thermometry dates back to a 1937 patent, originally filed in 1932 by Paul Neubert [150, 151]. The patent identified the thermal sensitivity of certain luminescent materials, with zinc sulfide doped with copper cited as an example of luminous paint. The specified sensing temperature range for this material was between 300 °C and 500 °C. Over time, the field has witnessed exponential growth in related publications and citations, as illustrated in Figure 6.1 [152]. Luminescence thermometry typically estimates temperature by evaluating specific parameters of the emitting center, including (see Figure 6.2):

i) **Spectral characteristics**, such as shifts, band shape, or bandwidth of a given transition,
ii) **Emission intensity**, either integrated or peak, for a single transition or a pair of transitions,
iii) **Lifetime measurements**, based on the time-decay profiles of luminescence from excited states.

This growing field highlights the versatility of thermal anti-quenching materials like $LiTaO_3$:Pr in advanced temperature-sensing applications.

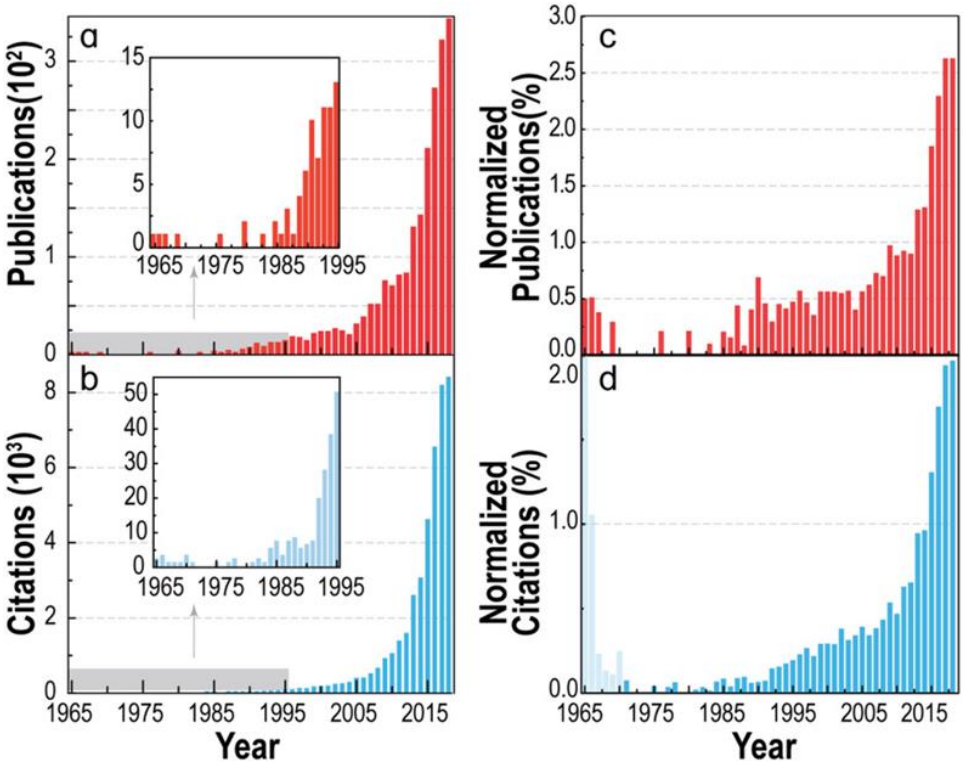

Figure 6.1: Displays the growth in the field of luminescence-based thermometry through the analysis of (a) the number of publications and (b) their citations. (c) and (d) show the

normalized data. The data is derived from a Web of Science (Clarivate Analytics) search conducted on 20/10/2018 in the principal collection (1900–2017). Reproduced from Ref. [152].

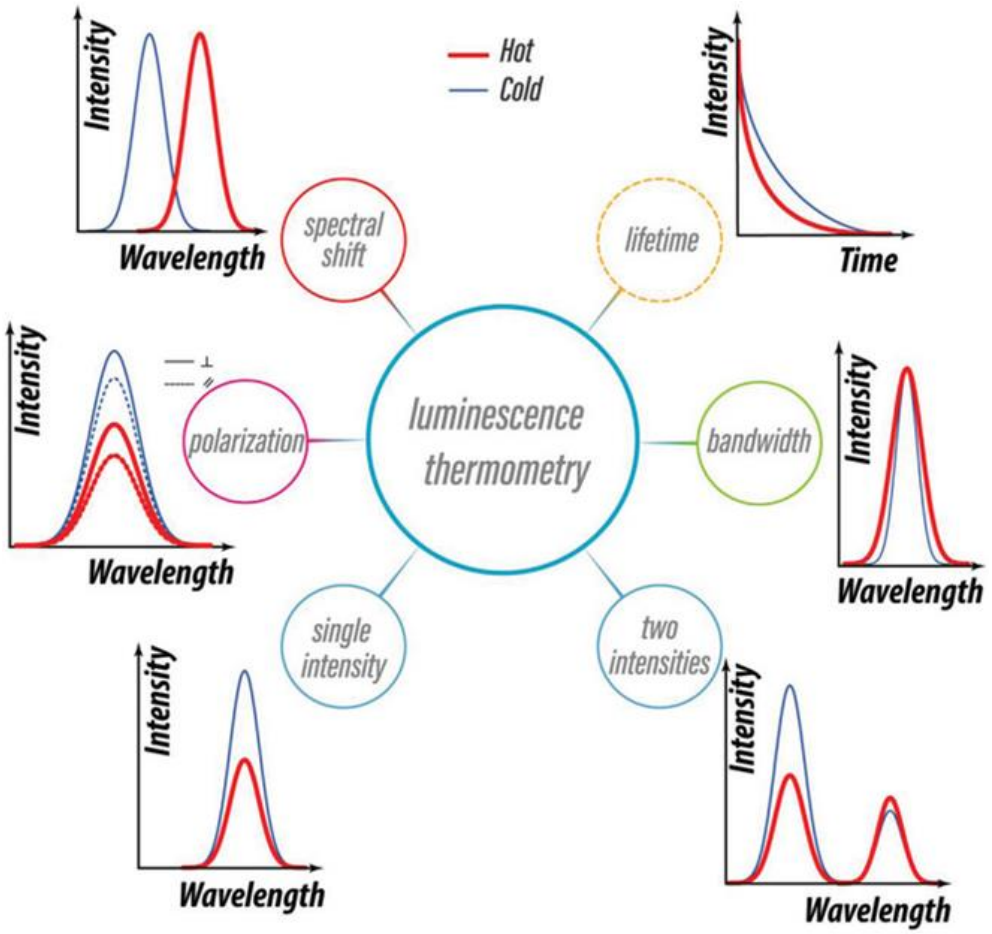

Figure 6.2: A schematic representation of the potential effects of increasing temperature on the emission characteristics of luminescence material. Reproduced from Ref. [152].

6.1. Intensity Ratio for Luminescence Thermometry:

The most common form of luminescence thermometry involves the luminescence intensity ratio (R) of thermally coupled excited states, which has been extensively studied. This technique offers several advantages, including accuracy, precision, and non-invasiveness, enabling temperature measurements with high spatial and temperature resolution. Additionally, it allows for remote temperature monitoring. This approach is known as Boltzmann-type luminescence intensity ratio thermometry. As per the Boltzmann distribution, thermally coupled excited states are populated accordingly, and the ratio of emission intensities from these states can be described by an equation 6.1.1 [153].

$$R = \frac{I_{E2}}{I_{E1}} = B \cdot \exp\left(\frac{-\Delta E}{kT}\right) \quad (6.1.1)$$

- I_{E1} is the intensity of the emission associated form one excited energy level,
- I_{E2} is the intensity of the emission associated form second excited energy level,
- B is the constant value,

- ΔE is the energy difference between excited states,
- k is the Boltzmann constant,
- T is the temperature.

Luminescence thermometry does not directly provide the temperature value; instead, it offers an indicator (R), which could represent a ratio of emission intensities, luminescence lifetime, or a shift in the emission band. To evaluate the performance of a material for luminescence thermometry, several important parameters are considered. These include the measurement range, absolute thermal sensitivity, relative thermal sensitivity, temperature resolution, temporal resolution, and spatial resolution. [153].

The measurement range is defined as the difference between the lowest and highest temperatures that can be reliably measured by a luminescence thermometer. It depends on the luminescent and physical properties of the materials used. Additionally, the phase transitions of the host material can also influence the measurement range.

The absolute thermal sensitivity (S_a) is defined as the change in the indication (R) relative to the change in temperature (T), and it is expressed in units of the indication per kelvin (refer to equation 6.1.2) [153]. It depends solely on the degree of thermally induced variations in R.

$$S_a = \left|\frac{\mathrm{d}R}{\mathrm{dT}}\right| \tag{6.1.2}$$

However, it is not meaningful to quantitatively compare the thermal sensitivity of thermometers that operate based on different principles (e.g., optical, electrical, or mechanical) or even those using the same principle but different materials. To compare the performance of different thermometers, regardless of their operational principle or material, the relative thermal sensitivity (S_r) should be calculated [154]. The relative thermal sensitivity (S_r) is defined as the ratio of absolute thermal sensitivity to the indication value (R). This parameter was introduced by Collins et al. in 1998 and has since been widely used to compare the thermal sensitivity of various luminescent materials [155]. In 2012, Brites et al. expressed Sr in units of % change per degree of temperature change (% K^{-1}) [156]. In recent studies, scientists typically compare the S_r values of different luminescent materials used for thermometry in terms of % K^{-1}. The S_r is a continuously decreasing function of temperature, and its value depends solely on the energy difference between the thermally populated excited states.

$$S_r = \frac{1}{R} \cdot \left|\frac{\mathrm{d}R}{\mathrm{dT}}\right| \times 100\% \tag{6.1.3}$$

The temperature resolution (δT) refers to the smallest temperature change that results in a noticeable change in the indication. It depends not only on the material but also on the experimental technique. Temperature uncertainty arises from various factors, including the detection technique, acquisition conditions, and the signal-to-noise ratio. Typically, δT is estimated by analyzing the time-dependent output fluctuations of the thermometer, and observing how the temporal fluctuations in the thermometric parameter evolve. Using a calibration curve, the temperature corresponding to each R-value is determined, allowing the construction of a histogram of the temperature readouts over a specific time interval. The experimental δT is then

represented by the standard deviation of this temperature histogram. When this method cannot be implemented, an alternative estimate of the temperature uncertainty is estimated by following equation [157].

$$\delta T = \delta R \left|\frac{\mathrm{d}R}{\mathrm{dT}}\right|^{-1} \tag{6.1.4}$$

6.2. Thermal Anti-Quenching Properties of $LiTaO_3$:Pr:

To study the thermal quenching behavior of $LiTaO_3$:Pr samples, photoluminescence PL spectra were measured across a temperature range of 173 to 693 K in 20 K increments under 270 nm excitation, as shown in Figure 6.2.1. A distinct behavior was observed: the peak at 511 nm, primarily associated with the $^3P_0 \rightarrow {}^3H_4$ transition, gradually decreases as the temperature increases. Conversely, the peak at 616 nm, attributed to the $^1D_2 \rightarrow {}^3H_4$ transition, increases with rising temperature. Additionally, a nearby peak at 636 nm, linked to the $^3P_0 \rightarrow {}^3H_6$ transition, shows a similar decreasing trend with increasing temperature. This pattern is consistent across all $LiTaO_3$:Pr samples. This phenomenon can be explained by intervalence charge transfer (IVCT). When only the IVCT band is excited, electrons in the $^3P_0$ energy level of Pr^{3+} are transferred to the $^1D_2$ level via the IVCT state formed between Pr^{3+} and Nb^{5+}, enhancing the red emission associated with the $^1D_2 \rightarrow {}^3H_4$ transition of Pr^{3+}. However, simultaneous excitation of both the charge transfer band (CTB) and the IVCT band induces charge transfer from the host matrix and the $^3P_0$ level of Pr^{3+} to the $^1D_2$ level (see Figure 6.2.1 (d)) [158]. This dual excitation leads to significantly higher red emission intensities and an overall increase in total emission intensity across all samples within the 373–523 K temperature range. The eventual decline in $^1D_2$ emission intensity after reaching the maximum anti-quenching level is attributed to increased thermal energy at higher temperatures. This energy enables electrons in the $^1D_2$ level to overcome the energy barrier, facilitating non-radiative transitions and returning to the ground state. Similar thermal anti-quenching behavior has previously been reported by Chunwei Yang et al. in Pr^{3+}-doped niobate phosphors ($YNbO_4$:x%Pr^{3+}). For more details, please refer to Reference [158].

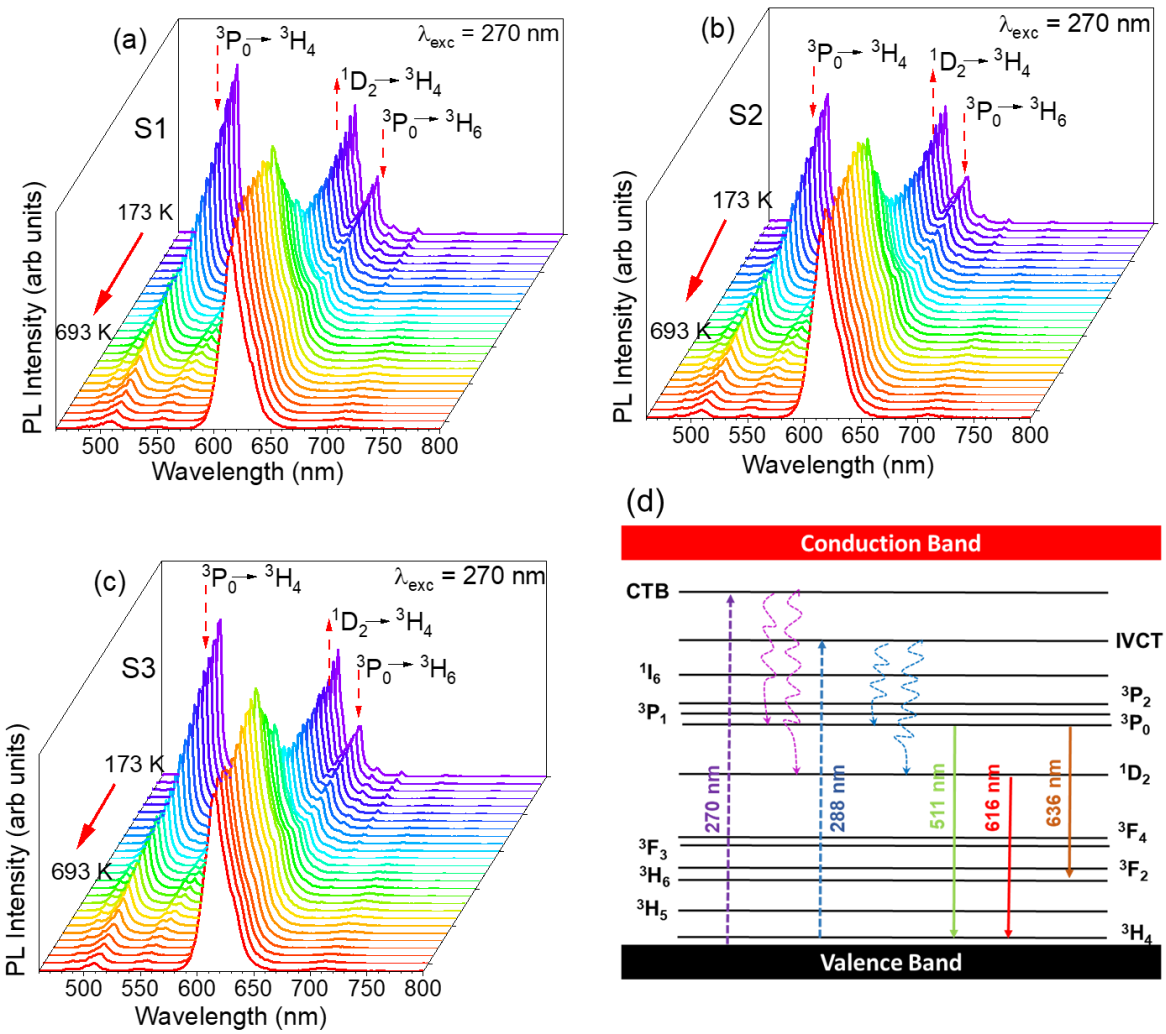

Figure 6.2.1: PL spectra at 270 nm excitation as a function of temperature from 173 to 693 K for (a) S1, (b) S2 and (c) S3. (d) The band diagram expresses the luminescence thermal quenching mechanism reconstructed from reference [158].

For better understanding, the integrated PL intensity within the 475–535 nm and 575–685 nm regions was plotted as a function of temperature for the S1, S2, and S3 samples (refer to Figure 7.2.2). For the S1 sample, it was observed that the integrated intensity in the 475–535 nm region decreased by a factor of 9, while the intensity in the 575–685 nm region increased by a factor of 2.7 as the temperature rose from 173 K to 693 K. In contrast, the S2 sample exhibited an increase in the 475–535 nm region by a factor of 8, whereas the 575–685 nm region decreased by a factor of 2.9. The S3 sample displayed a distinct behavior, with the integrated intensity decreasing by a factor of 10 in the 475–535 nm region and increasing by a factor of 2.6 in the 575–685 nm region. These variations are likely due to differences in trap formation and PL quantum efficiency across the samples. The overall pattern of total integrated PL intensity is consistent among the samples, demonstrating thermal anti-quenching behavior. From 173 K to 373 K, the intensity gradually decreases, followed by an abrupt increase between 373 K and 513 K. Beyond this range, the intensity saturates and then decreases again. The peak values of intensities at 511 nm and 616 nm were also plotted for all samples, revealing identical trends. The 511 nm peak decreases with

increasing temperature, while the 616 nm peak increases. This behavior is particularly advantageous for luminescence thermometry applications. The ratio of the different peaks as a function of temperature will be analyzed in subsequent sections, along with the calculation of key parameters essential for understanding the luminescence thermometric properties of $LiTaO_3$:Pr samples.

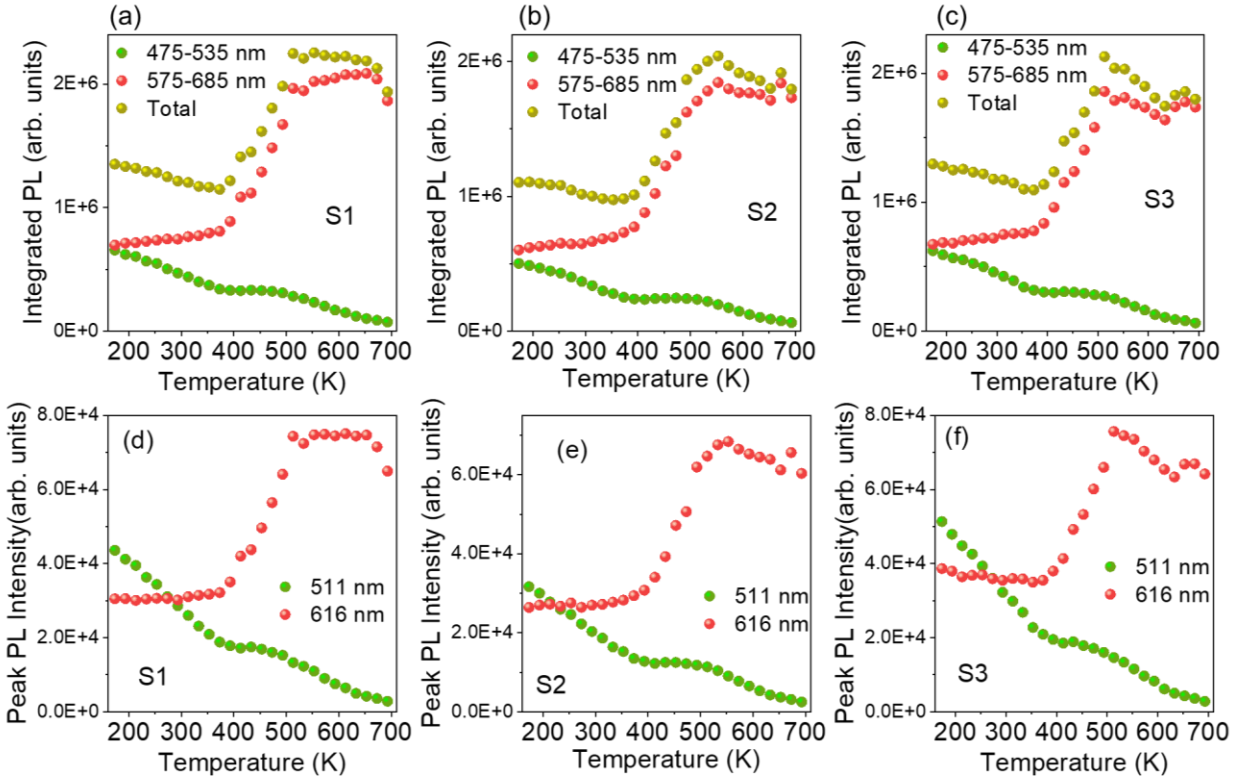

Figure 6.2.2: The integrated PL intensity of 475-535 nm and 475-685 nm regions as a function of temperature from 173 K to 693 K excited at 270 nm for (a) S1, (b) S2 and (c) S3 samples. The peak PL intensity at 511 nm and 616 nm as a function of temperature from 173 K to 693 K excited at 270 nm for (d) S1, (e) S2 and (f) S3 samples.

6.3. $LiTaO_3$:Pr based Luminescence Thermometry:

The thermal anti-quenching behavior of $LiTaO_3$:Pr samples demonstrates significant potential for luminescence thermometry applications. To explore this, the ratio of the 616 nm emission peak (associated with the $^1D_2 \rightarrow {}^3H_4$ transition) to the 511 nm emission peak (associated with the $^3P_0 \rightarrow {}^3H_6$ transition) was calculated, using both peak intensities and integrated intensities values. Figures 6.3.1 (a–c) presents the relative peak intensities as a function of temperature for each sample, along with exponential curve fitting. Additionally, the relative integrated intensities were calculated and plotted as a function of temperature in Figures 6.3.1 (d–e) for all samples. The fitting parameters for each sample are displayed as insets in the respective figures. The experimental data were fitted using equation 6.3.1 adapted from reference [159]. The equation provides an excellent fit to the experimental results, as evidenced by the coefficient of determination (R^2) values of more than 0.99 for each fitting. A key parameter derived from the fitting is C_2, which is directly proportional to the relative sensitivity of the luminescence thermometer. This parameter is crucial for evaluating the performance and precision of the

material in thermometry applications. It was observed that the C_2 values derived from relative peak intensities are higher than those obtained from relative integrated intensities. This suggests that using relative peak values is more suitable than integrated values for luminescence thermometry. This discrepancy arises because the emission peaks at 511 nm and 616 nm have adjacent peaks associated with other transitions. When calculating the integrated intensity over a spectral region, contributions from these adjacent peaks are included, reducing the C_2 values and, consequently, the thermal sensitivity of the $LiTaO_3$:Pr samples (refer to Figure 6.3.2). Moreover, the variation in the C_2 values among the samples can be attributed to other processes, such as cross-relaxation and interactions with the host lattice, which may be influenced by the differing concentrations of Pr in each sample.

$$R = \frac{I_{616\,nm}}{I_{511\,nm}} = C_1 \cdot \exp\left(\frac{-C_2}{kT}\right) \tag{6.3.1}$$

Here,

- k is the boltzman constant,
- T is the temperature,
- *C_1 and C_2 are the fitting parameters.*

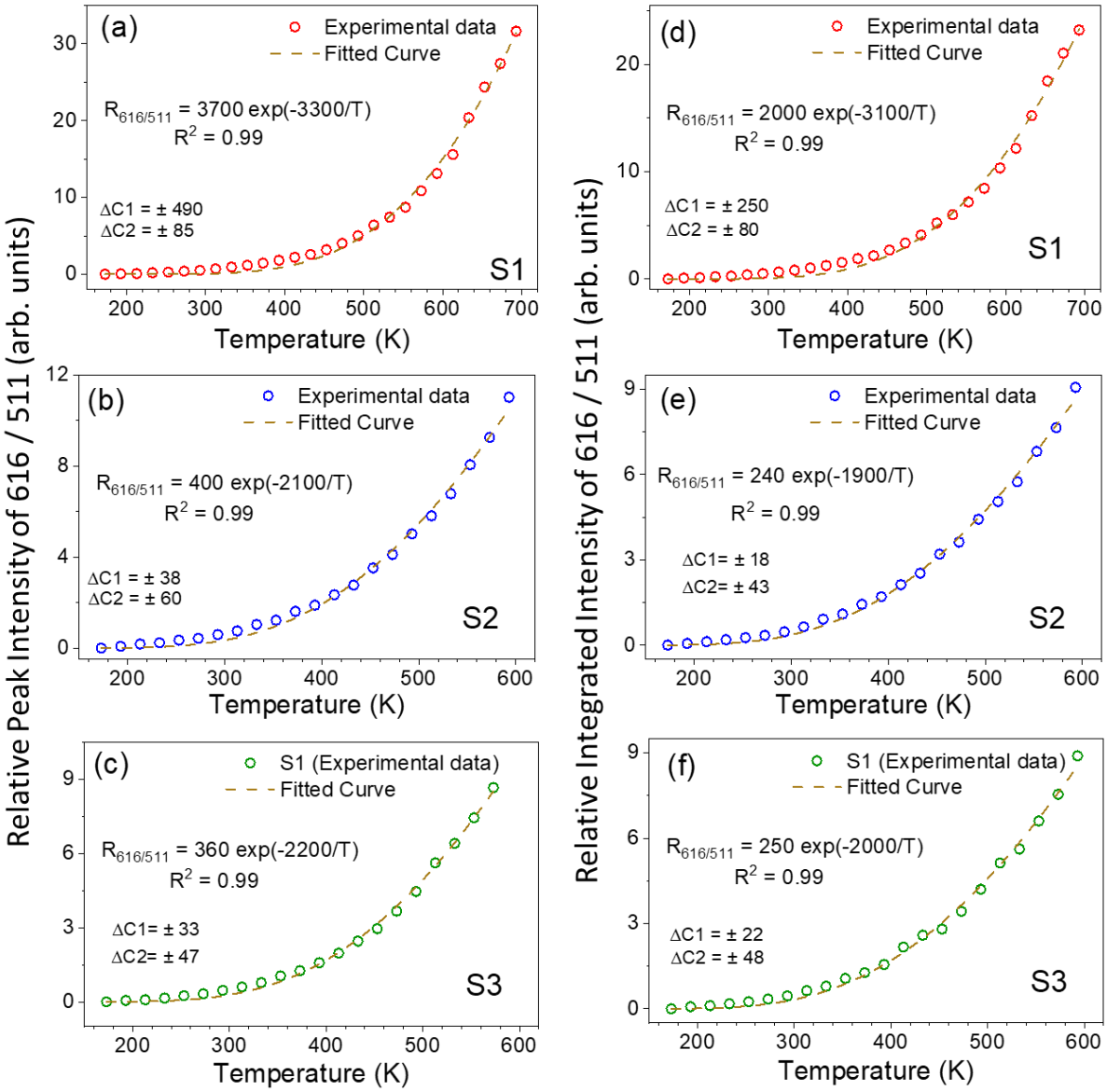

Figure 6.3.1: The relative peak intensity as a function of temperature with the exponential fitting of Eqn 6.3.1 for samples (a) S1, (b) S2 and (c) S3. The relative integrated peak intensity as a function of temperature with the exponential fitting of equation. 6.3.1 for sample (d) S1, (e) S2 and (f) S3.

As previously mentioned, certain important parameters are essential for analyzing the performance of luminescent materials in thermometry. For $LiTaO_3$:Pr samples, these parameters are also calculated. The first parameter is the relative sensitivity as a function of temperature, presented in Figure 6.3.2. The relative sensitivity is calculated using equation 6.3.2 [159]. It can be observed that the relative sensitivity of the S1 sample is the highest among the samples.

$$S_r = \left| -\frac{C_2}{T^2} \right| \cdot 100\% \qquad (6.3.2)$$

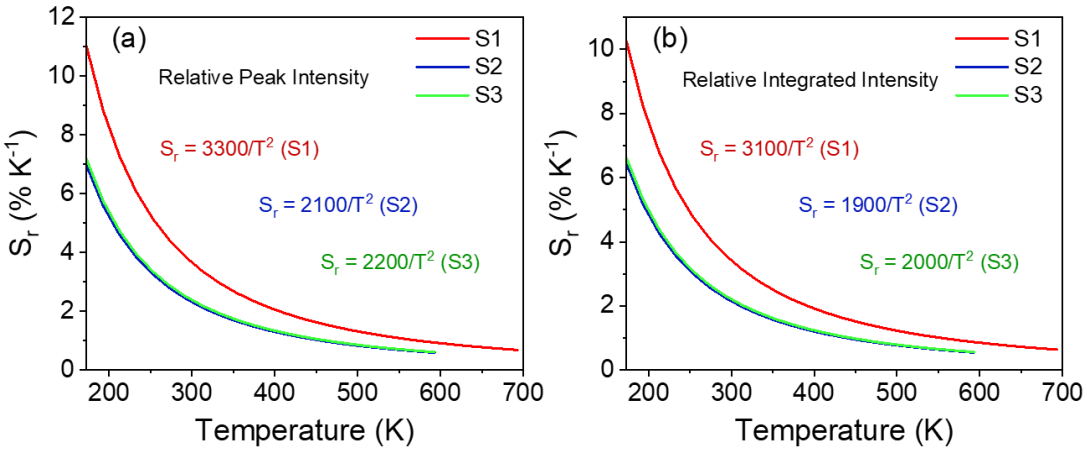

Figure 6.3.2: The relative thermal sensitivity (calculated using Eqn. 6.3.2) as a function of temperature for the S1, S2 and S3 samples calculated by fitting parameters of (a) relative peak intensity and (b) relative integrated intensity.

Another important parameter in luminescence thermometry is temperature accuracy (δT) or temperature uncertainty. Since this parameter depends not only on the sample but also on the temperature stability of the experimental setup, it is crucial to ensure that the setup's uncertainty is lower than that of the sample. The theoretical values of temperature uncertainty, estimated from the errors in the fitting parameters C_1 and C_2, are plotted in Figure 6.3.3. It can be observed that when temperature uncertainty is calculated using peak values, the S3 sample exhibits the lowest uncertainty (see Figure 6.3.3(a)). Conversely, when integrated values are considered, the S2 sample shows the lowest uncertainty (see Figure 6.3.3(b)). In both cases, the S1 sample demonstrates moderate theoretical temperature uncertainty compared to the others. Temperature accuracy can be enhanced through further optimization of the fitting parameters.

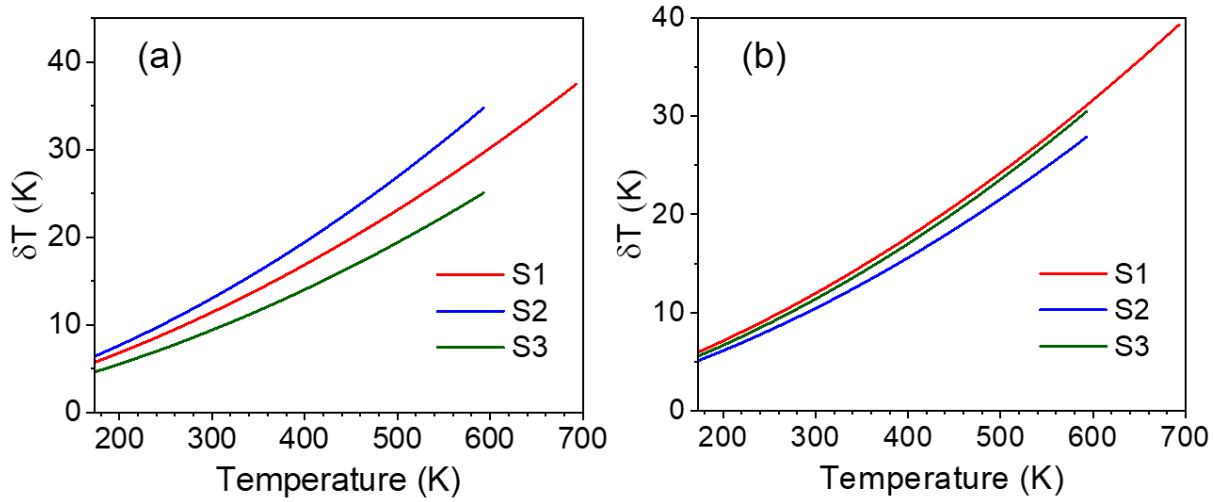

Figure 6.3.3: The theoretical values of temperature uncertainty (calculated by Eqn. 6.1.4) as a function of temperature, calculated using (a) peak values and (b) integrated values fitting for S1, S2 and S3 samples.

Since S1 exhibits a wide temperature sensing range and good relative sensitivity compared to the other samples, the experimental temperature stability values for S1 were calculated using equation 6.1.4 at specific temperatures (173 K, 300 K, 450 K, and 650 K). The results are presented in Figure 6.3.4. Figure 6.3.4(a) shows the calculated values of various parameters used to estimate temperature stability based on the relative peak values extracted from the PL emission spectra. These measurements were repeated up to 10 times at each fixed temperature. The temperature variation is 0.037 K, 0.174 K, 0.338 K, and 1.01 K for 173 K, 300 K, 450 K, and 650 K, respectively. Additionally, temperature variation was calculated using the relative integrated intensities of the 575–685 nm and 475–535 nm regions (refer to Figure 6.3.4(b)). In this case, the estimated variation values are 0.016 K, 0.048 K, 0.151 K, and 1.321 K at the same respective temperatures. It can be observed that using integrated values results in reduced temperature variation. These measurements demonstrate the thermal stability of the setups, measured using the $LiTaO_3$:Pr sample as an optical temperature sensor, rather than evaluating temperature accuracy.

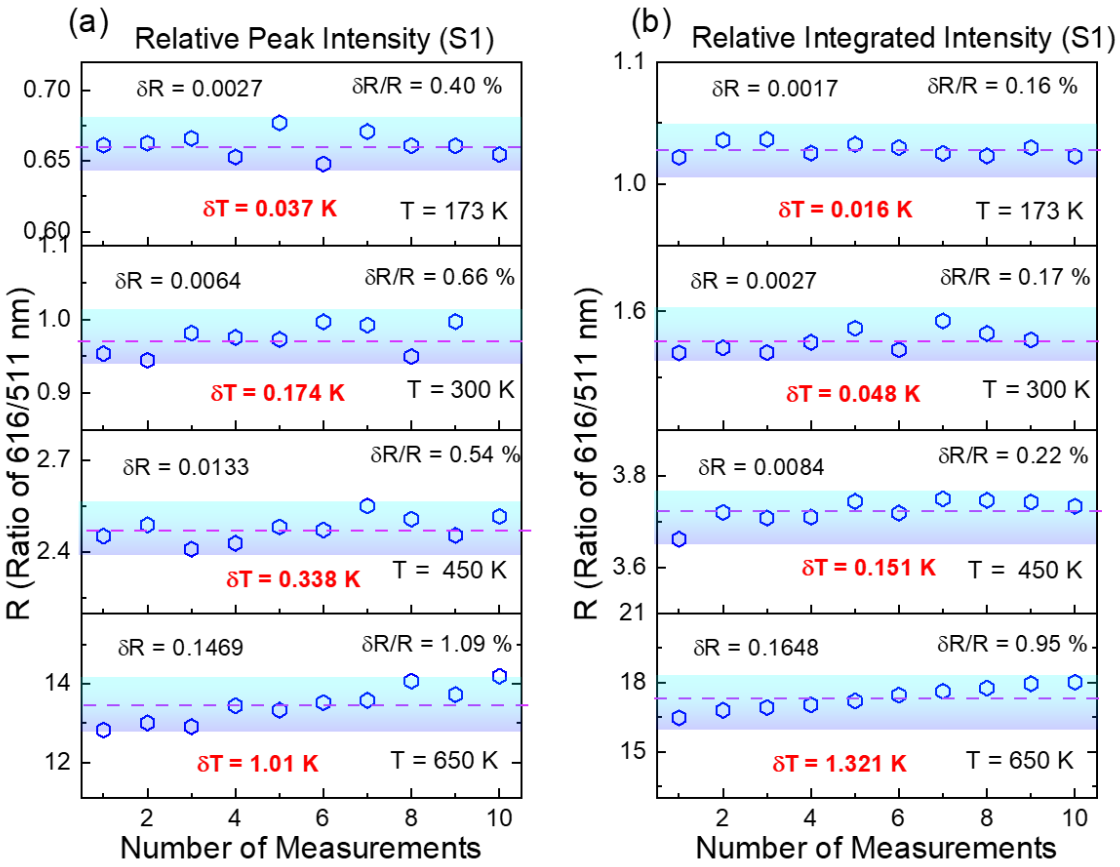

Figure 6.3.4: The temperature uncertainty at temperature values of 173 K, 300 K, 450 K and 650 K for the S1 calculated by using (a) relative peak intensity and (b) relative integrated intensity.

The extracted parameters of luminescence thermometry for $LiTaO_3$:Pr samples are compared with previously published materials known for their excellent luminescence thermometric properties, as shown in Table 6.3.1. From this comparison, it is evident that the S1 sample exhibits exceptional relative sensitivity at low temperatures and competitive sensitivity at room temperature. Moreover, it has low temperature uncertainty. Among the materials presented

in the table, only the composite $Sc_2Mo_3O_{12}$:Yb/Er and ZrO_2:Yb/Ho, studied by Lu, Y., et al., demonstrates better sensitivity at room temperature than the S1 sample. Furthermore, the S1 sample also offers a reasonably wide temperature sensing range, making it a promising candidate for luminescence thermometry applications.

Materials	Sensing range (K)	$S_{r,max}$ ($\%K^{-1}$)	T at $S_{r,max}$(K)	S_r at RT ($\%K^{-1}$)	δT at RT (K)	Peak ratio	Ref.
LaF_3:Yb,Er/LaF_3:Yb,Tm core/shell	293-323	3.9	293	2.1	~0.7	1000/1230	[160]
SrF_2:Yb,Tm/Y/Yb, Er, Nd/ Nd core/shell	293-333	~1.6	333	1.45	1.7	980/1060	[161]
$NaYF_4$: Er	113-433	2.15				837/980	[162]
Composite ($Sc_2Mo_3O_{12}$: Yb/Er and ZrO_2:Yb/Ho)	310-580	4.2	310	~4.2	~0.33	1537/1213	[159]
β-$NaYF_4$/SiO: Yb, Er	299-337	1.64	337	1.44	0.8	1010/810	[163]
YF_3: Yb,Tm	303-345	1.89	303	1.58	4.15	940/452	[164]
	303-345	1.04	303	0.93	3.89	940/650	
$LiNbO_3$: Yb,Tm	300-800	0.73	365	0.64		700/476	[165]
$NaYF_4$:Er/Yb	303-483	1.19	303	1.05		490/540	[166]
$NaGdF_4$: Yb,Er	303-373	1.9	303	0.85		654/523,542	[167]
La_2MgTiO_6:Pr	77-500	1.28	350	1.0		608/499	[168]
Sr_2GeO_4:Pr	17-600	0.9	22	~0.5	~0.45	612	[169]
$LaMg_{0.402}Nb_{0.598}O_3$: Pr	298-523	0.83	448	0.35		540/655	[160]
$LiTaO_3$:1%Pr (S1)	173-693	11.0	173	3.8	5.6	616/511	This work
$LiTaO_3$:3%Pr (S2)	173-593	6.9	173	2.4	6.4	616/511	
$LiTaO_3$:5%Pr (S3)	173-593	7.2	173	2.5	4.6	616/511	

Table 6.3.1: The comparison of various important parameters of the samples synthesized in this study with previously published work.

CHAPTER 7. Mechanoluminescence Properties of Other Materials

In this chapter, the mechanoluminescent properties of well-known luminescent materials, such as $SrSi_2O_2N_2$:Eu, $SrSi_2O_2N_2$:Eu,Mn, AlN:Mn and ZnS:Mn are discussed. Additionally, the ultrasound induced luminescence characteristics of most of them are also examined. These materials are renowned for their good luminescent properties (also observed by our group members and collaborators) and are used in a wide range of applications, including phosphor-converted light-emitting diodes (LEDs), field emission displays (FEDs), electroluminescent devices, optical imaging of biological materials, photovoltaic applications, radiation detection, and as bio-labeling agents [170-180]. A literature review reveals that these materials have not been extensively studied for their ML and Us-L properties. Therefore, investigating their ML and Us-L behaviors would be a valuable endeavor to explore their potential applications in stress and ultrasonic sensing.

7.1. Experimental:

7.1.1. Sample preparation and applied measuring techniques:

The series of oxynitridosilicate samples outlined in Table 7.1.1.1 were synthesized using a solid-state synthesis [83]. The images of the powder samples under UV is present in Figure 7.1.1.1(a). For I-ML and Us-L at 20 kHz measurements, films of equal thickness and sample portions were prepared (procedure explained in Chapter 3). For the Us-L measurements, powder embedded PDMS films were prepared by homogeneously mixing of PDMS and powder in the mass ratio of 8:2. Later, 0.1 g of hardener is added. The final mixer is poured on the plastic mold having a hexagonal shape with a maximal diameter of 3 cm. The film is dried in an oven at 60 °C for 24 hours. The films are presented in Figures 7.1.1.1(b) and (c) The thickness of the films are approximately 1.5 mm.

Sample symbol	Chemical formula	Dopant concentration	
		Eu [mol %]	Mn [mol %]
E2	$Sr_{0.98}Eu_{0.02}Si_2O_2N_2$	2	0
E4	$Sr_{0.96}Eu_{0.04}Si_2O_2N_2$	4	0
EM2	$Sr_{0.96}Eu_{0.02}Mn_{0.02}Si_2O_2N_2$	2	2
M2	$Sr_{0.98}Mn_{0.02}Si_2O_2N_2$	0	2

Table 7.1.1.1: The information regarding the concentration of dopant and sample name.

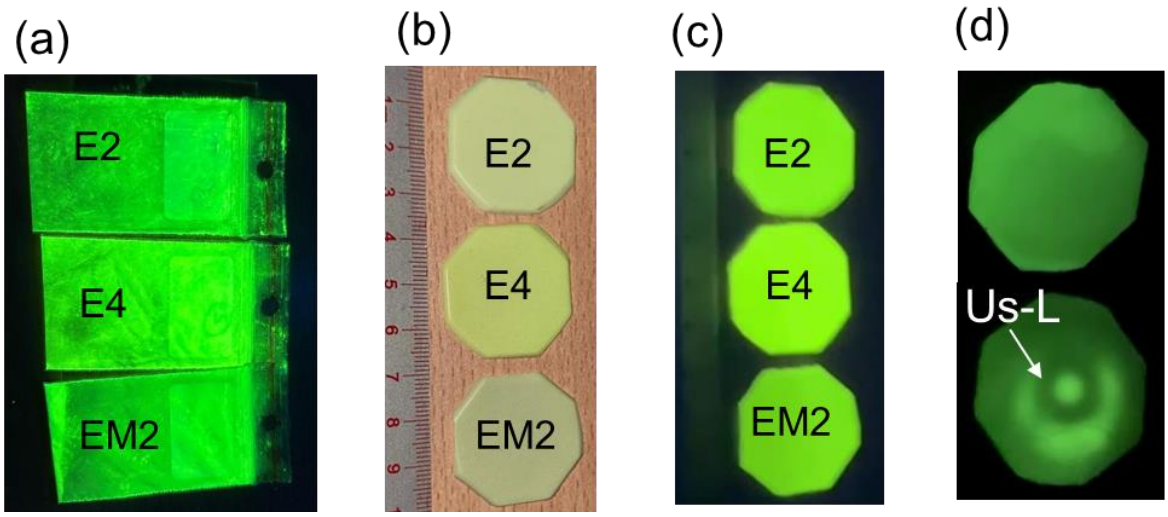

Figure 7.1.1.1: Photographs of sample E2, E4 and EM2 (a) powder form under UV light, (b) powder embedded in PDMS film, (c) powder embedded with PDMS film under UV light, and (d) E2/PDMS composite film without and with Us exposure, present Us-L.

The synthesis of the AlN:Mn sample was described in detail in reference [181]. For I-ML studies, an even layer of AlN:Mn powder was prepared by UV transparent PP adhesive tape. For the Us-L measurements, AlN:Mn embedded PDMS film was prepared by homogeneously mixing of 0.5 g PDMS and 0.05 g AlN:Mn powder. Later, 0.06 g of hardener is added. The thickness of the film is 0.8 mm.

The synthesis procedure of the ZnS:Mn nanophosphor sample was described in detail in reference [182]. For I-ML studies, a similar procedure is used mentioned in Chapter 3, an even layer of ZnS:Mn nanophosphor powder was prepared by UV transparent PP adhesive tape. The I-ML and Us-L properties of these materials were evaluated by using self-designed experimental setups described in Chapter 3.

7.2. Results and discussion:

7.2.1. Mechanoluminescence analysis:

Figure 7.2.1.1 shows the results of the I-ML studies of single doped $SrSi_2O_2N_2$:Eu and Mn co-doped $SrSi_2O_2N_2$:Eu samples mentioned in Table 7.1.1.1. In these experiments, the UV excitation time was fixed at 2 minutes, and the speed of the fired projectile was (40.7 ± 0.2) m/s and mass 0.28 g. The I-ML curves measured after the UV exposure for samples E2, E4, and EM2 are displayed in Figures 7.2.1.1(a) - (c), respectively. The sharp peaks in the signals represent the I-ML intensity captured during the collision of the projectile with the samples. All three samples demonstrated good ML reproducibility up to 5 minutes after UV excitation. To compare the ML capabilities of E2, E4 and EM2 samples, we plotted the peak and total ML intensities (calculated as the integrated ML signal intensity over time) as a function of time after UV irradiation step in Figures 7.2.1.1(d) and (e). Among the three tested samples, E2 exhibited the highest values for both peak and total ML intensities, whereas sample EM2 showed a lower peak I-ML but higher total I-ML compared to sample E4. Generally, all tested samples exhibited excellent ML capabilities, with sample E2 demonstrating the strongest response to mechanical stimuli. The high

ML intensity of E2 is attributed to its greater abundance of trap states compared to samples E4 and EM2, as identified in TL study [83]. In contrast, the better ML performance of sample EM2 over E4 is due to variations in the distribution of trapping states between the two samples.

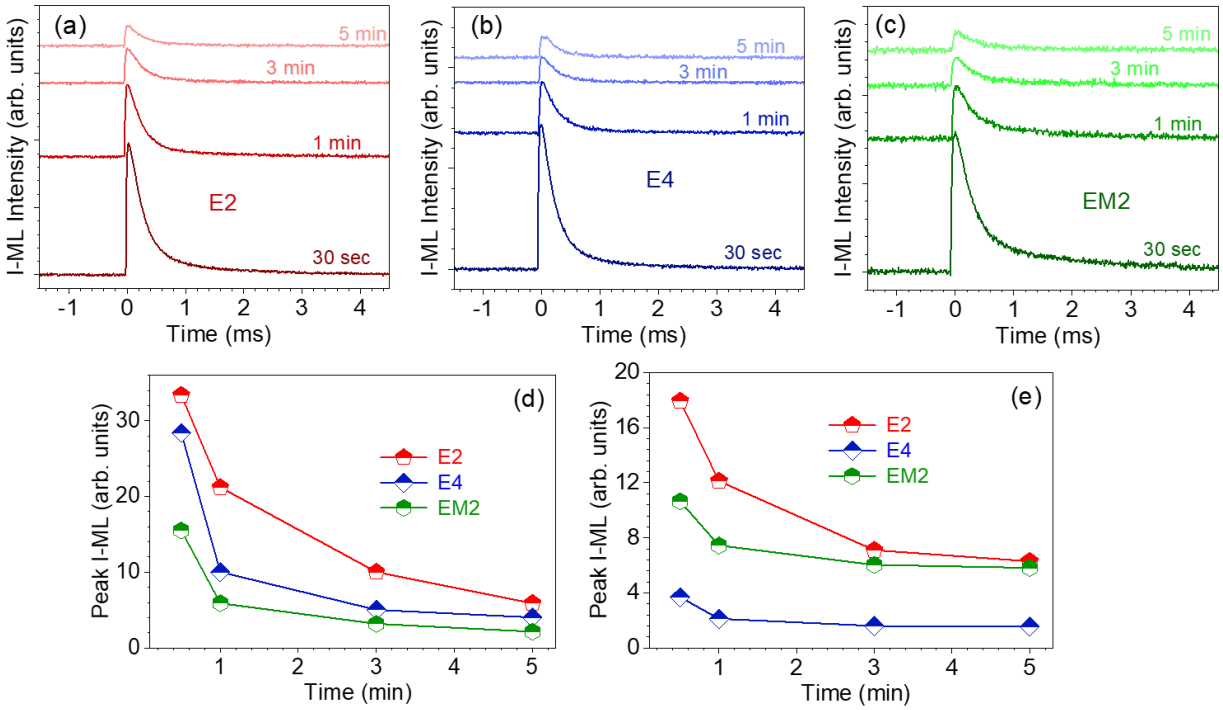

Figures 7.2.1.1: I-ML signal as a function of time measured during the firing of 0.28 g mass projectile with the speed of (40.7 ± 0.2) m/s at a film of (a) E2, (b) E4 and (c) EM2 samples at different interval after 2 min UV excitation (270 nm). The (d) peak and (e) total I-ML intensity vs. time delay after UV excitation.

Figure 7.2.1.2 presents the I-ML results for the AlN:Mn sample, which also demonstrates good I-ML during mechanical impact. Figure 7.2.1.2(a) displays the graph of I-ML intensity as a function of time. The sharp peaks in the graph represent the ML generated by mechanical impacts on the sample due to the fired projectiles. Multiple projectiles were fired on the sample in the dark at 1, 2, 3, 5, and 9 minutes after once initial UV irradiation. The region of the collision is the same in each shot confirmed by the single spot due to the shooting on the sample film. Notably, the sample retains 57% (in comparison of I-ML intensity measured at 1st shot after 1 min) of its I-ML intensity even after 9 minutes of UV excitation and five consecutive impacts (see Figure 7.2.1.2(a)). Similarly, to investigate its long-term charge carrier trapping capabilities, the I-ML was measured after one hour and two days without any UV excitation in between. The results indicate that the AlN:Mn sample retains 30% (in comparison of I-ML intensity measured at 1st shot after 1 min) of its I-ML intensity after one hour and 20% (in comparison of I-ML intensity measured at 1st shot after 1 min) after two days (see Figure 7.2.1.2(b)). These findings confirm that AlN:Mn has effective energy traps, contributing to its remarkable mechanical impact sensing capabilities and reproducibility of I-ML. The relative I-ML intensity, shown in Figure 7.2.1.2(c), increases over time, further supporting its potential as a candidate for I-ML sensing applications, with red-colored ML at a peak wavelength of 600 nm. The results of the I-ML experiments

demonstrate that the AlN:Mn sample effectively senses mechanical impacts with high sensitivity and reproducibility.

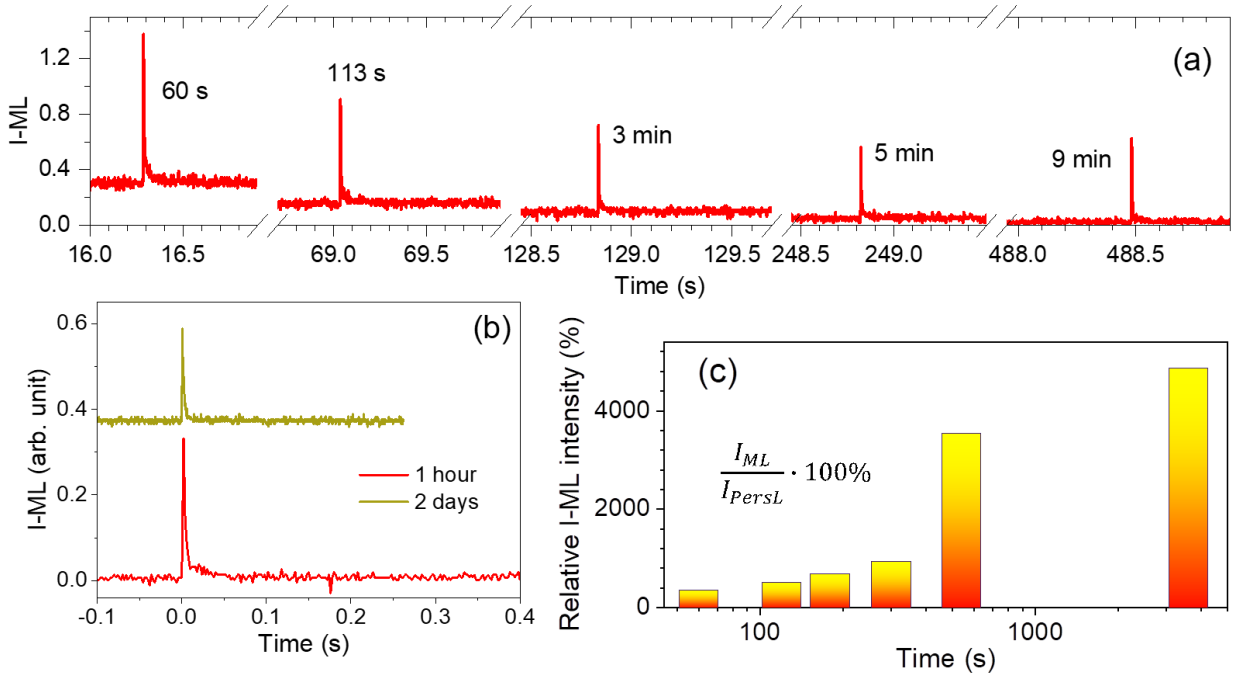

Figure 7.2.1.2: (a) The I-ML intensity as a function time after 1 min, 2 min, 3 min, 5 min and 9 min of UV exposure (270 nm and 1 min). (b) The comparison of I-ML vs. time after 1 hour and 2 days of UV excitation. (c) Bar plot represents the ratio of intensity of I-ML and PersL as a function of time.

Figures 7.2.1.3(a) and (b) display the I-ML curves for zinc blende cubic and wurtzite ZnS:Mn samples over time, both with and without pre-excitation by UV radiation. These curves, characterized by sharp peaks, represent the I-ML intensity produced during the impact of a spherical projectile with a mass of 0.28 g. In all cases, the same mass and velocity are used for the projectile to ensure comparable results. At the point of impact, a piezoelectric field forms near the activator ions, reducing the depth of the electron and hole traps around these ions. This process releases charge carriers from the traps into the conduction and valence bands [183]. The recombination of these electron-hole pairs produces non-radiative energy, which excites Mn^{2+} ions in the crystal lattice, generating ML. The color of the emission relates to the crystal structure: orange in the case of zinc blende cubic ZnS:Mn and yellow for wurtzite ZnS:Mn. For the zinc blende cubic ZnS:Mn, pre-illumination with UV light fills more electron traps, leading to enhanced recombination and, consequently, higher I-ML intensity. Notably, even without external illumination, the cubic structure exhibits a strong I-ML response. A comparative study of both the cubic and wurtzite ZnS:Mn (refer to [184-186]) structures under the same experimental conditions reveals key differences. The wurtzite ZnS:Mn sample in Figure 7.2.1.3(b) displays a more intense and slightly broader I-ML response over time compared to the zinc blende sample. This can be attributed to the higher piezoelectric coefficient of wurtzite ZnS relative to the zinc blende structure. Unlike the cubic structure, the wurtzite ZnS:Mn sample does not exhibit any improvement in I-ML performance when exposed to UV pre-illumination. Furthermore, room-temperature EPR (electron paramagnetic resonance) spectra for both samples, collected under

identical conditions (refer to [182]), indicate that the wurtzite sample contains approximately 20 times more Mn^{2+} ions than the cubic sample, which explains its significantly higher ML efficiency. Previous studies have also observed enhanced ML intensity in the wurtzite phase during temperature-induced phase transitions from zinc blende to wurtzite, further corroborating these findings [187]. These observations suggest that ZnS:Mn phosphors in both cubic and wurtzite phases are highly suitable for direct applications stress sensing applications. In the case of the zinc blende structure, ML efficiency can potentially be further improved by optimizing Mn^{2+} dopant concentration, temperature, or external illumination intensity. Additionally, both types of ZnS:Mn nanoparticles show promise for future applications when embedded in polymer matrices such as PDMS, Epoxy or PVDF [188, 189].

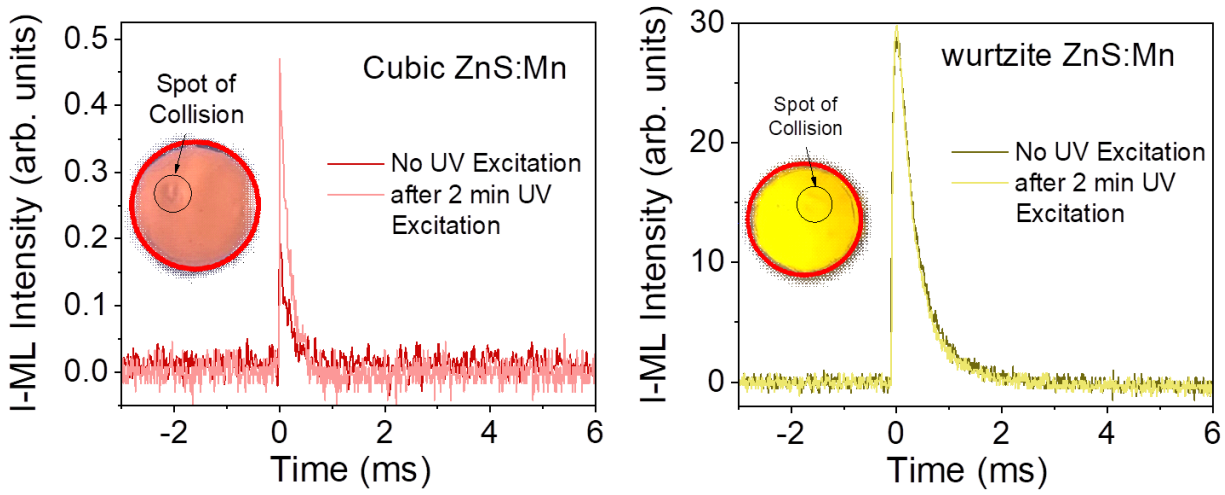

Figure 7.2.1.3: I-ML intensity as a function of time plot of (a) zinc blende cubic ZnS:Mn and (b) wurtzite ZnS:Mn samples without any pre UV excitation and with pre UV excitation for 2 minutes. Inset images shows the particular sample films under UV radiation utilized for I-ML measurements.

7.2.2. Ultrasound-induced Luminescence analysis:

Us-L analysis of the single doped $SrSi_2O_2N_2$:Eu and Mn co-doped $SrSi_2O_2N_2$:Eu samples mentioned in Table 7.1.1.1 at 20 kHz frequency are presented at Figure 7.2.2.1. The marked area in Figure 7.2.2.1(a) indicates the region where ultrasound waves at 20 kHz were applied for 2 s, causing a sharp increase in intensity and indicating Us-L. The slope of the intensity increase varies for each sample, reflecting their response behavior to ultrasound waves. Among them, sample EM2 shows the strongest response to Us waves. Figures 7.2.2.1(b) and (c) illustrate the Us-L retentivity of the samples, sensing ultrasound waves applied in 2 s cycles with an 18 s delay between each cycle. The results confirm that these samples possess excellent Us-L properties with good reproducibility at 20 kHz. The E2 and EM2 samples exhibit comparable Us-L intensities (see Figure 7.2.2.1(c)), similar to the ML results, suggesting that Us-L at 20 kHz is more closely related to ML than to TL. This hypothesis is further supported by the Us-L results of $LiTaO_3$:Pr samples already presented in Chapter 5.

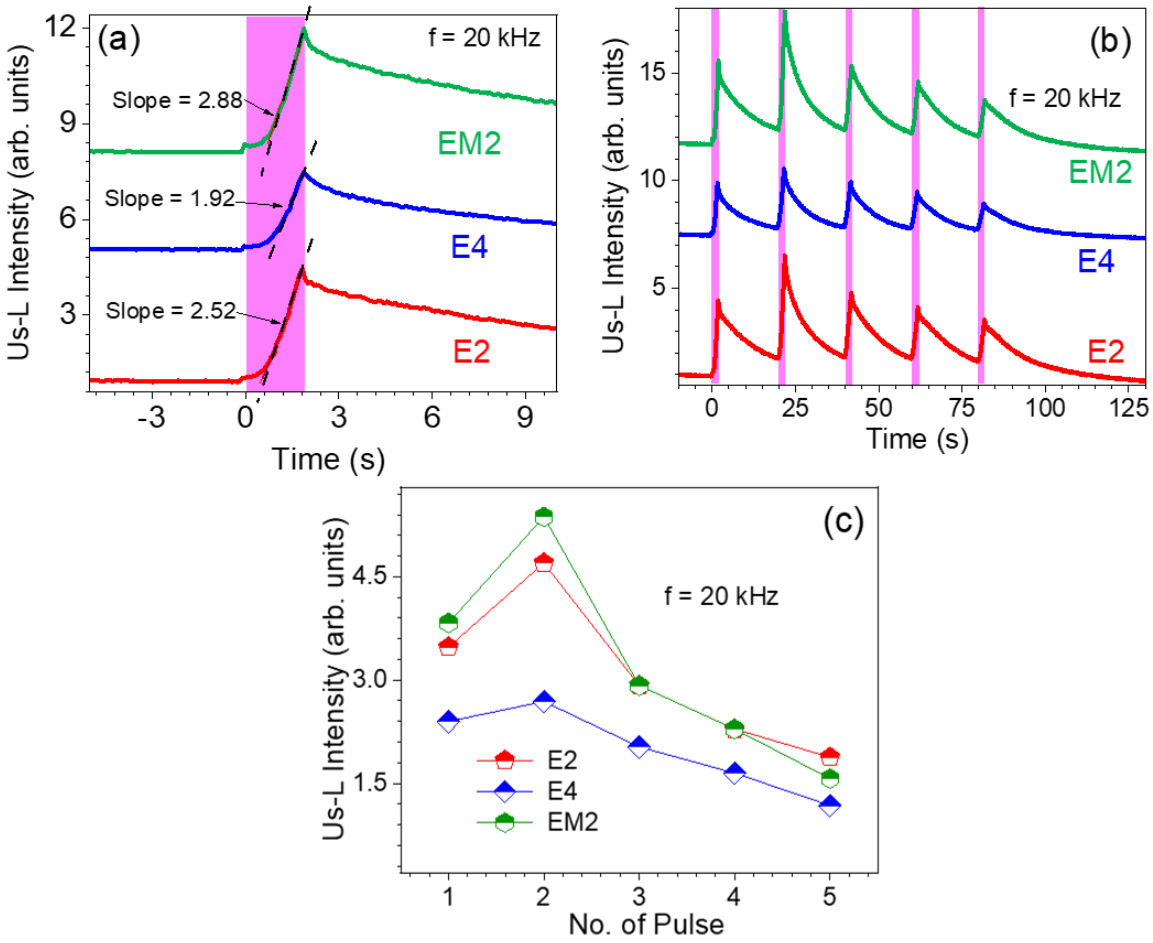

Figure 7.2.2.1 (a) Us-L curves during 2 s pulse single of Us waves (indicates with cyan color) for each sample. (b) Us-L curves during multiples 2 s Us pulses with 18 s delay time for each sample. (c) Us-L intensity as a function of number 2 s Us pulses applied on the samples.

Moreover, Us-L at 3.3 MHz is also measured and the results are presented in Figures 7.2.2.2 and 7.2.2.3. Figures 7.2.2.2(a)-(c) show a linear correlation between the generated Us-L and the power of the applied Us wave, with identical slope values across all samples. Figure 7.2.2.2(d) compares the Us-L properties of samples E2, E4, and EM2, showing that E4 has the highest Us-L value. To enhance visualization, images of the sample film during Us wave application are converted into contour plots, as displayed in the inset of Figure 7.2.2.2(d). The region of pressure induced by the Us wave is clearly visible as an area with high Us-L intensity, consistent with hydrophone Us sensing from a previous study [35, 146]. The linearity between Us-L and the power of the Us waves suggests a significant TL nature of the Us-L at 3.3 MHz. Furthermore, this finding aligns with the conclusions drawn by Michels et al., indicating that Us-L is caused by the thermal release of trapped carriers rather than being driven by ML [190].

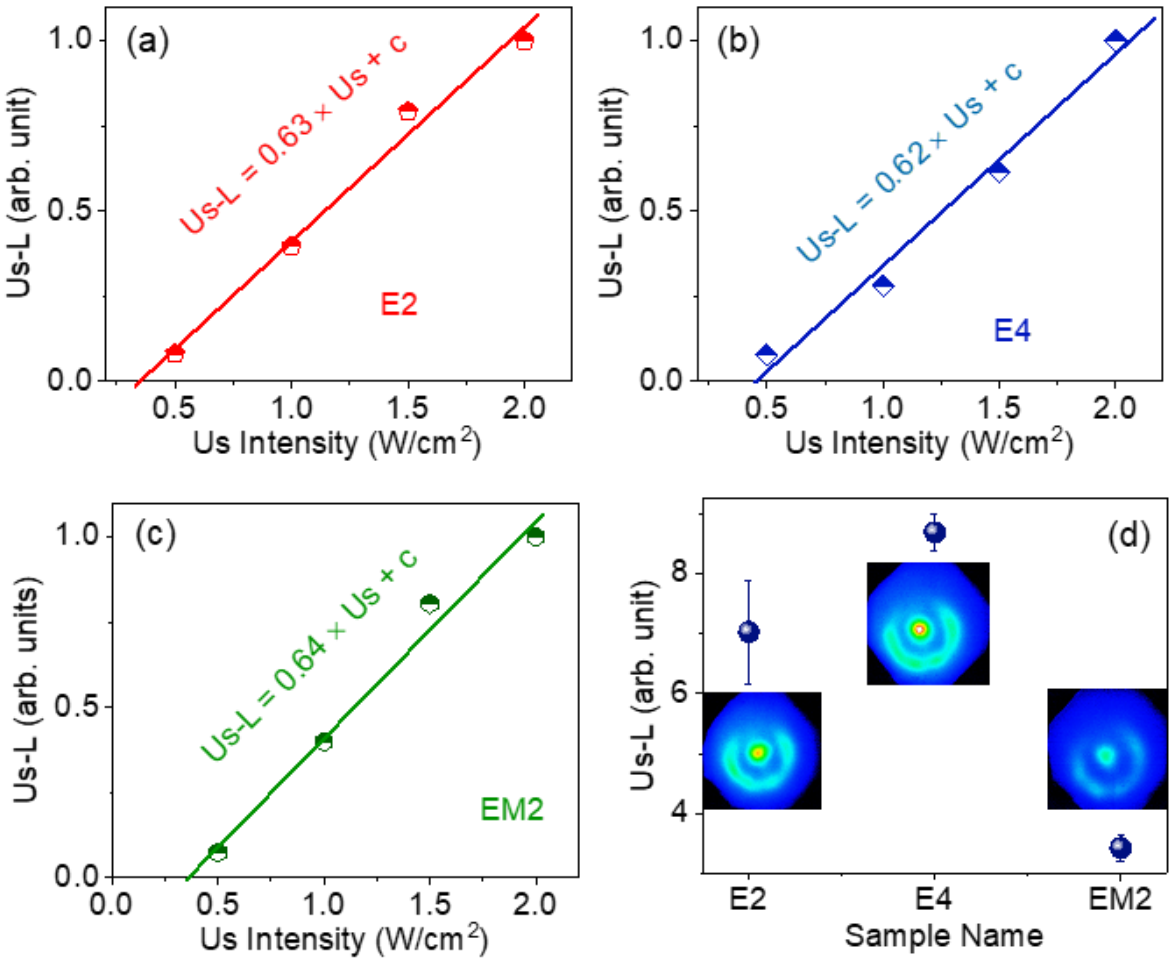

Figure 7.2.2.2: Us-L intensity as a function of Us Intensity for (a) E2, (b) E4 and (c) EM2. (d) The comparison between the Us-L intensities of E2, E4 and EM2 with an inset image of the contour plot presents the intensity due to Us exposure.

The relationship between Us-L and the distance from the Us transducer to the sample film was also examined, revealing a linear decrease in Us-L as the distance increased (Figures 7.2.2.3(a)-(c)), confirming the samples' capability to measure distance. The temperature-dependent retention of Us-L properties for E2, E4, and EM2 was further investigated at 2 °C, 20 °C, and 50 °C, as presented in Figures 7.2.2.3(d)-(f). In these graphs, all Us-L values are normalized to the initial maximum Us-L at room temperature (20 °C) for comparison. The results demonstrate that all three samples maintain good Us-L at room temperature. For E2 and EM2, the Us-L retention is better at 2 °C than at 20 °C and 50 °C. These findings confirm the Us sensing capabilities of oxynitridosilicate, highlighting a linear dependence of emitted Us-L on both Us intensity and distance. Additionally, these samples exhibit strong Us wave sensing abilities across different temperatures.

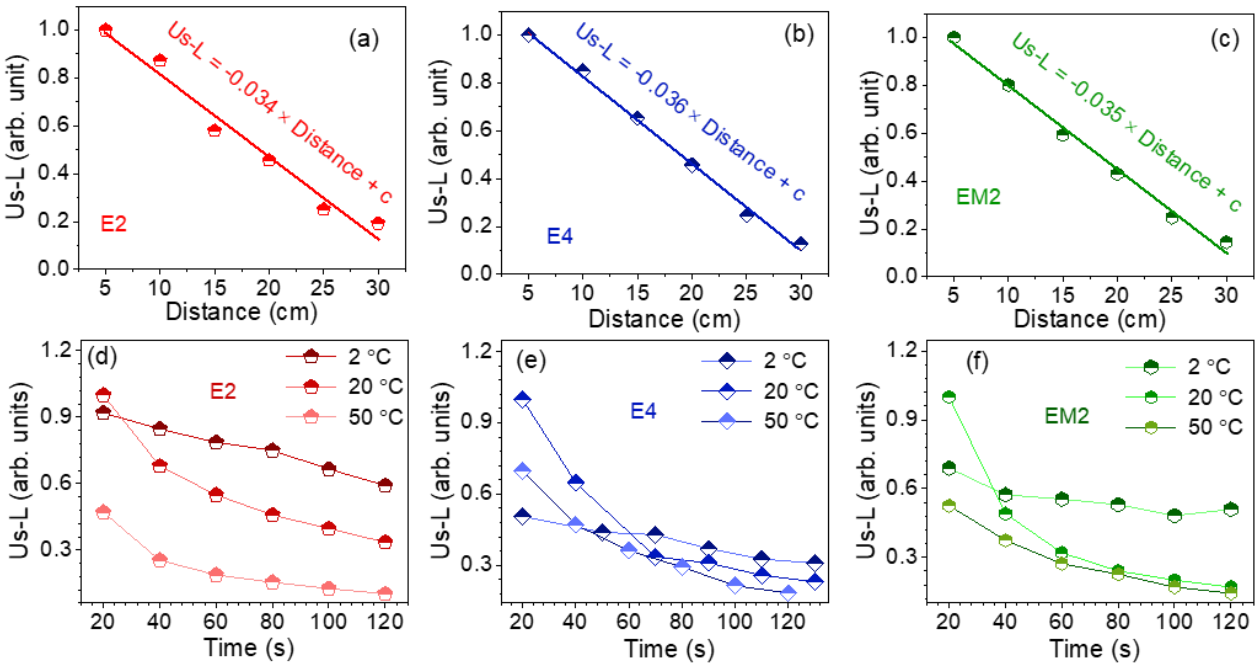

Figure 7.2.2.3: Us-L intensity as a function of the distance between the Us transducer and sample film for (a) E2, (b) E4 and (c) EM2. The Us-L as a function of time at different environmental temperatures (2 °C, 20 °C and 50 °C) for (d) E2, (e) E4 and (f) EM2.

The Us-L properties of AlN:Mn sample at a frequency of 20 kHz are illustrated in Figure 7.2.2.4, which highlights its ability to detect Us waves. Figure 7.2.2.4(a) depicts the Us-L intensity over time for different Us waves on/off time ratios in seconds (1 s/19 s, 2 s/18 s, 3 s/17 s, 4 s/16 s, 5 s/15 s, and 8 s/12 s), applied across five pulses in cycles at 24 µm vibrational amplitude. The Us-L peaks decrease with the number of pulses, and saturation of each peak occurs at higher on/off ratios and with increasing number of pulses. Figures 7.2.2.4(b) and 7.2.2.4(c) display the peak Us-L intensity and total Us-L intensity (calculated by Us-L signal intensity integrated over the time without PersL) as a function of the on-duration of each Us pulse. An abrupt increase in Us-L is observed after 2 s, followed by minor fluctuations up to 5 s, and another increase at 8 s. This nonlinear dependence of Us-L on Us pulse duration suggests that charge carriers belonging to different energy traps are being detrapped at different Us pulse duration's time. Since all peaks show the same pattern, it is not necessary to plot the peak and total Us-L intensity values for each peak up to the fifth one.

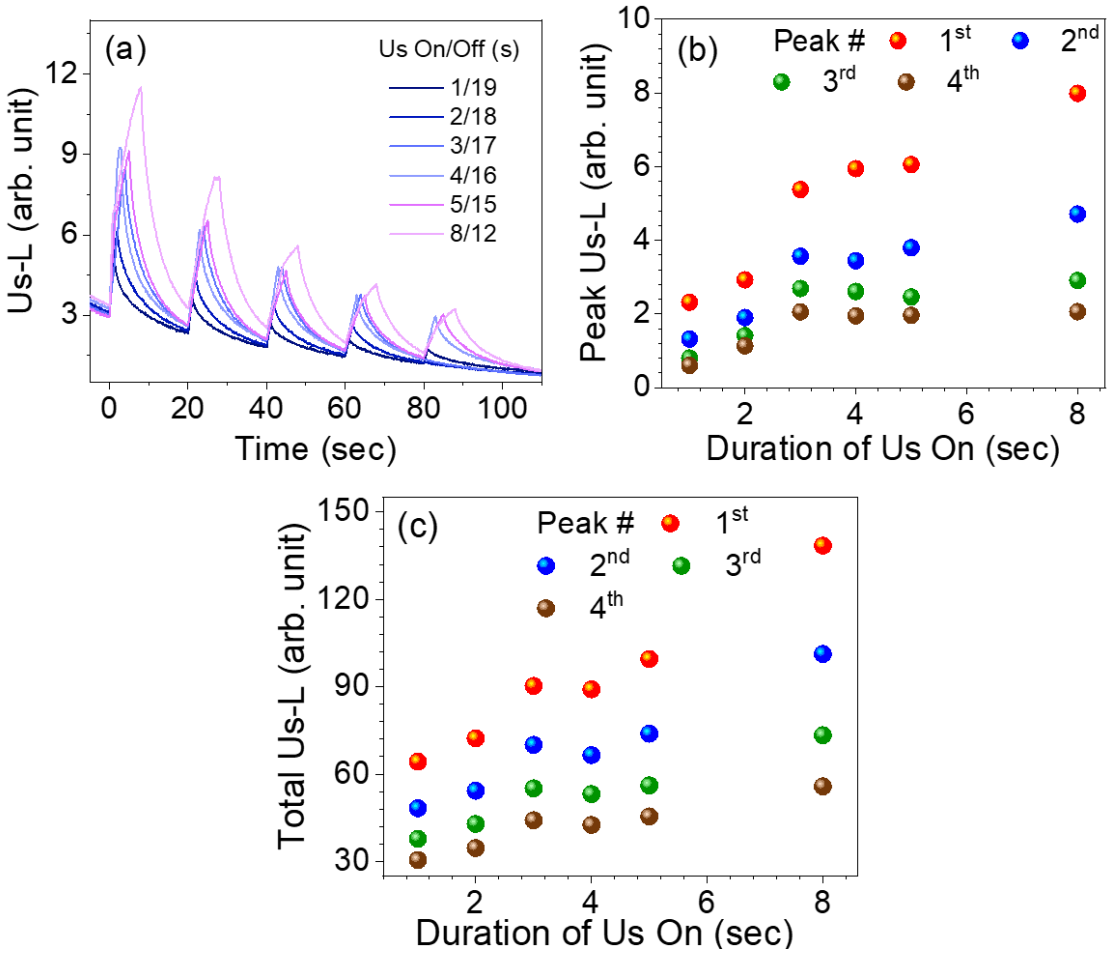

Figure 7.2.2.4: (a) Intensity of Us-L as a function of time at 24 µm vibration amplitude and different On/Off ratio in seconds 1 s/19 s, 2 s/18 s, 3 s/17 s, 4 s/16 s, 5 s/15 s and 8 s/12 s. (b) Peak Us-L values for 1st, 2nd, 3rd and 4th peak vs. duration of Us exposure. (c) Total Us-L values for 1st, 2nd, 3rd and 4th peak vs. duration of Us exposure.

Figure 7.2.2.5(a) shows Us-L intensity over time at various vibrational amplitudes ranging from 24 µm to 120 µm, changing with a step size of 12 µm. The on/off ratio time of Us waves is 1 s/19 s and the exposure repeats up to five cycles. The pre UV excitation time is 1 min with 270 nm source then after 1 min of dark, 1st Us pulse is applied. There is no UV excitation in between the cycles. The same UV excitation source, time, and delay are used in energy dependent measurements. The motivation behind the vibrational amplitude-dependent measurements is to study the effect of forces exerted on the sample during sonication. ML is caused by the detrapping of charge carriers due to the induced piezoelectric field while TL is produced as a result of thermal induced detrapping of charge carriers. So, the outcomes of these measurements will be helpful for understanding the inherent phenomena of Us-L at 20 kHz. The Us-L curves at different vibrational amplitudes indicate that Us-L intensity increases with vibrational amplitude of the transducer. To further explore the relationship between Us-L and vibrational amplitude, Figures 7.2.2.5(b) and (c) represent peak and total Us-L intensity against vibrational amplitude, respectively. It is evident that both peak and total Us-L intensities are linearly related to vibrational amplitude for each peak with different slope. The decreasing slope of the Us-L peaks with each subsequent pulse suggests that a larger number of charge carriers are already released during the initial exposure to the Us

waves. Since vibrational amplitude is directly related to force, it is likely that Us-L results from the detrapping of charge carriers due to force-induced piezoelectric fields, rather than solely from TL.

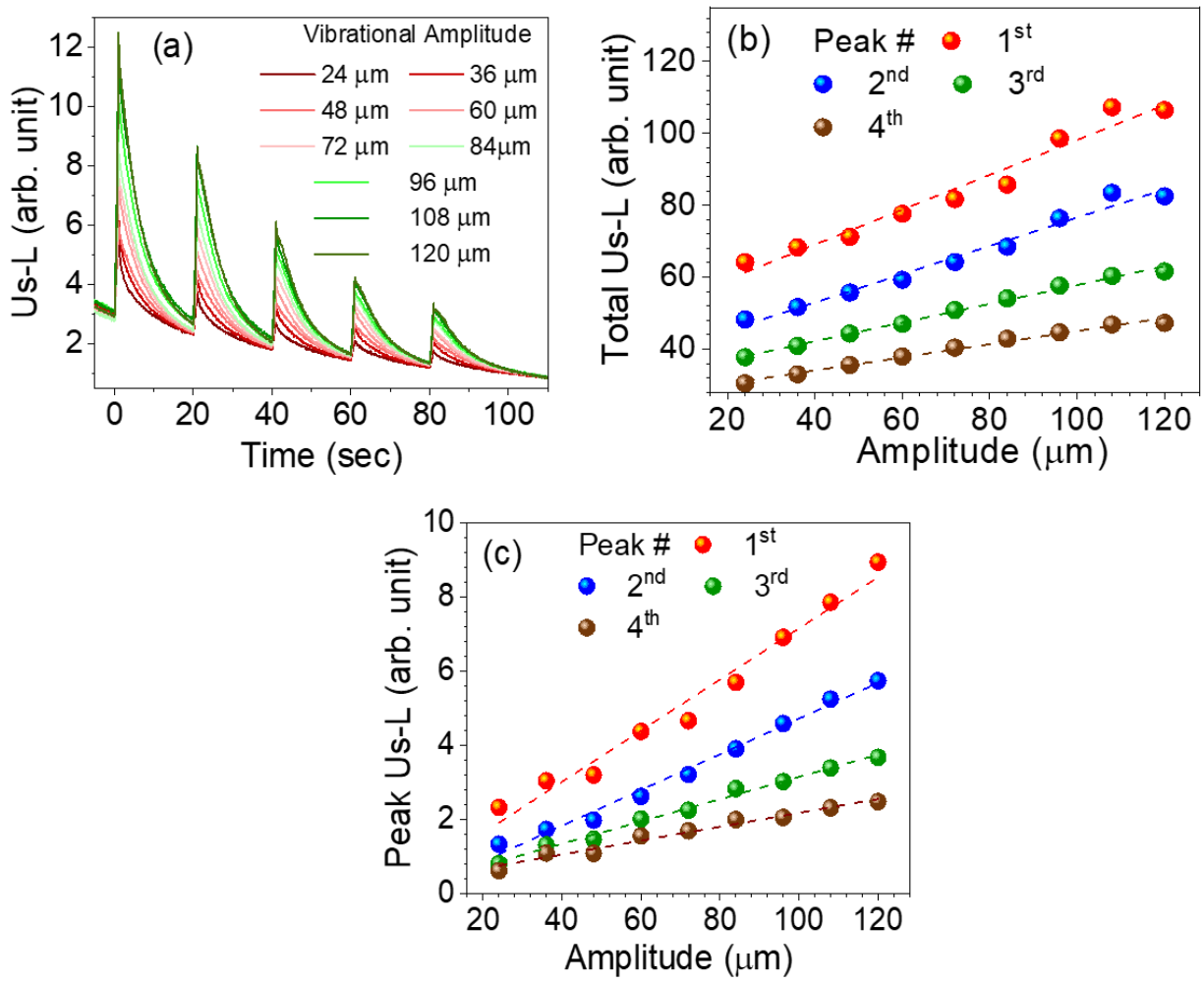

Figure 7.2.2.5: (a) Intensity of Us-L vs. time at 1 s/19 s On/Off ratio and various vibration amplitudes from 24 µm to 120 µm with a step size of 12 µm. (b) Peak Us-L values for 1st, 2nd, 3rd and 4th peak vs. amplitude of transducer vibration. (c) Total Us-L values for 1st, 2nd, 3rd and 4th peak vs. amplitude of transducer vibration.

To study the dependence of Us-L upon the magnitude of the applied Us wave's energy, we measure Us-L at various energies ranging from 1 J to 20 J at fixed vibrational amplitude (60 µm). These measurements are useful to estimate the Us-L's saturation point in terms of energy. The Us waves are applied twice with the interval of 1 min to validate the Us-L reproducibility at different energies. The extracted results are shown in Figure 7.2.2.6 (a). The results indicate that Us-L intensity is increases with the energy of the Us waves and gets saturated at higher energy values. Moreover, the second peaks of Us-L represent good retentivity at higher energies as well. Figure 7.2.2.6 (b) further clarifies this relationship, by plotting peak and total Us-L intensity as a function of energy, it exhibits a nonlinear trend and eventually saturates at higher energy levels. This behavior of Us-L with applied Us wave's energy suggests that at higher energies most of the charge carriers are already detrapped before reaching maximum energy, causing wasting of Us

wave energy and saturation of Us-L. The results validate that AlN:Mn is highly sensitive to Us waves applied at 20 kHz with even the lowest energy (1 J), making it suitable for Us sensing applications.

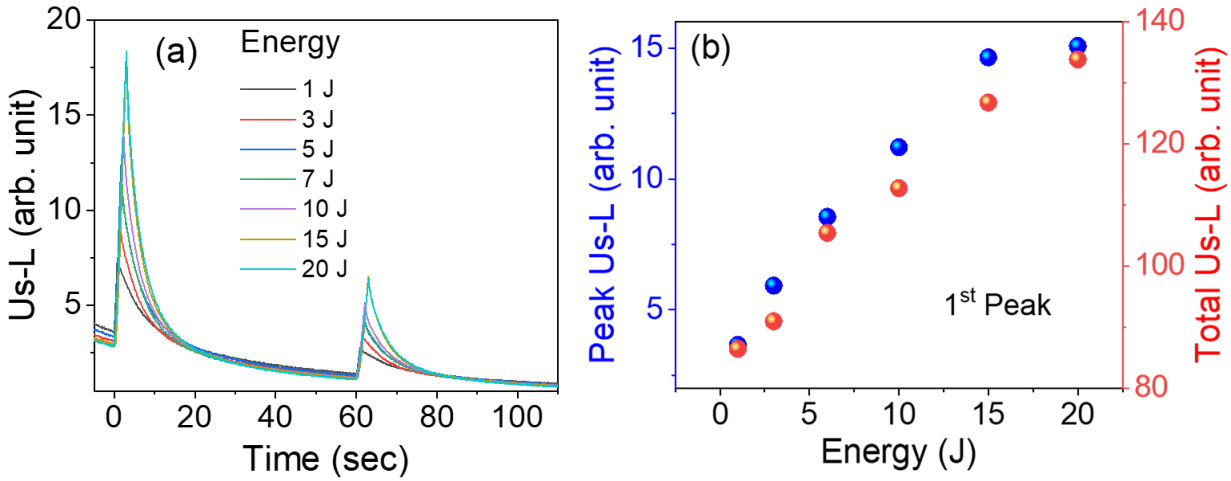

Figure 7.2.2.6: (a) Intensity of Us-L as a function of time at different energies of Us exposure from 1 J to 20 J and 60 µm vibrational amplitude. (b) Peak Us-L and Total Us-L as a function of the energy of Us exposure for 1st peak of Us-L. All graphs measured at 20 kHz frequency setup

The Us-L properties of AlN:Mn at a frequency of 3.3 MHz are presented in Figure 7.2.2.7. The results show a detectable Us-L in the capture images. When the AlN:Mn sample film is exposed to Us waves. For each value of power dependent Us-L, the sample film is pre-irradiated with UV 270 nm source for 1 min and 20 sec in the dark. Figure 7.2.2.7(a) illustrates the relationship between the power of the applied Us waves (ranging from 0.5 W/cm² to 2 W/cm²) and the emitted Us-L intensity, revealing a nonlinear increase in Us-L with increasing Us wave power. Similarly, the relationship between Us-L intensity and the distance from the Us transducer to the sample film (ranging from 5 cm to 20 cm) was examined. The sample film is UV exposure for 1 min with 270 nm diode after each step of a changing distance. The data indicate that Us-L intensity decreases linearly with increasing distance between the Us transducer and the sample film, as shown in Figure 7.2.2.7(b). To investigate the reproducibility of the Us-L, we measured the sample under the cyclic 10 s Us exposure with 10 s delay at ambient conditions. During measurements, the sample film is only once pre-irradiated with a 270 nm UV source for 1 min and wait for 20 s in the dark. The outcome is represented in the bar plot in Figure 7.2.2.7(c). The results confirmed the good Us-L reproducibility of AlN:Mn sample at 3.3 MHz, even after 100 s and four cycles. The inset contour images in Figures 7.2.2.7(a) and (b) show the captured Us-L emitted from the AlN:Mn/PDMS film during Us wave exposure. These measurements validate Us waves sensing ability of AlN:Mn sample even at 3.3 MHz frequency, making it an efficient candidate for Us wave imaging applications.

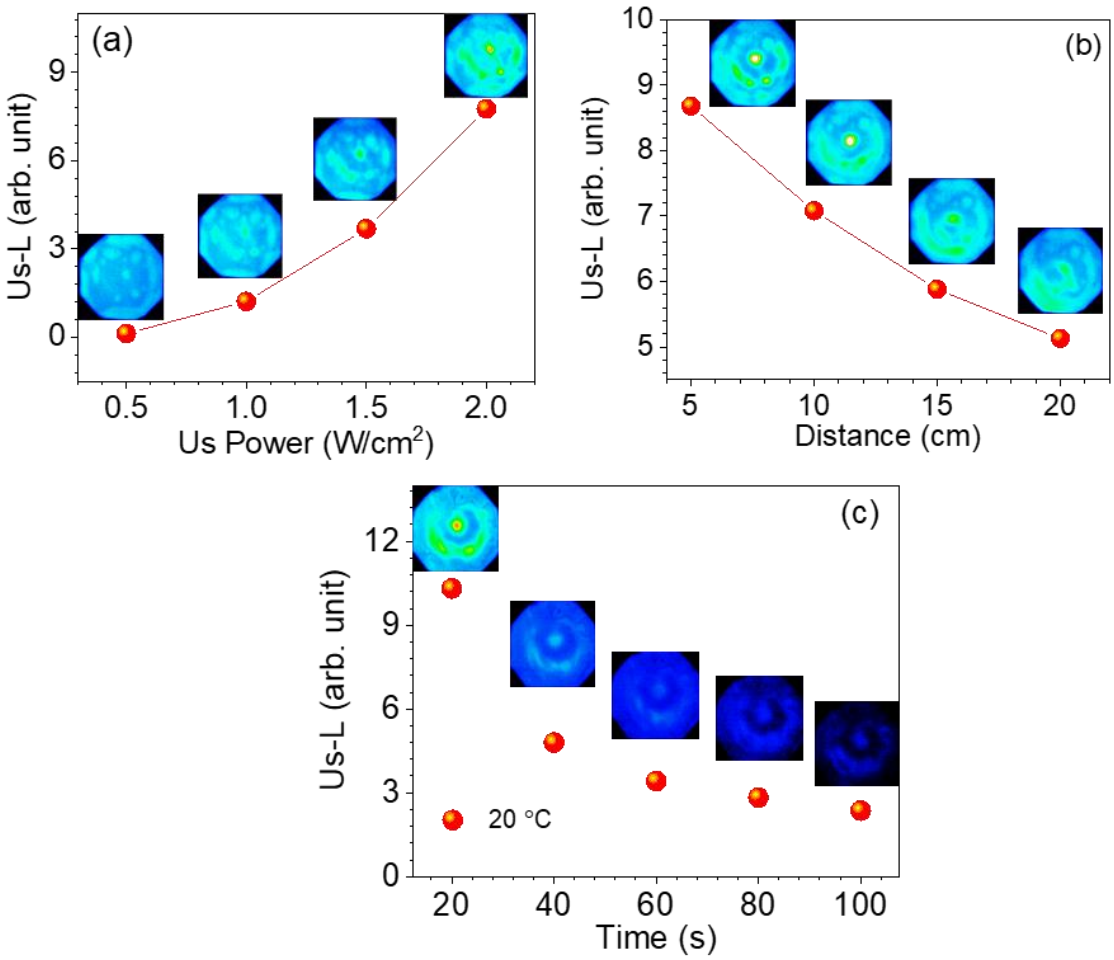

Figure 7.2.4.1: (a) the Us-L as a function of applied Us power at 3.3 MHz frequency and 3 cm distance. (b) The Us-L as a function of distance between the Us transducer and sample film at 3.3 MHz frequency and 2 W/cm^2 Us power. (c) Us-L as a function of time after the end of UV irradiation at ambient temperatures, 3.3 MHz frequency, 3 cm distance and 2 W/cm^2 Us power.

CHAPTER 8. Conclusion and Future Outlook

8.1. Conclusion:

The thesis work started by designing self-constructed experimental setups for measuring impact-induced mechanoluminescence, stress-induced mechanoluminescence, and ultrasound-induced luminescence. These setups have been carefully calibrated, and their reliability has been tested with various mechanoluminescent materials. The first setup measures I-ML as a function of impact kinetic energy with high sensitivity. This integrative, low-cost, simple, and user-friendly setup facilitates the exploration of I-ML behavior in mechanoluminescent materials, which holds significant potential for advancing impact detection technologies. The second setup is designed to visualize stress distribution within the tested specimen, where a tensile testing machine applies stress to a composite pellet made of ML material and a stress-transmitting medium. Real-time ML are captured using a high-frame-rate and high-resolution camera. This setup enables the study of stress transformation by measuring ML under varying force applications at different speeds while monitoring deformation through changes in the structure dimensions. The third setup is designed for ultrasound-induced luminescence at a frequency of 20 kHz. Its functionality is validated by measuring commercially available phosphor materials. This setup can measure pulse time-dependent, vibrational amplitude-dependent, and temperature-dependent Us-L properties of various materials.

In the second part of the thesis mechanoluminescence and ultrasound induced luminescence properties of the $LiTaO_3$:Pr are studied. Initially, three different samples, S1 (1% Pr), S2 (3% Pr), and S3 (5% Pr), having different percentages of praseodymium as a dopant are synthesized. X-ray diffraction and X-ray photoelectron spectroscopy analysis confirm that the synthesized samples have $LiTaO_3$ as a major phase with the same percentage distribution of Pr^{3+} and Pr^{4+} dopant ions. Photoluminescence results exhibit identical emission spectra for each sample associated with the Pr^{3+} ions. Mechanoluminescence analysis demonstrates that the S3 sample has significant properties of sensing abrupt mechanical impact and stress with high sensitivity and reproducibility. The prominent ML properties of S3 sample may happen due to the formation of suitable deep and shallow traps as well as relatively higher concentrations of luminescence center, beneficial for abrupt impact and stress sensing. On the other hand, S1 sample has a relatively large amount of shallow traps and a relatively small amount of deep traps results in a high efficiency of PersL. The outcomes suggested that the redistribution of trap carrier populations (deep vs. shallow traps) modulates the efficiency of ML processes. A portion of ML from $LiTaO_3$:Pr also lies in an NIR-1 biological window, which is another novel exploration of this study. The basis of ML analysis of $LiTaO_3$:Pr proves it is emerging as a highly promising material for fast, highly sensitive, and remote stress sensing applications in various engineering domains as well as a good phosphor for optical energy storage. During ultrasound induced luminescence measurement of the same samples at low (20 kHz) and high (3.3 MHz) frequency Us-L setups were performed. The outcome reveals that at 20 kHz, S1 exhibited a remarkably high intensity (~10 times higher than S2 and S3 samples), while S2 demonstrated excellent Us-L reproducibility. Conversely, S3 displayed a fast response and recovery time to ultrasound with Us-L saturation at elevated Us high-power levels. In the case of a temperature-dependent Us-L at 20 kHz study, the S1 exhibited

a linear decrease with increasing temperature, lowest at 53°C. However, S2 maintained consistent Us-L across temperatures from 12°C to 53°C. An interesting observation from the amplitude-dependent Us-L measurements at 20 kHz is the linear relationship between vibration amplitude (linearly related to force) and Us-L intensity, indicating that transducer sonication induces a piezoelectric field, resulting in the detrapping of charge carriers. The mentioned results at 20 kHz hinted towards the prominent ML nature of Us-L. However, at 3.3 MHz, S1 displayed a linear increase with increasing temperature up to 30°C, while S2 and S3 exhibited similar behavior up to 40°C, which may be because of the existence of deep traps in S2 and S3 samples. This linear increase of Us-L with temperature is in agreement with the thermoluminescence results and previously published observations by Michels et al. [35], validate that Us-L at high frequency (3.3 MHz) is produced by ultrasound wave-induced thermal energy. Moreover, the unlike acoustic phenomena at low (acoustic cavity) and high (convective acoustic streaming) frequencies may also cause a distinct prominent nature of Us-L: ML-driven (20 kHz) and ii) TL-driven (3.3 MHz). The trap system (concentration, depth) in each sample makes them suitable for diverse ultrasound sensing applications and most probably this trap system correlates with variable concentrations of Pr in $LiTaO_3$ crystal lattice. Moreover, Us-L in the infrared region offers $LiTaO_3$:Pr an opportunity to play an important role in medical applications as well. The presented study revealed the unique ultrasound sensing capabilities of $LiTaO_3$:Pr for versatile potentially industrial and medical applications. Additionally, during the analysis of thermal quenching, it was observed that the $LiTaO_3$:Pr sample exhibits thermal anti-quenching behavior, which is highly advantageous for luminescence thermometry analysis. The luminescence thermometry investigation revealed that S1 demonstrates excellent luminescence thermometric properties with a wide thermal sensing range and good relative sensitivity.

In the concluding section of the thesis, the mechanoluminescence and ultrasound-induced luminescence properties of other well-known luminescent materials, including $SrSi_2O_2N_2$:Eu, $SrSi_2O_2N_2$:Eu,Mn, AlN:Mn and ZnS:Mn, were also studied. The promising ML and Us-L studies outcomes position these materials as significant candidates for future in-depth exploration of their ML and Us-L properties. Furthermore, these results offer strong motivation for engineers and technicians to consider the commercialization of these materials for applications in stress sensing and ultrasonic imaging.

8.2. Future outlook:

During ML studies for stress sensing it can be found that an alternative approach could be considerable: rather than detecting stress through changes in intensity, monitoring changes in color could offer valuable insights and enhance the spatial resolution of stress sensing. In the proposed idea, a series of composites with different ratiometric compositions will be prepared with the three different materials that have an individual single narrow peak at blue, green and red regions, respectively. Afterward, their cylindrical pellets and films of the composite materials will be prepared by using epoxy resin or other polymers like PDMS, Epidian, etc. The correlation of change in ML color with the magnitude of applied mechanical stress will be experimentally observed and studied by capturing images and emission spectra of the pellets during variable stress or impact for each composite. Based on promising color-modulated ML properties, the ratiometric composition of the precursor materials is optimized. Moreover, the reproducibility of ML

composite material and its performance will be investigated. For the exhibition of the practical application of the project, several prototypes of mechanical impact and stress-sensing films will be prepared by employing the best ML color-modulated composites. With the completion of a proposed idea, it will be expected that a few optimized and reproducible outstanding composite materials can easily modulate their ML color with the magnitude of applied mechanical stimuli. For verification of the practical feasibility of the proposed idea, we try to prepare composite/epoxy pellets (thickness = 22 mm and diameter = 10 mm) by using three different composites having two dissimilar ML materials ($SrAl_2O_4:Eu^{2+},Dy^{3+}$ for green color emission and $Sr_{0.95}Ca_{0.05}(SO_4)$:Mn for red color). These composites are obtained by mixing different mass percentages of $SrAl_2O_4:Eu^{2+},Dy^{3+}$ (10%, 20% and 30%) into $Sr_{0.95}Ca_{0.05}(SO_4)$:Mn powder. Afterward, its pellets are prepared with a stress transmission medium (epoxy resin) with a mass ratio of 1:9 (composite/epoxy). Some initial measurements are done by utilizing an S-ML setup for exhibiting stress-dependent color modulation. The visuals of pellets as a function of time during the application of stress with the rate of 500 mm/min up to 9% deformation are exhibited in Figure 8.2.1. The pictures exhibit color modulation from red to yellow during the application of stress. The composites that have 20% and 30% $SrAl_2O_4:Eu^{2+},Dy^{3+}$ powder show good ML and color modulation because the $SrAl_2O_4:Eu^{2+},Dy^{3+}$ has good ML properties as compared to $Sr_{0.95}Ca_{0.05}(SO_4)$:Mn powder valid by previously mentioned results. This novel idea opens up new possibilities for stress detection and monitoring, as it provides another visual and intuitive way to perceive mechanical stress variations in a testing specimen.

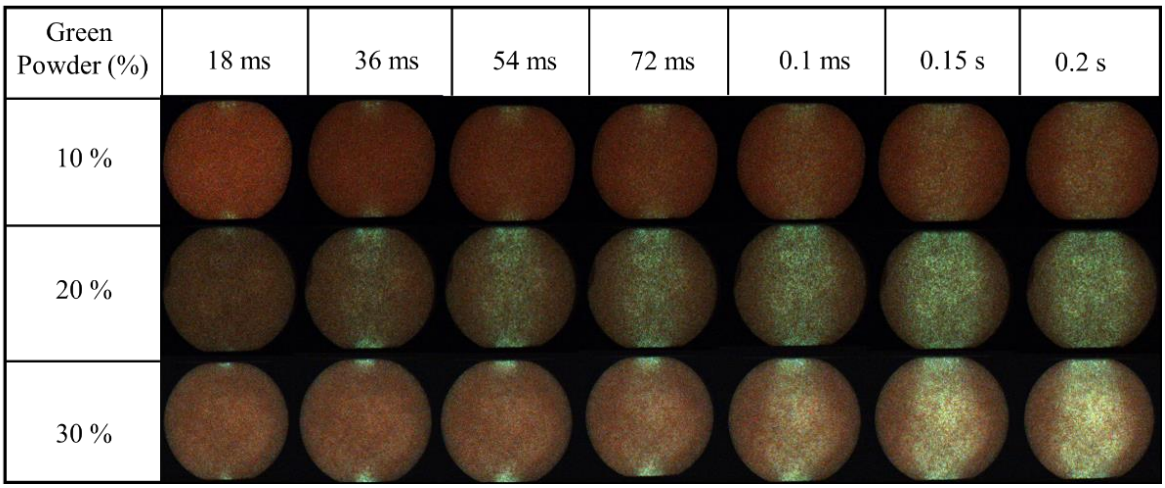

Figure 8.2.1: Images of stress transformation in color-modulated ML composite/epoxy pellets at different times.

REFERENCES

[1] M. Anpo and M. Che, "Applications of photoluminescence techniques to the characterization of solid surfaces in relation to adsorption, catalysis, and photocatalysis," *Advances in catalysis*, vol. 44, pp. 119-257, 1999.

[2] K. Murthy, "Thermoluminescence and its applications: a review," in *Defect and Diffusion Forum*, vol. 347: Trans Tech Publ, pp. 35-73, 2014.

[3] A. Feng and P. F. Smet, "A review of mechanoluminescence in inorganic solids: compounds, mechanisms, models and applications," *Materials*, vol. 11, no. 4, p. 484, 2018.

[4] S. S. Haider, J. Barzowska, P. Sybilski, and A. Suchocki, "Designing of experimental setup for impact induced mechanoluminescence measurements," *Measurement*, vol. 203, p. 112012, 2022.

[5] L. Kricka, "Clinical applications of chemiluminescence," *Analytica chimica acta*, vol. 500, no. 1-2, pp. 279-286, 2003.

[6] A. J. Syed and J. C. Anderson, "Applications of bioluminescence in biotechnology and beyond," *Chemical Society Reviews*, vol. 50, no. 9, pp. 5668-5705, 2021.

[7] H. K. Henisch, "Electroluminescence," *Reports on Progress in Physics*, vol. 27, no. 1, p. 369, 1964.

[8] B. Chandra and K. Shrivastava, "Dependence of mechanoluminescence in rochelle-salt crystals on the charge-produced during their fracture," *Journal of Physics and Chemistry of Solids*, vol. 39, no. 9, pp. 939-940, 1978.

[9] B. Chandra, "Mechanoluminescence," in *Luminescence of solids*: Springer, pp. 361-389, 1998.

[10] J.-C. Zhang, X. Wang, G. Marriott, and C.-N. Xu, "Trap-controlled mechanoluminescent materials," *Progress in Materials Science*, vol. 103, pp. 678-742, 2019.

[11] V. Dubey, N. Dubey, M. M. Domanska, M. Jayasimhadri, and S. J. Dhoble, *Rare-Earth-Activated Phosphors: Chemistry and Applications*. Elsevier, 2022.

[12] C. Xu, T. Watanabe, M. Akiyama, and X. Zheng, "Artificial skin to sense mechanical stress by visible light emission," *Applied Physics Letters*, vol. 74, no. 9, pp. 1236-1238, 1999.

[13] C.-N. Xu, T. Watanabe, M. Akiyama, and X.-G. Zheng, "Direct view of stress distribution in solid by mechanoluminescence," *Applied Physics Letters*, vol. 74, no. 17, pp. 2414-2416, 1999.

[14] L. Kobakhidze, C. J. Guidry, W. A. Hollerman, and R. S. Fontenot, "Detecting mechanoluminescence from ZnS: Mn powder using a high speed camera," *IEEE Sensors Journal*, vol. 13, no. 8, pp. 3053-3059, 2013.

[15] H. Zhang, H. Yamada, N. Terasaki, and C.-N. Xu, "Stress-induced mechanoluminescence in $SrCaMgS_{i2}O_7$: Eu," *Electrochemical and Solid-State Letters*, vol. 10, no. 10, p. J129, 2007.

[16] B. Liu, C. Shi, M. Yin, L. Dong, and Z. Xiao, "The trap states in the $Sr_2MgSi_2O_7$ and (Sr, Ca) $MgSi_2O_7$ long afterglow phosphor activated by Eu^{2+} and Dy^{3+}," *Journal of alloys and compounds*, vol. 387, no. 1-2, pp. 65-69, 2005.

[17] H. Zhang, H. Yamada, N. Terasaki, and C.-N. Xu, "Green mechanoluminescence of $Ca_2MgSi_2O_7$: Eu and $Ca_2MgSi_2O_7$: Eu, Dy," *Journal of The Electrochemical Society*, vol. 155, no. 2, p. J55, 2007.

[18] Y. Lin *et al.*, "Preparation and characterization of long afterglow $M_2MgSi_2O_7$-based (M: Ca, Sr, Ba) photoluminescent phosphors," *Materials chemistry and physics,* vol. 82, no. 3, pp. 860-863, 2003.

[19] H. Zhang, N. Terasaki, H. Yamada, and C.-N. Xu, "Mechanoluminescence of europium-doped $SrAMgSi_2O_7$ (A= Ca, Sr, Ba)," *Japanese Journal of Applied Physics,* vol. 48, no. 4S, p. 04109, 2009.

[20] K. Van den Eeckhout, P. F. Smet, and D. Poelman, "Persistent luminescence in Eu^{2+}-doped compounds: a review," *Materials,* vol. 3, no. 4, pp. 2536-2566, 2010.

[21] N. Kodama, T. Takahashi, M. Yamaga, Y. Tanii, J. Qiu, and K. Hirao, "Long-lasting phosphorescence in Ce^{3+}-doped $Ca_2Al_2SiO_7$ and $CaYAl_3O_7$ crystals," *Applied physics letters,* vol. 75, no. 12, pp. 1715-1717, 1999.

[22] M. Akiyama, C.-N. Xu, H. Matsui, K. Nonaka, and T. Watanabe, "Recovery phenomenon of mechanoluminescence from $Ca_2Al_2SiO_7$: Ce by irradiation with ultraviolet light," *Applied Physics Letters,* vol. 75, no. 17, pp. 2548-2550, 1999.

[23] L. Li, K.-L. Wong, P. Li, and M. Peng, "Mechanoluminescence properties of Mn^{2+}-doped BaZnOS phosphor," *Journal of Materials Chemistry C,* vol. 4, no. 35, pp. 8166-8170, 2016.

[24] B. Chandra, V. Chandra, S. Mahobia, P. Jha, R. Tiwari, and B. Haldar, "Real-time mechanoluminescence sensing of the amplitude and duration of impact stress," *Sensors and Actuators A: Physical,* vol. 173, no. 1, pp. 9-16, 2012.

[25] C. Li, C.-N. Xu, L. Zhang, H. Yamada, and Y. Imai, "Dynamic visualization of stress distribution on metal by mechanoluminescence images," *Journal of Visualization,* vol. 11, no. 4, pp. 329-335, 2008.

[26] J. Kim *et al.*, "Quasi-dynamic visualization of crack propagation and wake evolution in Y-TZP ceramic by mechano-luminescence," *Metals and Materials International,* vol. 14, no. 2, pp. 165-169, 2008.

[27] K. Hyodo, Y. Terasawa, C.-N. Xu, H. Sugaya, H. Mishima, And S. Miyakawa, "Mechanoluminescent stress imaging for hard tissue biomechanics," *Journal of Biomechanics,* no. 45, p. S263, 2012.

[28] T. Zhan, C.-N. Xu, O. Fukuda, H. Yamada, and C. Li, "Direct visualization of ultrasonic power distribution using mechanoluminescent film," *Ultrasonics sonochemistry,* vol. 18, no. 1, pp. 436-439, 2011.

[29] N. Terasaki, H. Yamada, and C.-N. Xu, "Ultrasonic wave induced mechanoluminescence and its application for photocatalysis as ubiquitous light source," *Catalysis Today,* vol. 201, pp. 203-208, 2013.

[30] M. Philibert and K. Yao, "Explore Ultrasonic-Induced Mechanoluminescent Solutions towards Realising Remote Structural Health Monitoring," *Sensors,* vol. 24, no. 14, p. 4595, 2024.

[31] V. Chandra, B. Chandra, and P. Jha, "Models for intrinsic and extrinsic elastico and plastico-mechanoluminescence of solids," *Journal of luminescence,* vol. 138, pp. 267-280, 2013.

[32] K. Melde, T. Qiu, and P. Fischer, "Fast spatial scanning of 3D ultrasound fields via thermography," *Applied Physics Letters,* vol. 113, no. 13, 2018.

[33] M. Kersemans, P. F. Smet, N. Lammens, J. Degrieck, and W. Van Paepegem, "Fast reconstruction of a bounded ultrasonic beam using acoustically induced piezo-luminescence," *Applied Physics Letters,* vol. 107, no. 23, 2015.

[34] V. Sonwane, A. Gaur, B. Haldar, S. Pandey, and B. Chandra, "Ultrasonic pulse induced mechanoluminescence of europium doped strontium aluminate micro-crystals," *Recent Research in Science and Technology,* vol. 4, no. 8, 2076-5061, 2012.

[35] S. E. Michels, M. Kersemans, M. Versluis, G. Lajoinie, and P. F. Smet, "Fast and High-Resolution Ultrasound Pressure Field Mapping Using Luminescent Membranes," *Advanced Optical Materials,* vol. 9, no. 12, p. 2100085, 2021.

[36] Y. Ding, B. So, J. Cao, F. Langenhorst, and L. Wondraczek, "Light Delivery, Acoustic Read-Out, and Optical Thermometry Using Ultrasound-Induced Mechanoluminescence and the Near-Infrared Persistent Luminescence of CaZnOS: Nd^{3+}," *Advanced Optical Materials,* vol. 11, no. 17, p. 2300331, 2023.

[37] T. Zhou *et al.*, "Unrevealing temporal mechanoluminescence behaviors at high frequency via piezoelectric actuation," *Small,* vol. 19, no. 8, p. 2207089, 2023.

[38] Y. Ding, B. So, J. Cao, and L. Wondraczek, "Ultrasound-Induced Mechanoluminescence and Optical Thermometry Toward Stimulus-Responsive Materials with Simultaneous Trigger Response and Read-Out Functions," *Advanced Science,* vol. 9, no. 23, p. 2201631, 2022.

[39] D. Vij, *Luminescence of solids*. Springer Science & Business Media, 2012.

[40] A. J. Walton, "Triboluminescence," *Advances in Physics,* vol. 26, no. 6, pp. 887-948, 1977.

[41] F. Bacon, *The Two Bookes of Sr. Francis Bacon, of the Proficience and Advancement of Learning, Divine and Humane*. IL [ie J. Lichfield], 1994.

[42] F. Bacon, "The Advancement of Learning [I ed. 1605]. New York: PF Collier and Son," ed, 1901.

[43] R. Waller, "Essays of natural experiments made in the Academy del Cimento under the protection of the most serene Prince Leopold of Tuscany. Englisht by the ingenious Richard Waller Esq; fellow of the Royal Society," *Philosophical Transactions of the Royal Society of London,* vol. 14, no. 164, pp. 757-758, 1667.

[44] E. N. Harvey, "A history of luminescence from the earliest times until 1900," 1957.

[45] J. I. Zink, G. E. Hardy, and J. E. Sutton, "Triboluminescence of sugars," *The Journal of Physical Chemistry,* vol. 80, no. 3, pp. 248-249, 1976.

[46] P. Jha and B. Chandra, "Survey of the literature on mechanoluminescence from 1605 to 2013," *Luminescence,* vol. 29, no. 8, pp. 977-993, 2014.

[47] B. Chandra, "Mechanoluminescence," *Luminescence of solids,* pp. 361-389, 1998.

[48] M. Nakamura, K. Saitoh, M. Ikeyama, T. Kozuka, And I. Shigematsu, "A study on the utilization of an electro-conductive surface layer on a Si_3N_4 ceramic formed by ion implantation as a crack gage and a strain gage," *Journal of the Ceramic Society of Japan,* vol. 101, no. 1169, pp. 139-142, 1993.

[49] H. Yanagida, "Intelligent ceramics," *Ferroelectrics,* vol. 102, no. 1, pp. 251-257, 1990.

[50] C.-N. Xu, H. Yamada, X. Wang, and X.-G. Zheng, "Strong elasticoluminescence from monoclinic-structure $SrAl_2O_4$," *Applied Physics Letters,* vol. 84, no. 16, pp. 3040-3042, 2004.

[51] X. Wang, C. N. Xu, H. Yamada, K. Nishikubo, and X. G. Zheng, "Electro-mechano-optical conversions in Pr^{3+}-doped $BaTiO_3$–$CaTiO_3$ ceramics," *Advanced Materials,* vol. 17, no. 10, pp. 1254-1258, 2005.

[52] H. Zhang, H. Yamada, N. Terasaki, and C.-N. Xu, "Blue light emission from stress-activated CaYAl3O7: Eu," *Journal of the Electrochemical Society,* vol. 155, no. 5, p. J128, 2008.

[53] C. N. Xu, "Coatings," *Encyclopedia of smart materials,* 2002.

[54] Y. Jia, M. Yei, and W. Jia, "Stress-induced mechanoluminescence in $SrAl_2O_4$:Eu^{2+}, Dy^{3+}" *Optical Materials,* vol. 28, no. 8-9, pp. 974-979, 2006.

[55] R. Shrivastava and J. Kaur, "Characterisation and mechanoluminescence studies of $Sr_2MgSi_2O_7$: Eu^{2+}, Dy^{3+}," *Journal of Radiation Research and Applied Sciences,* vol. 8, no. 2, pp. 201-207, 2015.

[56] L. Zhang, C.-N. Xu, H. Yamada, and N. Bu, "Enhancement of mechanoluminescence in $CaAl_2Si_2O_8$: Eu^{2+} by partial Sr^{2+} substitution for Ca^{2+}," *Journal of the Electrochemical Society,* vol. 157, no. 3, p. J50, 2010.

[57] X. Li, R. Hu, X. Wang, Y. Li, and X. Yao, "Intense mechanoluminescence and photostimulated luminescence with less afterglow in Pr^{3+}/Gd^{3+} co-doped $LiTaO_3$ phosphors," *Journal of Luminescence,* vol. 238, p. 118222, 2021.

[58] G. Qiu, H. Fang, X. Wang, and Y. Li, "Largely enhanced mechanoluminescence properties in Pr^{3+}/Gd^{3+} co-doped $LiNbO_3$ phosphors," *Ceramics International,* vol. 44, no. 13, pp. 15411-15417, 2018.

[59] M. Khokhar, R. Kher, D. Bisen, and B. Chandra, "Effect of divalent impurities on the mechanoluminescence of γ-irradiated NaCl and LiF single crystals," *Indian Journal of Pure and Applied Physics,* vol. 31, no. 12, pp. 952-954, 1993.

[60] A. Panigrahi, S. Dhoble, R. Kher, and S. Moharil, "Thermo and mechanoluminescence of Dy^{3+} activated $K_2Mg_2(SO_4)_3$ phosphor," *physica status solidi (a),* vol. 198, no. 2, pp. 322-328, 2003.

[61] B. Chandra, "Mechanoluminescence induced by elastic deformation of coloured alkali halide crystals using pressure steps," *Journal of Luminescence,* vol. 128, no. 7, pp. 1217-1224, 2008.

[62] D. Lapraz, H. Prevost, G. Angellier, F. Mady, M. Benabdesselam, and L. Dusseau, "Photoluminescence and thermally stimulated luminescence properties of $CaSO_4$: Sm^{3+} and $CaSO_4$:Ce^{3+},Sm^{3+}; $Sm^{3+}\rightarrow Sm^{2+}$ conversion and high temperature dosimetry," *physica status solidi (a),* vol. 204, no. 12, pp. 4281-4287, 2007.

[63] N. Brahme *et al.*, "Mechanoluminescence by impulsive deformation of γ-irradiated Er-doped CaF_2 crystals," *Journal of luminescence,* vol. 131, no. 5, pp. 965-969, 2011.

[64] R. Rai, A. Upadhyay, R. Kher, and S. Dhoble, "Mechanoluminescence, thermoluminescence and photoluminescence studies on Al_2O_3: Tb phosphors," *Journal of luminescence,* vol. 132, no. 1, pp. 210-214, 2012.

[65] X. Li, X. Wang, R. Hu, Y. Li, and X. Yao, "Modulating trap levels via co-doping Ca^{2+}/Si^{4+} in $LiTaO_3$: Pr^{3+} to improve both the intensity and threshold of mechanoluminescence," *Journal of Alloys and Compounds,* vol. 896, p. 162877, 2022.

[66] P. Xiong and M. Peng, "Near infrared mechanoluminescence from the Nd^{3+} doped perovskite $LiNbO_3$: Nd^{3+} for stress sensors," *Journal of Materials Chemistry C,* vol. 7, no. 21, pp. 6301-6307, 2019.

[67] V. Chandra, B. Chandra, and P. Jha, "Self-recovery of mechanoluminescence in ZnS:Cu and ZnS: Mn phosphors by trapping of drifting charge carriers," *Applied Physics Letters*, vol. 103, no. 16, p. 161113, 2013.

[68] N. Wang *et al.*, "Control of triboelectricity by mechanoluminescence in ZnS/Mn-containing polymer films," *Nano Energy*, vol. 90, p. 106646, 2021.

[69] J. S. Kim and G.-W. Kim, "New non-contacting torque sensor based on the mechanoluminescence of ZnS: Cu microparticles," *Sensors and Actuators A: Physical*, vol. 218, pp. 125-131, 2014.

[70] I. P. Sahu, D. Bisen, N. Brahme, and M. Ganjir, "Enhancement of the photoluminescence and long afterglow properties of $Sr_2MgSi_2O_7:Eu^{2+}$ phosphor by Dy^{3+} co-doping," *Luminescence*, vol. 30, no. 8, pp. 1318-1325, 2015.

[71] I. P. Sahu, D. Bisen, N. Brahme, L. Wanjari, and R. Tamrakar, "Luminescence properties of $Sr_2MgSi_2O_7$: Eu^{2+}, Ce^{3+} phosphor by solid state reaction method," *Physics Procedia*, vol. 76, pp. 80-85, 2015.

[72] H. Zhang, C.-N. Xu, N. Terasaki, and H. Yamada, "Detection of stress distribution using $Ca_2MgSi_2O_7$: Eu, Dy microparticles," *Physica E: Low-dimensional Systems and Nanostructures*, vol. 42, no. 10, pp. 2872-2875, 2010.

[73] S. K. Sao, N. Brahme, D. Bisen, G. Tiwari, and S. Dhoble, "Mechanoluminescence, thermoluminescence and photoluminescence studies of UV/γ-irradiated $Ba_2MgSi_2O_7$: Dy^{3+} phosphors," *Journal of Luminescence*, vol. 180, pp. 306-314, 2016.

[74] R. Shrivastava, J. Kaur, and B. Chandra, "Mechanoluminescence of $Ba_2MgSi_2O_7$ doped with Eu^{2+} and Dy^{3+} phosphor by impulsive deformation," *Luminescence*, vol. 30, no. 8, pp. 1207-1211, 2015.

[75] S. K. Sao, N. Brahme, D. Bisen, and G. Tiwari, "Thermoluminescence and Mechanoluminescence Properties of $Ba_{2-x}MgSi_2O_7:xCe^{3+}$ Phosphors," *Physics Procedia*, vol. 76, pp. 59-67, 2015.

[76] G. J. Yun, M. R. Rahimi, A. H. Gandomi, G.-C. Lim, and J.-S. Choi, "Stress sensing performance using mechanoluminescence of $SrAl_2O_4$:Eu (SAOE) and $SrAl_2O_4$:Eu,Dy (SAOED) under mechanical loadings," *Smart Materials and Structures*, vol. 22, no. 5, p. 055006, 2013.

[77] K. Satapathy, G. Mishra, R. Kher, and S. Dhoble, "Mechanoluminescence and thermoluminescence characterization of Tb^{3+} doped $CaAl_2O_4$: A theoretical and experimental study," *RSC advances*, vol. 5, no. 97, pp. 79391-79396, 2015.

[78] K. Satapathy and G. Mishra, "Hydrazine Assisted Self Combustion Synthesis of $CaAl_2O_4$: Eu Phosphor And Its Mechanoluminescence Characterization.", Vol. 16, No 1, pp 188-1 96, 2014.

[79] K. K. Satapathy, G. Mishra, and F. Khan, "$ZnAl_2O_4$:Eu novel phosphor: SEM and mechanoluminescence characterization synthesized by solution combustion technique," *Luminescence*, vol. 30, no. 5, pp. 564-567, 2015.

[80] H. Matsui, C.-N. Xu, and H. Tateyama, "Stress-stimulated luminescence from $ZnAl_2O_4$: Mn," *Applied Physics Letters*, vol. 78, no. 8, pp. 1068-1070, 2001.

[81] H. Matsui, C.-N. Xu, Y. Liu, and H. Tateyama, "Origin of mechanoluminescence from Mn-activated $ZnAl_2O_4$: Triboelectricity-induced electroluminescence," *Physical Review B*, vol. 69, no. 23, p. 235109, 2004.

[82] G. Tiwari, N. Brahme, R. Sharma, D. Bisen, S. K. Sao, and A. Khare, "Fracto-mechanoluminescence and thermoluminescence properties of orange-red emitting Eu^{3+} doped $Ca_2Al_2SiO_7$ phosphors," *Journal of Luminescence,* vol. 183, pp. 89-96, 2017.

[83] J. Barzowska *et al.*, "Mechanism of the luminescence enhancement of $SrSi_2N_2O_2$: Eu^{2+} phosphor via manganese addition," *The Journal of Physical Chemistry C,* vol. 126, no. 11, pp. 5292-5301, 2022.

[84] J. Botterman, K. Van den Eeckhout, I. De Baere, D. Poelman, and P. F. Smet, "Mechanoluminescence in $BaSi_2O_2N_2$:Eu," *Acta Materialia,* vol. 60, no. 15, pp. 5494-5500, 2012.

[85] K. Van den Eeckhout, D. Poelman, and P. F. Smet, "Persistent luminescence in non-Eu^{2+}-doped compounds: a review," *Materials,* vol. 6, no. 7, pp. 2789-2818, 2013.

[86] H. Matsui, C.-N. Xu, M. Akiyama, and T. Watanabe, "Strong mechanoluminescence from UV-irradiated spinels of $ZnGa_2O_4$:Mn and $MgGa_2O_4$: Mn," *Japanese Journal of Applied Physics,* vol. 39, no. 12R, p. 6582, 2000.

[87] N. Terasaki *et al.*, "Visualization of active crack on bridge in use by mechanoluminescent sensor," in *Health Monitoring of Structural and Biological Systems 2012*, 2012, vol. 8348: SPIE, pp. 652-657, 2012.

[88] K. Hyodo, Y. Terasawa, C.-N. Xu, H. Sugaya, H. Mishima, And S. Miyakawa, "Mechanoluminescent stress imaging for hard tissue biomechanics," *Journal of Biomechanics,* vol. 45, p. S263, 2012.

[89] Y. Fujio *et al.*, "Sheet sensor using $SrAl_2O_4$: Eu mechanoluminescent material for visualizing inner crack of high-pressure hydrogen vessel," *International Journal of Hydrogen Energy,* vol. 41, no. 2, pp. 1333-1340, 2016.

[90] C. Li, C.-N. Xu, Y. Adachi, and N. Ueno, "Real-time detection of axial force for reliable tightening control," in *Fourth International Conference on Experimental Mechanics*, vol. 7522: SPIE, pp. 989-994, 2010.

[91] N. Bergeron *et al.*, "Experimental evidence of triboluminescence induced by hypervelocity impact," *International journal of impact engineering,* vol. 33, no. 1-12, pp. 91-99, 2006.

[92] N. Bergeron, W. Hollerman, S. M. Goedeke, and R. Moore, "Triboluminescent properties of zinc sulfide phosphors due to hypervelocity impact," *International Journal of Impact Engineering,* vol. 35, no. 12, pp. 1587-1592, 2008.

[93] H. Zhang, N. Terasaki, H. Yamada, and C.-N. Xu, "Development of mechanoluminescent micro-particles $Ca_2MgSi_2O_7$: Eu, Dy and their application in sensors," *Thin Solid Films,* vol. 518, no. 2, pp. 610-613, 2009.

[94] R. Fontenot, W. Hollerman, M. Steuart, and B. Broussard, "Using triboluminescent impacts of ZnS: Mn as an impact detection sensor for spacecraft," in *Earth and Space 2010: Engineering, Science, Construction, and Operations in Challenging Environments*, pp. 2560-2567, 2010.

[95] C. Kai, L. Qianqian, and L. Zhen, "Advances in mechanoluminescence and its applications," *Chinese Journal of Organic Chemistry,* vol. 40, no. 11, pp. 3656-3671, 2020.

[96] W. A. Hollerman, R. S. Fontenot, K. N. Bhat, M. D. Aggarwal, C. J. Guidry, and K. M. Nguyen, "Review of Triboluminescence Impact Research at Projectile Speeds of 1 m/s to 6 km/s," *Procedia Engineering,* vol. 58, pp. 392-400, 2013.

[97] K. Gi-Woo, C. Min-Young, and K. Ji-Sik, "Frequency response analysis of mechanoluminescence in ZnS: Cu for non-contact torque sensors," *Sensors and Actuators A: Physical,* vol. 240, pp. 23-30, 2016.

[98] A. Yoshida, L. Liu, D. Tu, S. Kainuma, and C.-N. Xu, "Mechanoluminescent testing as an efficient inspection technique for the management of infrastructures," *Journal of Disaster Research,* vol. 12, no. 3, pp. 506-514, 2017.

[99] N. Terasaki and C.-N. Xu, "Historical-log recording system for crack opening and growth based on mechanoluminescent flexible sensor," *IEEE Sensors Journal,* vol. 13, no. 10, pp. 3999-4004, 2013.

[100] J. S. Kim, Y.-N. Kwon, N. Shin, and K.-S. Sohn, "Mechanoluminescent $SrAl_2O_4$: Eu, Dy phosphor for use in visualization of quasidynamic crack propagation," *Applied Physics Letters,* vol. 90, no. 24, p. 241916, 2007.

[101] G.-W. Kim and J.-S. Kim, "Dynamic torsional response analysis of mechanoluminescent paint and its application to non-contacting automotive torque transducers," *Measurement Science and Technology,* vol. 25, no. 1, p. 015009, 2013.

[102] J. S. Kim, Y.-N. Kwon, and K.-S. Sohn, "Dynamic visualization of crack propagation and bridging stress using the mechano-luminescence of $SrAl_2O_4$:(Eu,Dy,Nd)," *Acta Materialia,* vol. 51, no. 20, pp. 6437-6442, 2003.

[103] J. S. Kim, Y.-N. Kwon, N. Shin, and K.-S. Sohn, "Visualization of fractures in alumina ceramics by mechanoluminescence," *Acta Materialia,* vol. 53, no. 16, pp. 4337-4343, 2005.

[104] J. S. Kim, Y.-N. Kwon, N. Shin, and K.-S. Sohn, "Mechanoluminescent $SrAl_2O_4$: Eu, Dy phosphor for use in visualization of quasidynamic crack propagation," *Applied Physics Letters,* vol. 90, no. 24, 2007.

[105] C. Morano, N. Terasaki, T. Gao, G. Lubineau, and M. Alfano, "Snap-through Crack Propagation in Architected Bonded Interfaces Analyzed Using a Mechanoluminescent SAO/E Coating," *ACS Applied Materials & Interfaces,* Vol 15, pp. 40887- 40897, 2023.

[106] N. Terasaki and Y. Fujio, "Mechanoluminescent Visualization of Crack Propagation for Joint Evaluation," *JoVE (Journal of Visualized Experiments),* no. 191, p. e64118, 2023.

[107] R. W. Steinbrech, A. Reichl, and W. Schaarwächter, "R-curve behavior of long cracks in alumina," *Journal of the American Ceramic Society,* vol. 73, no. 7, pp. 2009-2015, 1990.

[108] R. E. Grimes, G. P. Kelkar, L. Guazzone, and K. W. White, "Elevated-Temperature R-Curve Behavior of a Polycrystalline Alumina," *Journal of the American Ceramic Society,* vol. 73, no. 5, pp. 1399-1404, 1990.

[109] X. Z. Hu, E. H. Lutz, and M. V. Swain, "Crack-tip-bridging stresses in ceramic materials," *Journal of the American Ceramic Society,* vol. 74, no. 8, pp. 1828-1832, 1991.

[110] C. Li, C. Xu, Y. Imai, and N. Bu, "Real-time visualisation of the Portevin–Le Chatelier effect with mechanoluminescent-sensing film," *Strain,* vol. 47, no. 6, pp. 483-488, 2011.

[111] C.-N. Xu, X.-G. Zheng, M. Akiyama, K. Nonaka, and T. Watanabe, "Dynamic visualization of stress distribution by mechanoluminescence image," *Applied Physics Letters,* vol. 76, no. 2, pp. 179-181, 2000.

[112] B. Chandra and J. Zink, "Triboluminescence and the dynamics of crystal fracture," *Physical Review B,* vol. 21, no. 2, p. 816, 1980.

[113] I. Grabec, "Triboluminiscence of rubber," *Journal of Polymer Science: Polymer Letters Edition,* vol. 12, no. 10, pp. 573-576, 1974.

[114] G. Alzetta, I. Chudáček, and R. Scarmozzino, "Excitation of triboluminescence by deformation of single crystals," *physica status solidi (a),* vol. 1, no. 4, pp. 775-785, 1970.

[115] K. Meyer and F. Polly, "Triboluminеszenzuntersuchungen an Alkalihalogeniden und Rohrzucker," *physica status solidi (b),* vol. 8, no. 2, pp. 441-456, 1965.

[116] K. Meyer and D. Obrikat, "Triboluminеszenzspektren von dotierten Zinksulfiden und ihr Zusammenhang zu Fotolumineszenzspektren1," *Zeitschrift für Physikalische Chemie,* vol. 240, no. 1, pp. 309-324, 1969.

[117] K. Nakayama, N. Suzuki, and H. Hashimoto, "Triboemission of charged particles and photons from solid surfaces during frictional damage," *Journal of Physics D: Applied Physics,* vol. 25, no. 2, p. 303, 1992.

[118] R. S. Fontenot, W. A. Hollerman, M. D. Aggarwal, K. N. Bhat, and S. M. Goedeke, "A versatile low-cost laboratory apparatus for testing triboluminescent materials," *Measurement,* vol. 45, no. 3, pp. 431-436, 2012.

[119] T. Zhan *et al.*, "Enhancement of impact-induced mechanoluminescence by swift heavy ion irradiation," *Applied Physics Letters,* vol. 100, no. 1, p. 014101, 2012.

[120] I. P. Sahu, "Enhancement of the mechanoluminescence properties on $Ca_2MgSi_2O_7$: Dy^{3+} phosphor by co-doping of charge compensator ions," *Applied Physics A,* vol. 122, pp. 1-10, 2016.

[121] S. Saha, S. Das, U. K. Ghorai, N. Mazumder, B. K. Gupta, and K. K. Chattopadhyay, "Charge compensation assisted enhanced photoluminescence derived from Li-codoped $MgAl_2O_4$:Eu^{3+} nanophosphors for solid state lighting applications," *Dalton transactions,* vol. 42, no. 36, pp. 12965-12974, 2013.

[122] X. Fu, S. Zheng, J. Shi, and H. Zhang, "Enhanced blue mechanoluminescence of $Sr_nMgSi_2O_{5+n}$: Eu alkali-earth silicate induced by defective phase," *Journal of Luminescence,* vol. 192, pp. 117-122, 2017.

[123] K. Sakai, T. Koga, Y. Imai, S. Maehara, and C.-N. Xu, "Observation of mechanically induced luminescence from microparticles," *Physical Chemistry Chemical Physics,* vol. 8, no. 24, pp. 2819-2822, 2006.

[124] H. Wang *et al.*, "Pressure-and rate-dependent mechanoluminescence with maximized efficiency and tunable wavelength in ZnS:Mn^{2+},Eu^{3+}," *ACS Applied Materials & Interfaces,* vol. 15, no. 23, pp. 28204-28214, 2023.

[125] I. Sokólska and S. Kück, "Optical characterization of Cr^{3+} doped $LiTaO_3$ crystals relevant for laser application," *Spectrochimica Acta Part A: Molecular and Biomolecular Spectroscopy,* vol. 54, no. 11, pp. 1695-1700, 1998.

[126] A. Wilkinson, A. Cheetham, and R. Jarman, "The defect structure of congruently melting lithium niobate," *Journal of applied physics,* vol. 74, no. 5, pp. 3080-3083, 1993.

[127] Q. Wang *et al.*, "$Pr_2BaNiMnO_{7-}$ δ double-layered Ruddlesden–Popper perovskite oxides as efficient cathode electrocatalysts for low temperature proton conducting solid oxide fuel cells," *Journal of materials chemistry A,* vol. 8, no. 16, pp. 7704-7712, 2020.

[128] J. Tauc, R. Grigorovici, and A. Vancu, "Optical properties and electronic structure of amorphous germanium," *physica status solidi (b),* vol. 15, no. 2, pp. 627-637, 1966.

[129] S. Tian, P. Feng, S. Ding, Y. Wang, and Y. Wang, "A color-tunable persistent luminescence material $LiTaO_3$:Pr^{3+} for dynamic anti-counterfeiting," *Journal of Alloys and Compounds,* vol. 899, p. 163325, 2022.

[130] H. Li *et al.*, "Commendable Pr^{3+}-activated $Ba_2Ga_2GeO_7$ phosphor with high-brightness white long-persistent luminescence," *Journal of Materials Chemistry C*, vol. 7, no. 22, pp. 6698-6705, 2019.

[131] D. Tu, C. N. Xu, A. Yoshida, M. Fujihala, J. Hirotsu, and X. G. Zheng, "$LiNbO_3$: Pr^{3+}: a multipiezo material with simultaneous piezoelectricity and sensitive piezoluminescence," *Advanced Materials*, vol. 29, no. 22, p. 1606914, 2017.

[132] W. Ryba-Romanowski, I. Sokólska, S. Gołab, and T. Łukasiewicz, "Photoluminescence of $LiTaO_3$: Pr," *Applied physics letters*, vol. 70, no. 6, pp. 686-687, 1997.

[133] Y. Liang, F. Liu, Y. Chen, X. Wang, K. Sun, and Z. Pan, "Red/near-infrared/short-wave infrared multi-band persistent luminescence in Pr^{3+}-doped persistent phosphors," *Dalton Transactions*, vol. 46, no. 34, pp. 11149-11153, 2017.

[134] B. Macalik, R. Lisiecki, R. M. Kowalski, and W. Ryba-Romanowski, "Down-and up-conversion of femtosecond light pulses into Pr^{3+} luminescence in $LiTaO_3$:Pr^{3+} single crystal," *Journal of Luminescence*, vol. 224, p. 117294, 2020.

[135] W. Gryk, D. Dyl, W. Ryba-Romanowski, and M. Grinberg, "Spectral properties of $LiTaO_3$:Pr^{3+} under high hydrostatic pressure," *Journal of Physics: Condensed Matter*, vol. 17, no. 35, p. 5381, 2005.

[136] Y. Guan, T. Tsuboi, Y. Huang, and W. Huang, "Concentration quenching of praseodymium ions Pr^{3+} in $BaGd_2(MoO_4)_4$ crystals," *Dalton Transactions*, vol. 43, no. 9, pp. 3698-3703, 2014.

[137] D. J. Rixen and P. L. van der Valk, "An impulse based substructuring approach for impact analysis and load case simulations," *Journal of Sound and Vibration*, vol. 332, no. 26, pp. 7174-7190, 2013.

[138] D. Van der Heggen *et al.*, "Persistent Luminescence in Strontium Aluminate: A Roadmap to a Brighter Future," *Advanced Functional Materials*, vol. 32, no. 52, p. 2208809, 2022.

[139] C. Shalgaonkar and A. Narlikar, "A review of the recent methods for determining trap depth from glow curves," *Journal of Materials Science*, vol. 7, pp. 1465-1471, 1972.

[140] D. Van der Heggen, D. Vandenberghe, N. K. Moayed, J. De Grave, P. F. Smet, and J. J. Joos, "The almost hidden role of deep traps when measuring afterglow and thermoluminescence of persistent phosphors," *Journal of Luminescence*, vol. 226, p. 117496, 2020.

[141] K. Van den Eeckhout, A. J. Bos, D. Poelman, and P. F. Smet, "Revealing trap depth distributions in persistent phosphors," *Physical Review B*, vol. 87, no. 4, p. 045126, 2013.

[142] S. Kamimura, H. Yamada, and C.-N. Xu, "Strong reddish-orange light emission from stress-activated $Sr_{n+1}Sn_nO_{3n+1}$: Sm^{3+} (n= 1, 2,∞) with perovskite-related structures," *Applied Physics Letters*, vol. 101, no. 9, p. 091113, 2012.

[143] A. J. Bos, "Thermoluminescence as a research tool to investigate luminescence mechanisms," *Materials*, vol. 10, no. 12, p. 1357, 2017.

[144] V. Laguta, L. Havlak, V. Babin, J. Barta, J. Pejchal, and M. Nikl, "Charge Transfer and Charge Trapping Processes in Ca-or Al-Co-doped Lu_2SiO_5 and $Lu_2Si_2O_7$ Scintillators Activated by Pr^{3+} or Ce^{3+} Ions," *Materials*, vol. 16, no. 12, p. 4488, 2023.

[145] S. S. Haider *et al.*, "Visible to near-infrared mechanoluminescence from Pr-Doped $LiTaO_3$ for stress-sensing applications," *The Journal of Physical Chemistry C*, vol. 128, no. 1, pp. 489-498, 2023.

[146] S. E. Michels, G. Lajoinie, S. Hedayatrasa, M. Versluis, M. Kersemans, and P. F. Smet, "A theoretical framework for acoustically produced luminescence: From thermometry to ultrasound pressure field mapping," *Journal of Luminescence*, vol. 248, p. 118940, 2022.

[147] O. Bulliard-Sauret *et al.*, "Heat transfer intensification by low or high frequency ultrasound: Thermal and hydrodynamic phenomenological analysis," *Experimental Thermal and Fluid Science*, vol. 104, pp. 258-271, 2019.

[148] M. Legay, N. Gondrexon, S. Le Person, P. Boldo, and A. Bontemps, "Enhancement of heat transfer by ultrasound: review and recent advances," *International Journal of Chemical Engineering*, vol. 2011, 2011.

[149] M. Rasheedy, "Method of Hoogenstraaten as a tool for obtaining the trap parameters of general-order thermoluminescence glow peaks," *Radiation Effects & Defects in Solids*, vol. 160, no. 9, pp. 383-390, 2005.

[150] N. Paul, "Device for indicating the temperature distribution of hot bodies," ed: Google Patents, 1937.

[151] P. Neubert, "Method and apparatus for recording temperatures of hot bodies," *US Patent*, vol. 2, p. 29, 1937.

[152] C. D. Brites, S. Balabhadra, and L. D. Carlos, "Lanthanide-based thermometers: at the cutting-edge of luminescence thermometry," *Advanced Optical Materials*, vol. 7, no. 5, p. 1801239, 2019.

[153] M. D. Dramićanin, "Trends in luminescence thermometry," *Journal of Applied Physics*, vol. 128, no. 4, 2020.

[154] V. Mykhaylyk *et al.*, "Evaluation of Li_2SnO_3: Cr^{3+},Mn^{4+} as a dual-emitter luminescence sensor for cryogenic temperatures," *Journal of Materials Chemistry C*, vol. 12, no. 4, pp. 1341-1353, 2024.

[155] S. Collins *et al.*, "Comparison of fluorescence-based temperature sensor schemes: theoretical analysis and experimental validation," *Journal of applied physics*, vol. 84, no. 9, pp. 4649-4654, 1998.

[156] C. D. Brites *et al.*, "Thermometry at the nanoscale," *Nanoscale*, vol. 4, no. 16, pp. 4799-4829, 2012.

[157] V. Mykhaylyk *et al.*, "Multimodal non-contact luminescence thermometry with Cr-doped oxides," *Sensors*, vol. 20, no. 18, p. 5259, 2020.

[158] C. Yang *et al.*, "Design of anti-thermal quenching Pr^{3+}-doped niobate phosphors based on a charge transfer and intervalence charge transfer band excitation-driven strategy," *Inorganic Chemistry Frontiers*, vol. 10, no. 16, pp. 4808-4818, 2023.

[159] Y. Lu, Y. Li, J. Li, D. Lin, H. Lu, and H. Zou, "A novel near-infrared thermometry based on thermal quenching and negative thermal quenching materials with high sensitivity and accuracy," *Journal of Luminescence*, vol. 263, p. 120067, 2023.

[160] H. Zhang *et al.*, "A ratiometric optical thermometer with multi-color emission and high sensitivity based on double perovskite $LaMg_{0.402}Nb_{0.598}O_3$:$Pr^{3+}$ thermochromic phosphors," *Chemical Engineering Journal*, vol. 380, p. 122491, 2020.

[161] P. Cortelletti *et al.*, "Tuning the sensitivity of lanthanide-activated NIR nanothermometers in the biological windows," *Nanoscale*, vol. 10, no. 5, pp. 2568-2576, 2018.

[162] F. Zhuohong, L. Lin, W. Zhezhe, and Z. Zhiqiang, "NIR optical temperature sensing with efficiently relative sensitivity based on β-$NaYF_4$:Er^{3+} nanoparticles," *Journal of Luminescence*, vol. 221, p. 117005, 2020.

[163] M. Runowski, N. Stopikowska, D. Szeremeta, S. Goderski, M. Skwierczyńska, and S. Lis, "Upconverting lanthanide fluoride core@ shell nanorods for luminescent thermometry in the first and second biological windows: β-$NaYF_4$: Yb^{3+}–Er^{3+}@ SiO_2 temperature sensor," *ACS applied materials & interfaces,* vol. 11, no. 14, pp. 13389-13396, 2019.

[164] N. Stopikowska, M. Runowski, P. Woźny, S. Goderski, and S. Lis, "Improving temperature resolution of luminescent nanothermometers working in the near-infrared range using non-thermally coupled levels of Yb^{3+} & Tm^{3+}," *Journal of Luminescence,* vol. 228, p. 117643, 2020.

[165] L. Xing, R. Ao, Y. Liu, and W. Yang, "Optical thermometry based on the non-thermally coupled levels of Tm (III) in $LiNbO_3$ crystals," *Spectrochimica Acta Part A: Molecular and Biomolecular Spectroscopy,* vol. 222, p. 117159, 2019.

[166] L. Li, F. Qin, Y. Zhou, Y. Zheng, H. Zhao, and Z. Zhang, "Temperature sensing based on the $^4F_{7/2}/^4S_{3/2}-{}^4I_{5/2}$ upconversion luminescence intensity ratio in $NaYF_4$: Er^{3+}/Yb^{3+} nanocrystals," *Journal of Luminescence,* vol. 206, pp. 335-341, 2019.

[167] J. Wang *et al.,* "A novel high-sensitive upconversion thermometry strategy: Utilizing synergistic effect of dual-wavelength lasers excitation to manipulate electron thermal distribution," *Sensors and Actuators B: Chemical,* vol. 278, pp. 165-171, 2019.

[168] R. Shi, L. Lin, P. Dorenbos, and H. Liang, "Development of a potential optical thermometric material through photoluminescence of Pr^{3+} in La_2MgTiO_6," *Journal of Materials Chemistry C,* vol. 5, no. 41, pp. 10737-10745, 2017.

[169] C. D. Brites, K. Fiaczyk, J. F. Ramalho, M. Sójka, L. D. Carlos, and E. Zych, "Widening the temperature range of luminescent thermometers through the intra-and interconfigurational transitions of Pr^{3+}," *Advanced Optical Materials,* vol. 6, no. 10, p. 1701318, 2018.

[170] X.-J. Wang *et al.*, "A novel and high brightness AlN:Mn^{2+} red phosphor for field emission displays," *Dalton Transactions,* vol. 43, no. 16, pp. 6120-6127, 2014.

[171] H. Bechtel *et al.*, "Fully phosphor-converted LEDs with Lumiramic phosphor technology," in *Tenth International Conference on Solid State Lighting*, 2010, vol. 7784: SPIE, pp. 160-170.

[172] K. Hara, A. Sato, K. Azumada, T. Atsumori, and M. Shiratori, "Preparation of AlN: Mn films by metalorganic chemical vapor deposition for thin film electroluminescent devices," *physica status solidi (c),* no. 7, pp. 2274-2277, 2003.

[173] V. Bachmann, T. Jüstel, A. Meijerink, C. Ronda, and P. J. Schmidt, "Luminescence properties of $SrSi_2O_2N_2$ doped with divalent rare earth ions," *Journal of Luminescence,* vol. 121, no. 2, pp. 441-449, 2006.

[174] X. Song, R. Fu, S. Agathopoulos, H. He, X. Zhao, and J. Zeng, "Luminescence and energy transfer of Mn^{2+} co-doped $SrSi_2O_2N_2$:Eu^{2+} green-emitting phosphors," *Materials Science and Engineering: B,* vol. 164, no. 1, pp. 12-15, 2009.

[175] G. Li *et al.*, "Photoluminescence tuning via cation substitution in oxonitridosilicate phosphors: DFT calculations, different site occupations, and luminescence mechanisms," *Chemistry of Materials,* vol. 26, no. 9, pp. 2991-3001, 2014.

[176] B. Berzina, L. Trinkler, V. Korsaks, and R. Ruska, "Luminescent AlN: Mn nanoparticles for optical imaging of biological materials," *Biophysical Bulletin,* no. 43, pp. 22-29, 2020.

[177] A. Le Donne, S. Kanti Jana, S. Banerjee, S. Basu, and S. Binetti, "Optimized luminescence properties of Mn doped ZnS nanoparticles for photovoltaic applications," *Journal of Applied Physics,* vol. 113, no. 1, 2013.

[178] E. Mohagheghpour *et al.*, "Controllable synthesis, characterization and optical properties of ZnS: Mn nanoparticles as a novel biosensor," *Materials Science and Engineering: C,* vol. 29, no. 6, pp. 1842-1848, 2009.

[179] A. W. Topol *et al.*, "Chemical vapor deposition of ZnS:Mn for thin-film electroluminescent display applications," *Journal of materials research,* vol. 19, no. 3, pp. 697-706, 2004.

[180] L. Ma, K. Jiang, X.-t. Liu, and W. Chen, "A violet emission in ZnS: Mn, Eu: Luminescence and applications for radiation detection," *Journal of Applied Physics,* vol. 115, no. 10, 2014.

[181] N. J. Cherepy *et al.*, "Red-emitting manganese-doped aluminum nitride phosphor," *Optical Materials,* vol. 54, pp. 14-21, 2016.

[182] A. K. Somakumar *et al.*, "Temperature and pressure dependent luminescence mechanism of a zinc blende structured ZnS: Mn nanophosphor under UV excitation," *Journal of Materials Chemistry C,* vol. 12, no. 19, pp. 7041-7052, 2024.

[183] P. Sharma, R. Daipuriya, A. Bhagatji, S. Tyagi, and S. S. Pal, "Impurity induced mechano-luminescence under different pressure impacts for Mn doped ZnS microcrystals," *Optical Materials,* vol. 122, p. 111798, 2021.

[184] T. Zheng *et al.*, "Mechanoluminescence and photoluminescence heterojunction for superior multimode sensing platform of friction, force, pressure, and temperature in fibers and 3D-printed polymers," *Advanced Materials,* vol. 35, no. 40, p. 2304140, 2023.

[185] R. Ma *et al.*, "Interface synergistic effects induced multi-mode luminescence," *Nano Research,* vol. 15, no. 5, pp. 4457-4465, 2022.

[186] R. Ma *et al.*, "Reproducible mechanical-to-optical energy conversion in Mn(II) doped sphalerite ZnS," *Journal of Luminescence,* vol. 232, p. 117838, 2021.

[187] X. Wang *et al.*, "Dynamic pressure mapping of personalized handwriting by a flexible sensor matrix based on the mechanoluminescence process," *Adv. Mater,* vol. 27, no. 14, pp. 2324-2331, 2015.

[188] A. Qasem, P. Xiong, Z. Ma, M. Peng, and Z. Yang, "Recent advances in mechanoluminescence of doped zinc sulfides," *Laser & Photonics Reviews,* vol. 15, no. 12, p. 2100276, 2021.

[189] H. Liu *et al.*, "Realizing red mechanoluminescence of ZnS: Mn^{2+} through ferromagnetic coupling," *Advanced Functional Materials,* p. 2314422, 2024.

[190] P. F. Smet, J. Botterman, K. Van den Eeckhout, K. Korthout, and D. Poelman, "Persistent luminescence in nitride and oxynitride phosphors: a review," *Optical Materials,* vol. 36, no. 11, pp. 1913-1919, 2014.